NASA Contractor Report 4125

A Study of Single and Binary Ion Plasma Expansion Into Laboratory-Generated Plasma Wakes

Kenneth Herbert Wright, Jr.

CONTRACT NAS8-31088 and GRANT NAG8-058
FEBRUARY 1988

NASA

NASA Contractor Report 4125

A Study of Single and Binary Ion Plasma Expansion Into Laboratory-Generated Plasma Wakes

Kenneth Herbert Wright, Jr.
The University of Alabama in Huntsville
Huntsville, Alabama

Prepared for
George C. Marshall Space Flight Center
under Contract NAS8-31088 and Grant NAG8-058

National Aeronautics
and Space Administration

Scientific and Technical
Information Division

1988

Acknowledgement

I wish to thank Dr. R. Hugh Comfort, Dr. Nobie H. Stone, and Prof. Uri Samir for the advice offered during the completion of this study. Support for this study is acknowledged through NASA contract NAS8-31088 and NASA grant NAG8-058. The experiments were performed at the Marshall Space Flight Center in the space plasma physics research facilities of the Space Science Laboratory. The use of these facilities, the technical support received, and the interaction with the members of the Magnetospheric Physics Branch are gratefully acknowledged. I also thank Mr. Vincent A. Provenza, Jr. and Mr. Ronald Eakes of the machine shop at the University of Alabama in Huntsville for fabrication of the binary ion plasma source hardware and Boeing Computer Support Services for computer software support.

TABLE OF CONTENTS

LIST OF TABLES

LIST OF FIGURES

LIST OF SYMBOLS

A	Aperature area of probe.
$\mathcal{A}$	Ratio of the ion drift energy to the magnitude of the body potential.
B_{MIRROR}	Magnetic field in the electrostatic mirror region of the binary ion plasma source.
B_{EXIT}	Magnetic field in the exit region of the binary ion plasma source.
$\overline{C}_{i_\perp}$	Mean ion thermal speed.
C_S	Ion acoustic speed.
e	Electric charge.
E	Electric field.
E_i	Ion energy.
E_d	Ion drift energy.
f	Ion distribution function.
g	Normalized ion distribution function.
I	Ion current.
I_0	Peak value of ion current profile.
I_F	Ion current at the expansion front.
I_{N_E}	Exit neutralizer current of the binary ion plasma source.
k	Boltzmann's constant.
L	Electric potential scale length variation.
m_e	Electron mass.

M_i	Ion mass.
M_1	Mass of the major ion component.
M_2	Mass of the minor ion component.
M_L	Lighter mass ion component.
M_H	Heavier mass ion component.
$\mathcal{M}$	Mach number (V_{flow}/C_S).
n_0	Ambient ion number density.
n_{tot}	Ambient total ion number density.
n_e	Electron density.
n_s	Slow ion number density.
n_f	Fast ion number density.
$\mathbf{p}$	Normalized $\mathbf{r_1}$.
$\mathbf{r}$	Three-dimensional vector.
$\mathbf{r_1}$	Projection of $\mathbf{r}$ onto a plane orthogonal to the z-axis.
R_0	Body radius.
R_D	Ratio of the body radius to the Debye length (Debye ratio).
R_S	Radius of plasma source.
S	Mach number ($S = \mathcal{M}/\sqrt{2}$).
t	Time; equivalent expansion time for experiment: $t = z/V_{flow}$.
T_e	Electron temperature.
T_i	Ion temperature.
$T_{i_\parallel}$	Ion temperature parallel to plasma stream direction.
$T_{i_\perp}$	Ion temperature perpendicular to plasma stream direction.
T	Ratio of electron temperature to ion temperature.

$\mathbf{u}$	Normalized $\mathbf{v_1}$.
$\mathbf{v}$	Three-dimensional velocity vector.
$\mathbf{v_1}$	Projection of $\mathbf{v}$ on to a plane orthogonal to the z-axis.
v_z	Ion velocity component in the direction of the plasma flow.
V_{flow}	Flow velocity of plasma stream.
$V_{e_{th}}$	Electron thermal velocity.
$V_{i_{th}}$	Ion thermal velocity.
V_i	Ion velocity.
V_F	Velocity of the expansion front.
V_{FP}	Velocity of ions in the foot region of the transverse ion current profile.
W_0	Width of plasma disturbance at the location of a finite-sized body.
$W(z)$	Width of plasma disturbance at a downstream distance z from the body.
x	Coordinate of the one-dimensional planar expansion; distance transverse to the vacuum chamber axis.
X_0	Transverse distance of plasma disturbance extrapolated to the plate location.
X_1	Rarefaction wave point.
X_F	Position of the expansion front.
X_{FP}	Position (the 'foot point') where the ion current goes to zero.
y	Coordinate direction along the plate edge.
z	Coordinate parallel to the vacuum chamber axis.
Z_i	Ion charge state.
Z_1	Charge state of the major ion.
Z_2	Charge state of the minor ion.

Greek symbols

α	Ambient percentage of the lighter ion mass constituent.
γ	Ratio of the charge to mass ratios of each ion species ($= Z_2 M_1 / Z_1 M_2$).
$\Gamma_{e,i}$	Specific heat capacity of electrons or ions.
δ	Half-width at half maximum of the DIFP deflection voltage curve.
θ_{meas}, θ	Angle measured by DIFP.
$\Delta\theta$	DIFP angular window.
κ	Total grid transmission factor.
λ_D	Debye length.
μ	Ratio of the ion masses, M_1/M_2.
ξ	Self-similar variable, $x/C_S t$.
ξ_M	Upper limit of the range of validity of the self-similar solution.
σ	Standard deviation of Gaussian distribution.
τ	Self-similar variable, $\xi/\sqrt{2}$.
ϕ	Electric potential.
ϕ_b	Body potential.
ϕ_d	Deflection voltage applied to DIFP.
ϕ_d^*	Voltage at the peak current of a deflection voltage sweep.
ϕ_p	Voltage applied to Langmuir probe.
ϕ_{MIRROR}	Voltage applied to the inner grids of the electrostatic mirror.
ϕ_{R_E}	Voltage applied to a conducting ring near the exit neutralizer of the binary ion plasma source.

ϕ_{R_2}	Voltage applied to a conducting ring near the exit of source # 2 of the binary ion plasma source.
ϕ_r	Retarding voltage applied to DIFP.
ϕ_{sp}	Plasma space potential.
ϕ_{plate}	Applied plate potential (0 volts).
ϕ_{acc}	Anode potential in ion source.
Φ_B	Normalized body potential.
ω_{pi}	Ion plasma frequency.
Ω	Angular measurement range of DIFP.

CHAPTER I. INTRODUCTION

A. General comments on flowing plasma-body interactions

The relative motion between a plasma and a body produces an interaction which, in its most general context, is a fundamental occurrence in the solar system. Plasma outflow from the sun, the solar wind, streams past the various planets and smaller objects such as asteroids and comets, while moons move through local planetary plasma environments and, in some cases, the solar wind. In addition, man-made satellites travel through the various space plasma environments. The understanding of the particle and field behavior of this fundamental interaction is thus basic to space plasma physics.

The mutual interaction between a body and a plasma produces a disturbed region in which a complex interplay occurs between particles and fields as they self-consistently adjust to the presence of the object. Relative motion between the plasma and body increases both the disturbance volume and the complexity of the interaction. The region downstream from the body, or the wake, occupies the largest part of the disturbance and is the most structurally complex.

Bodies moving through space plasmas encounter a wide variety of environments. The plasmas may be magnetized or unmagnetized, collisionless, and composed of single or multiple ionic constituents with Maxwellian or non-Maxwellian ion and electron distributions. The flow regimes range from subsonic to supersonic and sub-Alfvenic to super-Alfvenic. The bodies as well can possess different properties; i.e., surfaces which are non-conducting or conducting, a surrounding neutral

or ionized gas cloud, and possibly an intrinsic magnetic field. This large array of properties involved in the plasma flow-body interacton can give rise to a rich variety of phenomena in the wake. Such phenomena can include shocks, ion acceleration, current systems, large gradients in plasma densities, potential wells, counterstreaming ions and electrons, wave-particle interactions, plasma oscillations, instabilities, and turbulence.

The motion of artificial satellites through magnetospheric plasmas and of some planetary moons in their planetary plasmas fall into the category of non-magnetized bodies with sub-Alfvenic, supersonic motion. Io and Titan orbiting through the magnetospheric plasma of their respective planets, Jupiter and Saturn, are examples of this type of interaction occurring in nature. Another example of this flow regime is the motion of spacecraft through the Earth's ionosphere.

As the body travels through its environmental plasma, ions are swept up by the surface. Immediately behind the body in the near wake, an ion void region forms. A gradient in the plasma properties, then, exists near the body surface. The process by which plasma expands from the ambient across this density gradient into the near wake is of basic interest. This plasma expansion into a 'vacuum' or into a less dense region is the subject of this dissertation.

B. The non-magnetized body - plasma flow interaction

Bodies orbiting through the near-Earth plasma can serve as a 'model' for studying the particular case of a non-magnetized body in a supersonic, sub-Alfvenic flow. Measurements from small ionospheric spacecraft have provided some information about the wake region. These data have come almost entirely from probes mounted flush with the satellite surface and as a byproduct from missions whose goals were to perform geophysical measurements of the ionospheric plasma. Hence, the data

obtained are meager, fragmentary, and incomplete – limited in both spatial coverage and scope [*Samir*, 1981]. The usefulness of such data to assess the validity of various laboratory experiments and theoretical treatments is then limited to providing 'bench mark' results for checking more general insights obtained from laboratory and theoretical investigations. However, the recent space shuttle missions have provided previously unavailable observations of the extended disturbed plasma environment about a relatively large body [e.g., *Stone et al.*, 1983; *Siskind et al.*, 1984; *Stone and Wright*, 1985; *Stone et al.*, 1986; *Grebowsky et al.*, 1987]. For a comparison of some of the in situ observations from the space shuttle with those from small satellites, see *Samir et al.* [1986].

The correct interpretation, reliability, and quality of low-energy plasma measurements made by probes mounted on satellites depend on the understanding of the physical processes governing the body-plasma interaction. Knowledge of the interaction can also be applied to the design of probes and their location on the satellite surface and/or on booms. Hence, there is technical interest, as well as the scientific interest, in studying the plasma interaction with a non-magnetized body.

In the absence of the needed in situ information, a substantial number of laboratory simulation studies, employing single ion plasmas, have provided useful insight into the nature of the interaction. The application of laboratory studies to space plasma phenomena in general is usually made through the concept of process simulation where the principle of qualitative scaling is employed [Falthammer, 1974; Block, 1976; Podgorny, 1978]. In process simulation it is the local behavior of the plasma that is simulated rather than the entire system. In this way, selected physical processes can be effectively studied. The principle of qualitative scaling permits relaxation of the classical Vlasov scaling laws by requiring only that (1) the relevant dimensionless parameters which are of the order of unity should (to the extent possible) retain this value in the laboratory, and (2) the relevant dimensionless

parameters which are either much larger or much smaller than unity should retain this inequality in the laboratory, but not necessarily by the same order of magnitude.

Even though limitations such as wall effects and non-thermal particle distributions exist in the laboratory, an extensive picture of the wake for the unmagnetized body-plasma flow interaction has been obtained. A brief discussion of the wake morphology gained from these laboratory studies will follow, bringing in information from the more recent studies when applicable. For a more detailed discussion of the laboratory wake studies pertaining to this case, see *Stone* [1981*a*].

The electrostatic flow interaction depends on the following dimensionless parameters:

$$S = V_{flow}/\sqrt{2kT_e/M_i}\,; \qquad \Phi_B = e\phi_b/kT_e\,; \qquad R_D = R_o/\lambda_D\,; \qquad T = T_e/T_i\,,$$

where S = ionic Mach number, Φ_B = normalized body potential, R_D = linear dimension normalized to Debye length, T = ratio of electron temperature to ion temperture, V_{flow} = flow velocity, M_i = ion mass, ϕ_b = body potential, R_o = effective body radius, λ_D = Debye length, e = electron charge, and k = Boltzmann's constant. These similarity parameters represent the relative strengths of the different terms in the equations which describe this interaction; namely, the coupled, nonlinear Vlasov - Poisson equations. The morphology of the wake region is governed by the values which these similarity parameters possess. Most laboratory studies have been concerned with hypersonic flows in which $S > 4$, $R_D \approx 10^{-1} - 10^2$, $T \gg 1$, and Φ_B varies over a wide range.

Figure 1 shows a schematic of the ion disturbance produced by a test body immersed in a mesosonic plasma flow [*Stone*, 1981*a*]. Mesosonic flow is defined as the flow velocity being much larger than the ion thermal velocity and much smaller than the electron thermal velocity. This definition includes supersonic flow in general, that is $S > 1$. The plasma sheath on the upstream, or front, side of the body can be somewhat compressed compared to the stationary plasma case due to

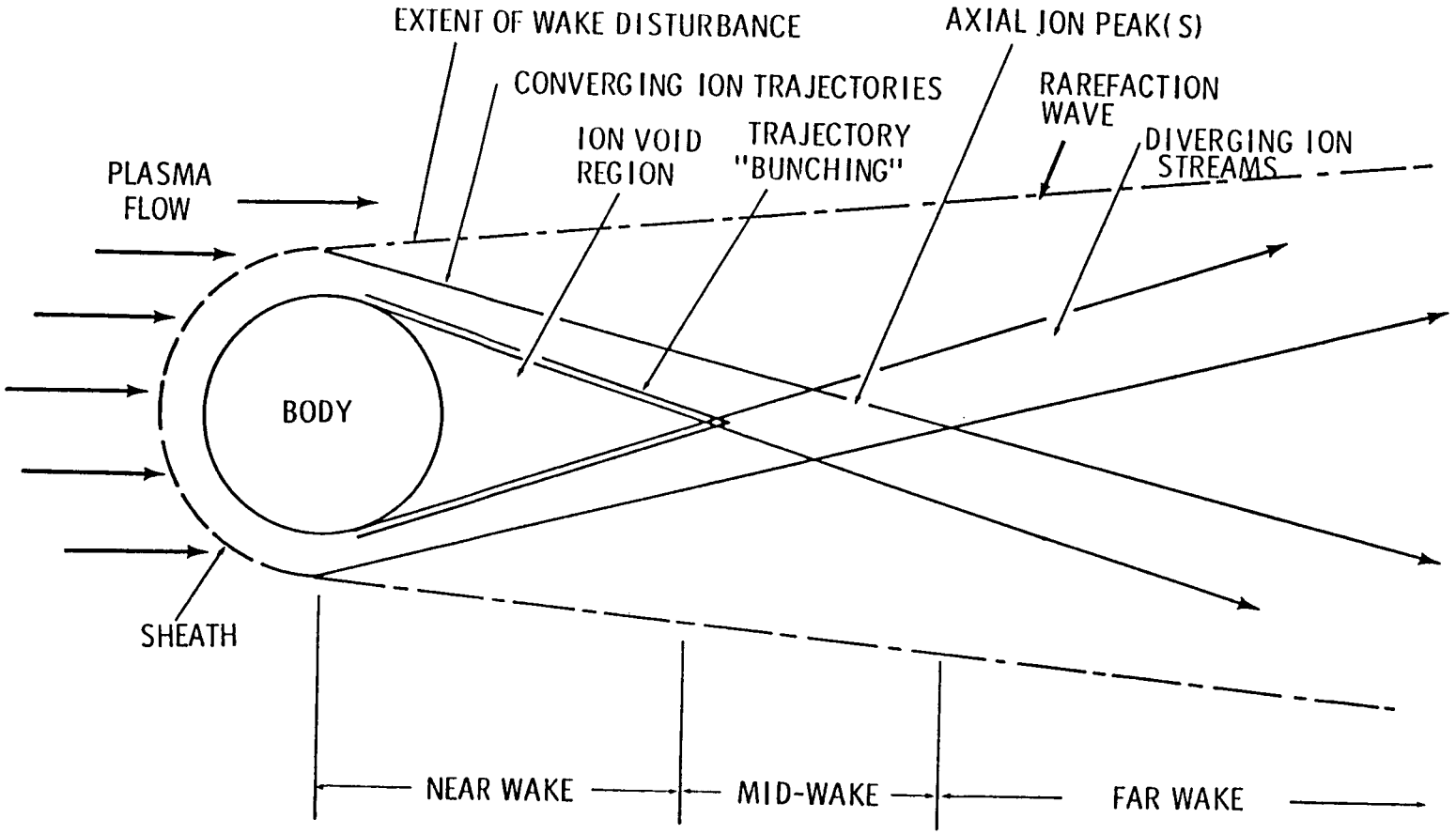

Figure 1. Ion behavior within the disturbed zone (after *Stone* [1981*a*]).

the directed ion motion. Downstream, a rarefaction wave initiates at the sheath boundary of the body and propagates away from the wake axis at the ion acoustic speed. The disturbance boundary defined by the rarefaction wave makes an angle, $\theta_S = \tan^{-1}(1/S)$, with respect to the wake axis. Based on the morphology of the ion behavior, the region inside the disturbance boundary can be roughly divided into three areas: the near, mid- , and far wake. In each of these regions, the expansion of particles from the ambient plasma into the wake is marked by a region of generally decreasing density (or current) variation.

Since the flow is mesosonic, the ions are swept out by the body, creating a near wake that is dominated by an ion void region. The highly mobile electrons are free to enter the ion void; however, a negative potential barrier is formed which acts to inhibit further electron entry [*Shuvalov*, 1979*a*,*b*; 1980]. Hence, the near wake is a region of extremely low particle density, for electrons as well as ions and neutrals. A density gradient then exists between the ambient plasma and the region immediately behind the body. The strength of this gradient depends on the various parameter values. The ion void region boundary (see Figure 1) is defined by the particular manner in which particles move into the wake.

Several mechanisms can act to bring ions into the near wake region; i.e., (1) deflection by sheath electric fields existing at the maximum cross-sectional area location, (2) acceleration by polarization electric fields developed from space charge effects acting over extended distances from the body, (3) diffusion from thermal motion, and (4) scattering by plasma oscillations and/or instabilities. The particular values of the dimensionless parameters given above will determine which is the dominant filling mechanism. Consider, for example, a hypersonic flow where (3) and (4) are relatively unimportant and that a negative Φ_B of a low to moderate value in magnitude exists. If $R_D \lesssim 1$, then (1) should dominate. The potential of the body extends a relatively far distance away from its surface resulting in a

substantial number of particles being deflected into the wake by the sheath. Deflection of particles by the sheath is analogous to Coulomb scattering, where momentum is transferred, but little energy is exchanged [*Stenzel et al.*, 1982]. The ion void boundary should be defined by a straight line in this case. Along this boundary, ions are observed to bunch together after being deflected by the sheath, determined both by scalar ion current measurements [*Stone*, 1981*b*; *Merlino and D'Angelo*, 1987] and by vector ion flux measurements [*Stone*, 1981*b*]. If $R_D \gg 1$, then (2) should dominate. The sheath size is small compared to the body size and, hence, the deflection of ions by the sheath will be minor. The density gradient between the plasma and the region immediately behind the body will be larger in this situation than for the former case. In responding to this density gradient, the different electron and ion mobilities result in charge separation between the ions and the electrons and, hence, the development of an electric field. This space charge effect acts over an extended region downstream from the body to define a curved boundary of the ion void. This dissertation is concerned with the influence of this polarization electric field mechanism for near wake filling. If intermediate values of R_D exist, then effects from both (1) and (2) should be observed. The ion void boundary may appear to have both linear and non-linear parts to its shape. A sufficiently large decrease in the negative value of Φ_B, however, will cause sheath deflection of particles to dominate, regardless of the value for R_D.

Other effects observed in the near wake include an axial electron temperature enhancement and oscillations along the wake boundary. *Oran et al.* [1975] found that an electron temperature enhancement, $[T_e(\text{wake})/T_e(\text{front})] \simeq 2$, exists in the ion void region and extends to a Mach number of body radii downstream, although with decreasing enhancement values. The plasma conditions were $R_D \simeq 4.4$, $S \simeq 7.1$, $\Phi_B = -2.9$, and $T_e(\text{front}) \simeq 1200\,\text{K}$. *Morgan et al.* [1987] show that $[T_e(\text{wake})/T_e(\text{front})] > 1$ for $\mathcal{A} > 1$ and $[T_e(\text{wake})/T_e(\text{front})] < 1$ for $\mathcal{A} < 1$, where

$\mathcal{A}$ is defined as the ratio the ion drift energy to the magnitude of the body potential. A velocity filtering mechanism is suggested to act in the near wake. The plasma conditions for the experiment were $R_D \simeq 10$, $S \simeq (1 - 3.5)$, $\Phi_B \simeq -(3 - 8)$, and $T_e(\text{front}) \simeq 4.4 \times 10^4$ K with an energetic tail of temperature 1.1×10^5 K. Also, *Shuvalov* [1979*a*, 1980] offers very limited measurements, in both quantity and spatial positions, of an elevated wake temperature, $[T_e(\text{wake})/T_e(\text{front})] \simeq 1.5$, for the plasma conditions $R_D \simeq 130$, $S \simeq 4.4$, $\Phi_B \simeq -1$, and $T_e(\text{front}) \simeq 4.6 \times 10^4$ K. *Singh et al.* [1987] suggest that counterstreaming electron expansions which produce electron distribution functions with larger second moments, i.e. higher 'temperatures' , may be responsible for the enhancement. In contrast to the the above results, *Intriligator and Steele* [1985] report no statistically significant near wake electron temperature enhancement. The plasma conditions of this experiment were $R_D \simeq 8.0$, $S \simeq 16$, $\Phi_B = 0$, and $T_e(\text{front}) \simeq 4.5 \times 10^4$ K. The ambient T_e value of this experiment is ≈ 40 times higher than the ambient T_e value of *Oran et al.* [1975], but close to the ambient T_e value in *Morgan et al.* [1987]. It is not yet clear why no T_e enhancement in the wake was observed in the *Intriligator and Steele* [1985] experiment. Oscillations along the wake boundary were reported by *Intriligator and Steele* [1982] and *Merlino and D' Angelo* [1987]. In *Merlino and D' Angelo* [1987], the spatial locations of the maximum noise amplitudes were shown to trace an 'X' pattern in the wake and the frequency value of the noise was more than an order of magnitude below the ion plasma frequency. It was also pointed out that the same general noise and spectral shape were present on the front side of the body.

The mid-wake region begins where ions start to cross the wake axis and is dominated by an axial ion current enhancement. This enhancement represents a peak in the variation of the ion current with downstream distance along the wake axis. Parametric investigations of the ion current peak have revealed the following characteristics [*Stone*, 1981*c*]: (1) the axial location of the peak is a linear function

of $[S \cdot R_D^{0.024}/|\Phi_B|]$; (2) the peak current value, normalized to the ambient current density, is a linear function of $[S/|\Phi_B|]^{1/2}$; and (3) the peak width, normalized by body radius, is a linear function $|\Phi_B|^{-1/2}$. This behavior was determined over the parameter range $0.7 \leq R_D \leq 5.4$, $9.4 \leq S \leq 15.8$, and $-103 \leq \Phi_B \leq -10$. Test body geometry plays a role in the magnitude of the current enhancement if the sheath geometry changes with thickness. Circular shaped body cross-sections result in the largest enhancements, since all ion streams through the sheath are focussed to a point. For a body with a square cross-section and a relatively thin sheath, the enhancement is reduced; ions are focussed along a line. However, as the sheath thickness enlarges, presenting a more circular cross-sectional shape to the plasma flow, the current enhancement for a body with a square cross-section will approach that for a sphere.

In *Shuvalov* [1979*a*,*b*], plasma flow about a sphere was examined for $R_D \simeq 100 - 130$, $S \simeq 4.4$, $\Phi_B \simeq -0.8$, and $T \simeq 7 - 10$ (with $T_e(\text{ambient}) \simeq 4.6 \times 10^4$ K). The ion current profiles transverse to the wake axis reveal a local peak on the axis in the mid-wake and existing over a range of downstream distance (z) from the body given by $1.2 \leq z/R_0 < 2.5$. However, the variation of the ion current along the wake axis shows only a monotonic change. For this relatively large R_D case, the sheath deflection of ions onto the wake axis is minimal. The action of the polarization space charge electric field on bringing ions into the wake is clearly demonstrated in this experiment, but this effect has only been minimally investigated in the bulk of the previous laboratory wake studies. As stated earlier, for large R_D bodies, the polarization electric field should be the prevalent mechanism for accelerating ions into the wake.

The far wake region is characterized by ion streams diverging away from the wake axis. The divergence of some of these streams, which cross the wake axis and follow ballistic trajectories, depends on the body potential. The far wake of

the small bodies ($R_D \ll 1$) are completely characterized by streams of this type. In other cases, the mid-wake axial ion peak occurring in the wake of bodies for $1 \simeq R_D < 20$ is observed to split into two peaks and propagate away from the wake axis at about the Mach angle [*Stone et al.*, 1972]. The motion of these peaks is independent of body potential, which suggests a collective interaction taking place in the mid-wake region. These features resemble soliton-like structures, but have not been identified as such. *Fournier and Pigache* [1975] also observe a variety of propagating wave and shock-like features occurring in the far wake. The mid-wake current enhancement observed by *Shuvalov* [1979*a*,*b*], noted above, does not split but gradually disappears, resulting in a smooth variation of current in the far wake. This suggests that for the larger R_D bodies at small Φ_B the far wake may be featureless. However, increasing the T_e/T_i ratio may change this picture.

The great majority of laboratory simulation experiments have used plasma streams where the ions had very little thermal motion in the transverse direction. *Fournier and Pigache* [1975] have carried out experiments using larger effective T_i; i.e., $T_e/T_i \leq 2$. The main result is that the wake becomes considerably less complicated. This is not surprising since ion thermal motions will smear out charge distributions and, hence, reduce local electric fields. The ion current is observed to have a smooth variation downstream from the test body as the ion void fills. For values of $\Phi_N \simeq -3$ and $1.6 \leq R_D \leq 45$, there is no mid-wake ion peak. However, as Φ_N becomes more negative, the peak can reappear. The precise value of T_e/T_i in combination with the other parameters where the detailed wake structure disappears remains an open question.

In summary, laboratory investigations using cold, collisionless, single ion plasmas have revealed much about the wake structure of a non-magnetized body in a mesosonic flow regime. The parametric dependence of the features in the three wake sub-divisions have been noted for a fairly wide range of the parameters $S > 4$,

$R_D \approx 10^{-1} - 10^2$, $T \simeq 1$ to $T \gg 1$, and a wide range for Φ_B. The deflection of ions by sheath electric fields due to body surface potentials has been well documented, while the acceleration of ions by space charge polarization electric fields existing over extended regions from the body has not.

C. Investigative goal and approach

The near wake of a non-magnetized body in mesosonic plasma flow is dominated by an ion void which can be filled by a variety of mechanisms, as discussed above. The prevalent mechanisms depend on the values of the similarity parameters. The near wake is known to be non-neutral. It is electron-rich in the inner region about the wake axis and ion-rich in the outer region of the disturbance. The response of the plasma to the large density gradient in the wake boundary near the body is of key interest.

Gurevich et al. [1966] suggested that filling of the wake should be analogous to plasma expansion into a 'vacuum' or into a less dense region. (In fact, this idea appears to have been suggested in a rudimentary form by *Kornowski* [1960], but not fully developed.) The nature of the polarization electric field, mentioned in the preceeding section, can be explained in terms of the processes and phenomena involved in plasma expansion. When a plasma expands across a strong density gradient, the high mobility of the electrons leads to the development of an electric field that dynamically couples to the ions and forms an ion expansion front. This field will continue to exist as long as the transit time for thermal electrons from the ambient plasma reservoir to the expansion front is relatively short and energy can be resupplied. Plasma expansion is such a fundamental process that it should occur anywhere there is a sufficiently large density (or pressure) gradient. As discussed above, such a gradient is always created in the near wake of a mesosonic body

with a thin plasma sheath. Therefore, 'plasma expansion' may be responsible for populating the wake of bodies with $R_D \gg 1$ and small Φ_N, which, as discussed above, is a case of general interest to space plasma physics.

This study addresses the applicability of the plasma expansion process to account for the filling of the wake void region through a series of conceptually simple simulation experiments. Mesosonic plasma flow around the edge of a thin, 'semi-infinite' plane is examined. Investigating the plasma flow about one edge has the effect of making the body size appear very large. The potential between the body and the plasma is kept small in order to minimize sheath deflection effects on the filling process and to maximize the density gradient at the plate edge. Experiments are conducted in both single ion and binary ion plasmas. Various diagnostic probes, including a probe capable of vector measurements of the ion motion, are employed. The focus of this investigation is on the effect of d.c. electric fields on the motion of the ion population. The role of oscillations in scattering particles into the wake is not an experimental goal, and hence, no spectrum analysis of the ion or electron current is performed.

In the reference frame of a body in motion through the ionosphere, all plasma constituents flow past the body with a common velocity. To properly simulate this interaction in the laboratory when two ionic constituents are present, a source is needed to accelerate the disimilar masses to a common velocity. Prior to the present study, no experiment has properly satisfied this condition. To perform the binary ion plasma experiment described in this study, a plasma source has been constructed that can produce the required common flow velocity for the ions. In addition, the density ratio of the ionic constituents is controllable. Thus two new dimensions are added to the parameter space availiable for laboratory studies; namely, the ionic mass ratio and the ionic density ratio.

The phenomena and processes of plasma expansion in single and binary ion plasmas with a single electron temperature are discussed in Chapter II. The basic equations treated in plasma expansion theories are presented in Appendix A, while a brief discussion of the expansion of plasmas with multiple electron temperatures, which may be of interest in certain solar system situations, can be found in Appendix B. The results of the single ion plasma experiment are presented and discussed in Chapter III and the binary ion plasma experiment, in Chapter IV. A description of the diagnostic instruments used and their manner of operation are given in Appendix C and the development of the plasma expansion analogy, as applied to near wakes, with the accompanying limitations, is described in Appendix D. A summary and the conclusions arrived at in this study are given in Chapter V.

CHAPTER II. EXPANSION OF PLASMA INTO A VACUUM: BASIC PHENOMENA AND PROCESSES

Plasma expansion phenomena are well known to laboratory researchers and have been observed since the early days of plasma physics research. Fast ions were observed in vacuum arc experiments in the 1930's [e.g., *Tanberg*, 1930; *Kobel*, 1930; *Tonks*, 1938], although a satisfactory explanation of those experimental findings, acceleration of particles by electric fields, was not given until years later [e.g., *Plyutto*, 1961]. Since then various experimental configurations have produced plasma expansion phenomena: e.g., vacuum sparks [e.g., *Hendel and Reboul*, 1962; *Goldenbaum and Gerber*, 1973]; laser-target interactions [e.g., *Linlor*, 1963; *Decoste and Ripin*, 1977; *Tan and Borovsky*, 1986]; Q-machines [e.g., *Korn et al.*, 1970]; pulsed plasma sources [e.g., *Eselevich and Fainshtein*, 1980; *Chan et al.*, 1984; *Hairapetian and Stenzel*, 1987]; and body-flowing plasma interactions [e.g., *Alikhanov et al.*, 1971; *Wright et al.*, 1985, 1986; *Raychaudhuri et al.*, 1986]. Ambient densities and electron temperatures in these experiments range from $n \simeq 10^{18}\,\mathrm{cm}^{-3}$ and $T_e \simeq 10\,\mathrm{keV}$ for laser created plasmas to $n \simeq 10^{5}\,\mathrm{cm}^{-3}$ and $T_e \simeq 0.3\,\mathrm{eV}$ for rarefied plasmas. The plasma expansion process is thus seen to be fundamental to a wide range of plasmas.

An extensive effort has been devoted to the study of electric fields and energy and density distributions of particles created by plasma expansion into a vacuum or into a less dense plasma. The development of the existing collisionless plasma expansion models was driven mainly by results from laser-pellet interaction experiments. The studies were mostly theoretical, which included both analytical and numerical methods for a wide range of conditions. The types of plasmas considered

include: (1) plasmas composed of a single electron temperature and a single ion species [e.g., *Gurevich et al.*, 1966, 1968 (the pioneering work in this area); *Allen and Andrews*, 1970; *Widner et al.*, 1971; *Crow et al.*, 1975; *Bezzerides et al.*, 1978; *Mora and Pellet*, 1979; *Lonngren and Hershkowitz*, 1979; *Denavit*, 1979; *Gurevich and Meshcherkin*, 1981*a*, *b*; *Sack and Schamel*, 1985]; (2) plasmas composed of electrons with multiple temperatures and a single ion species [e.g., *Bezzerides et al.*, 1978; *Denavit*, 1979; *Wickins and Allen*, 1979; *True et al.*, 1981; *Mitrovich*, 1985]; (3) plasmas composed of a single electron temperature and multiple ion species [e.g., *Gurevich et al.*, 1973*a*, 1979; *Gurevich and Pitaevsky*, 1975; *Decoste and Ripin*, 1978; *Felber and Decoste*, 1978; *Anderson et al.*, 1978; *Gurevich and Meshcherkin*, 1981*a*; *Begay and Forslund*, 1982; *Singh and Schunk*, 1982, 1983*a*, *b*]; (4) plasmas composed of electrons with multiple temperatures and multiple ion species [e.g., *Wickens and Allen*, 1981]. The papers cited can be divided according to whether a fluid and/or a kinetic approach is used, whether ion pressure effects are treated, and whether overall charge neutrality or charge separation is considered. Among the papers which treat charge separation effects are: *Widner et al.* [1971]; *Crow et al.* [1975]; *Lonngren and Hershkowitz* [1979]; *Denavit* [1979]; *True et al.* [1981]; *Gurevich and Meshcherkin* [1981*b*]; *Singh and Schunk* [1982, 1983*a*, *b*]; and *Sack and Schamel* [1985]. Among the papers which assume equal ion and electron densities throughout the expansion region are: *Gurevich et al.* [1966, 1968, 1973*a*, 1979]; *Allen and Andrews* [1970]; *Gurevich and Pitaevsky* [1975]; *Anderson et al.* [1978]; *Bezzerides et al.* [1978]; *Decoste and Ripin* [1978]; *Felber and Decoste* [1978]; *Mora and Pellat* [1979]; *Wickens and Allen* [1979, 1981]; *Gurevich and Meshcherkin* [1981*a*]; and *Begay and Forslund* [1982].

In spite of its association with dense plasmas in fusion research, it was only recognized recently that the phenomena and processes involved in plasma expansion may be active in solar system and cosmic plasma phenomena and, therefore,

necessary for the interpretation of planetary and space observations. *Graur et al.* [1973] used plasma expansion to estimate the plasma and field behavior of a barium cloud release in the ionophere. *Podgorny et al.* [1980], in their experimental study of the interaction of a magnetized plasma flow with glass and wax spheres (simulating the Moon and Venus, respectively), allude to plasma expansion effects in explaining the magnetic field behavior in the wake region of these bodies. *Singh and Schunk* [1982, 1983*b*, 1985] examined the flow of plasma from the earth's ionosphere in the context of plasma expansion. The review of *Samir et al.* [1983] examined wake data from ionospheric spacecraft in the context of plasma expansion and called attention to the potential application, in general, of the plasma expansion theory to the structure of the wake region behind obstacles moving through space plasmas (first suggested by *Gurevich et al.* [1966]). *Borovsky et al.* [1984] applied properties of the laser blow-off plasma expanding into a surrounding ionized gas to the case of the interaction between between supernova ejecta and the interstellar medium. *Tariq et al.* [1985] employed plasma expansion as a possible explanation for the energetic ion observations in the wake of the Jovian moon Ganymede. *Eselevich and Filippov* [1986] examined the mechanism of solar wind formation by appealing to generalized results derived from laboratory experiments on plasma expansion.

Most of the above papers have not explicitly included magnetic forces acting on the particles during the expansion. If a magnetic field is mentioned, it is argued to be sufficiently strong such that the plasma expasnion is essentially confined to one dimension along the field. Examples of experiments in which magnetic forces play a significant role are: *Chang and Hashmi* [1977]; *Raadu* [1979]; *Chan* [1986]; and *Hairapetian and Stenzel* [1987]. Examples of theoretical treatments which include a magnetic force term are: *Mathews* [1971]; *Gurevich et al.* [1973*b*]; *Anderson et al.* [1980]; and *Johnson and Lonngren* [1982]. While it is recognized that magnetic fields play an important role in space plasma physics, the understanding of the more

basic case of plasma expansion in the absence of magnetic fields is a necessity first. Therefore, the subsequent discussion of plasma expansion in this chapter and of experimental work in this dissertation presented in later chapters will be confined to the non-magnetized case.

The plasma types to be treated in this dissertation will be: (1) the single ion and single electron temperature plasma and (2) the binary ion and single eletron temperature plasma. The discussion of the expansion of these plasma types in this chapter is restricted to basic phenomena and processes and some of the results. Comments on the other types of plasmas, which may have relevance to certain solar system situations, can be found in Appendix B.

A. Single ion and single electron temperature plasma

Consider a one-dimensional, planar expansion process from the initial condition of a semi-infinite plasma held by a diaphragm at its boundary located at $x = 0$ and a vacuum region for $x > 0$ (see Figure 2a). At a time $t = 0$ the diaphragm is removed and the plasma expands into the vacuum. As stated above, the evolution of the expansion has been studied in both fluid and kinetic treatments. Solutions to the cold ion fluid equations (see Appendix A.2) will be used first to illustrate the expansion process. However, information will be freely drawn from all studies in order to discuss the details of the expansion process.

Some characteristic features of the expansion process can be found by solving for the ion dynamics under the assumptions of charge neutrality, isothermal electrons, and neglect of electron inertia. Charge neutrality removes the Debye length as a relevant characteristic length from the equations (see Poisson's equation in Appendix A). Thus any functional dependence on x or t will be through the combination (x/t). In other words, the distribution of all quantities at various instants in

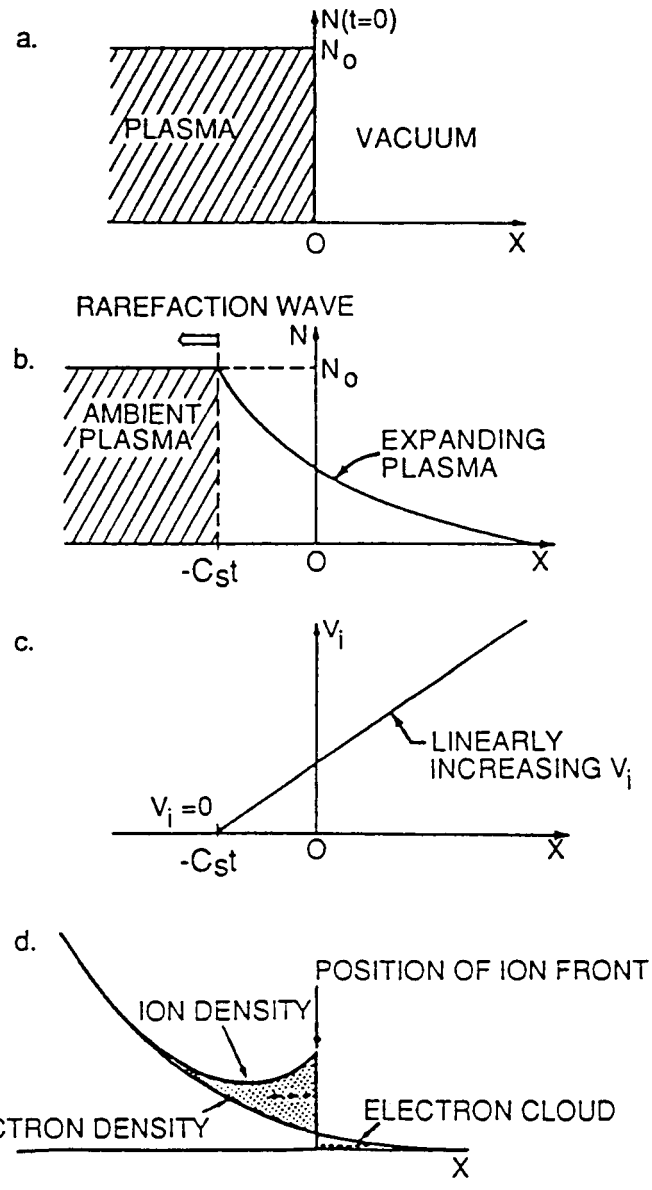

Figure 2. Plasma expansion: (a) initial conditions; (b) evolution of density; (c) evolution of velocity; (d) schematic of electron and ion densities at the expansion front.

time will be similar, differing only in the scale along the x-axis, which increases proportionally with time. Solutions of this type, commonly referred to as self-similar (*Landau and Lifshitz*, 1963), describe the asymptotic state of the expansion. Neglecting electron inertia means that the electron pressure gradient is in equilibrium with the electric field. For an ambient electron distribution which is Maxwellian, the electrons, assuming a constant temperature, will obey the Boltzmann relation; i.e., $n_e = Z_i n_0 \exp(e\phi/kT_e)$, where n_e = electron density, Z_i = ion charge state, and n_0 = ambient ion density. An analytical solution of the fluid equations in Appendix A.2 is obtained by assuming a space-time dependence for density and velocity through the variable

$$\xi = \frac{x}{C_S t}, \tag{2.1}$$

where $C_S = (Z_i kT_e/M_i)^{1/2}$ is the ion acoustic speed. The self-similar solutions for a plasma consisting of a single ionic species are (e.g., *Allen and Andrews*, [1970]; *Lonngren*, [1977]):

$$n_e = Z_i n_i = Z_i n_o \exp[-(\xi + 1)] \tag{2.2}$$

$$V_i = C_S(\xi + 1) \tag{2.3}$$

$$\phi = -\frac{kT_e}{e}(\xi + 1) \tag{2.4}$$

for $\xi + 1 > 0$. The polarization electric field is then given by

$$E = -d\phi/dx = (kT_e/e)(1/C_S t)H(\xi + 1), \tag{2.5}$$

where $H(\xi + 1)$ is the step function.

Figures 2*b* and 2*c* show the self-similar density and velocity solutions. A region of decreased plasma density, the 'rarefaction wave' , propagates into the plasma at the ion acoustic speed. Note that for large values of x this theory predicts high velocity ions with a density that approaches zero. The quasi-neutrality assumption is valid as long as the scale length, L, of the potential variation is much greater

than the Debye length; i.e., $L \gg \lambda_D$. This scale length can be estimated by setting $L \simeq C_S t$. An upper limit for the validity of the quasi-neutrality assumption and, hence, the range for which the self-similar solution is valid, can be found by equating L to the local Debye length. Since $\lambda_D \propto (T_e/n_e)^{1/2}$, letting $L = \lambda_D$, with n_e given by (2.2), implies that $C_S t = (kT_e/4\pi e^2 Z_i n_0)^{1/2} \exp[-(\xi_M + 1)/2]$, where ξ_M is the upper limit. Solving this equation yields $\xi_M = [2\ln(\omega_{pi} t) - 1]$, where $t > \omega_{pi}^{-1}$ and $\omega_{pi} = (4\pi n_0 Z_i^2 e^2/M_i)^{1/2}$ = the ambient ion plasma frequency [*Singh and Schunk*, 1982]. For values of $\xi > \xi_M$, the potential due to the self-similar solution given by (2.4) is not valid and the self-similar solution is restricted to $-1 < \xi < \xi_M$. The time required for the ions to respond to the polarization electric field and produce a quasi-neutral plasma flow with $n_e = Z_i n_i$ is seen to be ω_{pi}^{-1}. The velocity at $\xi = \xi_M$ can be interpreted as the velocity of an ion front (V_F) moving in the expansion region with

$$V_F = C_S(\xi_M + 1) = 2C_S \ln(\omega_{pi} t). \tag{2.6}$$

The energy of the ions at the front is then given by

$$E_i = \frac{1}{2} M_i V_F^2 = 2Z_i kT_e [ln\omega_{pi} t]^2. \tag{2.7}$$

and/or energy per charge by

$$E_i/Z_i = 2kT_e [ln\omega_{pi} t]^2. \tag{2.8}$$

All ions with the same charge to mass ratio will be accelerated in the same manner.

The behavior of the ions that were initially near the plasma-vacuum interface (see Figure 2*a*) was examined by, among others, *Crow et al.* [1975] and *Sack and Schamel* [1985]. Numerical solutions were found to the cold ion fluid equations which drop the assumption of quasi-neutrality and use Possion's equation to determine the electric potential. At the instant the diaphragm is removed, the electrons will rush ahead of the ions due to their higher mobility. This charge separation

produces an electric field which accelerates the ions to form a leading 'front' of the expansion. Equation (2.5), the electric field for the quasi-neutral case, shows that at time $t = 0$, the electric field is infinite. This is not physical so an initial finite electric field value, assumed in the numerical simulations, is estimated by smearing out the electron density distribution around the $x = 0$ point. Figure $2d$ shows a typical picture of the charge densities at the expansion front at a time during the expansion. In general, the ion density at the front decreases with time. However, in a numerical simulation without dissipation [*Sack and Schamel*, 1985], the non-monotonic behavior of the electric field and ion velocity at the front was shown to induce the phenomenon of wave-breaking, the nonlinear steepening of the density over a certain time period and the subsequent singularity. Adding some numerical dissipation stabilizes this rapid density growth. Whether this dissipation represents the actual physical case or not will be dictated by ambient plasma properties. Some sort of local ion enhancement at the expansion front is seen in various numerical simulations, but to different degrees. This indicates differences in the inherent dissipation involved in the various calculation schemes used. The ion expansion front in *Crow et al.* [1975] was found to accelerate to supersonic velocities described by the logarithmic behavior of (2.6) for expansion times up to $\omega_{pi}t = 100$. In the simulation by *Sack et al.* [1986] for times up to $\omega_{pi}t = 350$, three distinct time regions of acceleration were seen: (1) an initial acceleration regime to logarithmic time dependence for the velocity; (2) a region where the velocity changes very slowly; and (3) a final acceleration region where the velocity increases faster than the first region.

Examination of the electron behavior during the expansion was performed in several studies. Electron dynamics were included by *Denavit* [1979] in order to examine the assumptions of an isothermal electron expansion and the neglect of electron inertia. The result was that these assumptions are correct to order $(Z_i m_e/M_i)^{1/2}$ [*Denavit*, 1979]. Basically, electron inertia in this process can be

neglected as long as the ion streaming velocity is less than the electron thermal velocity. The electron thermal energy is the source of the ion translational energy. Therefore, if the electron gas does not cool, then heat must flow from the ambient plasma to the expansion region. *Mora and Pellat* [1979] showed that at the rarefaction wave, $q_e(\xi = -1) = dE_i/dt$, where q_e = heat flux and E_i = ion energy. *Gurevich and Meshcherkin* [1981*a*] showed how the fast ion acceleration depends on the ambient electron distribution function. The ion front velocity increases with increasing number of particles in the tail of the electron distribution. The above studies considered essentially an infinite ambient plasma reservoir. If a finite plasma source is considered, i.e., a finite total energy in the plasma, the electron temperature decreases much faster and the ion expansion front attains a certain maximum velocity which depends on the initial dimension of the plasma source [*Chutov and Kravchenko*, 1980].

In the pioneering work of *Gurevich et al.* [1966, 1968], numerical self-similar solutions were found using a kinetic approach; i.e., the Vlasov equation for ions (see Appendix A.1). The assumptions of quasi-neutrality and a Boltzmann relation for electrons were also employed. A self-similar solution was calculated using the variable $\tau = (x/t)(M_i/2Z_ikT_e)^{1/2} = \xi/\sqrt{2}$. Comparing the results from the kinetic approach and the results from the cold ion fluid treatment shows that including ion temperature smooths out the weak discontinuity at $\xi = -1$ (see Figure 2*b*) and introduces differences in the ion density values in the rarefaction region for $\xi > -1$. As the ion temperature (T_i) increases, the difference between the two approaches increases. In the expansion region at large ξ (or large x), changing the T_e/T_i ratio was shown to introduce small differences between the two approaches. The reason for these small differences is that at large ξ the ambient ion distribution function evolves to a streaming delta-function-like distribution. Figure 3 shows the normalized distribution function in velocity space for various values of the self-similar

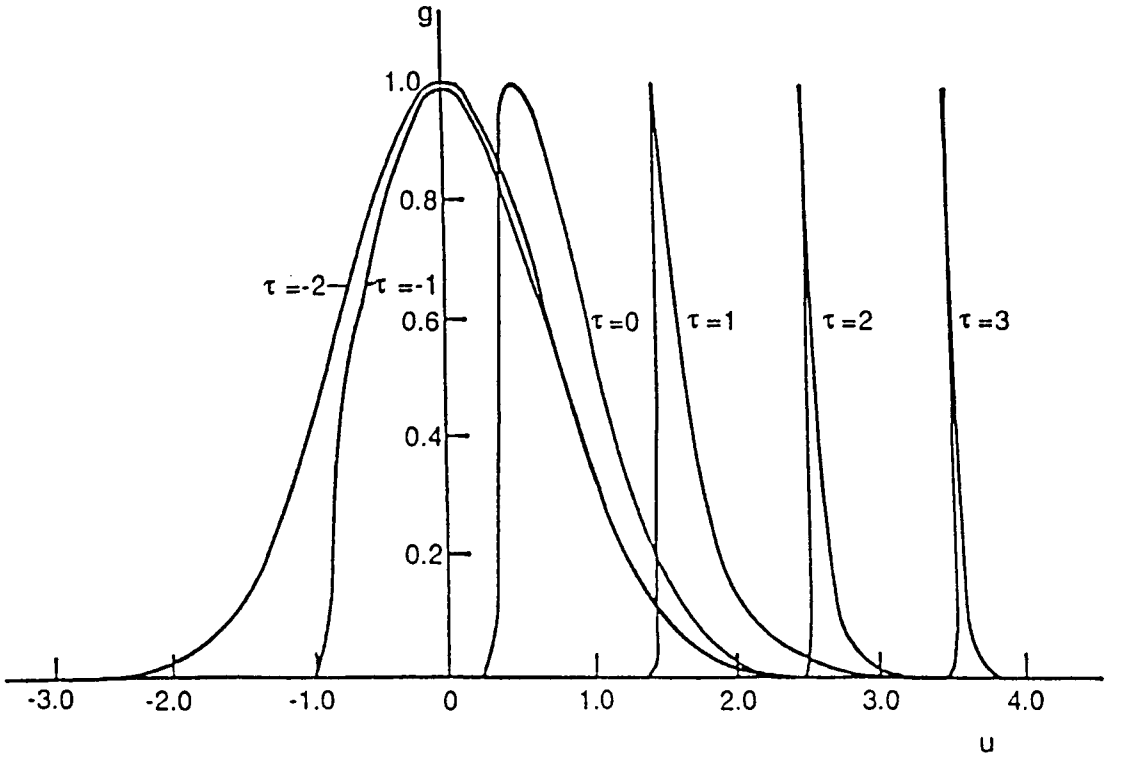

Figure 3. The evolution of normalized distribution function g with the normalized velocity u for different values of τ. $g \equiv (2\pi kT_i/M_i)^{1/2}\, n_0^{-1}\, f$, $u \equiv V_i\sqrt{2Z_ikT_e/M_i}$, and $\tau \equiv x/(t\sqrt{2Z_ikT_e/M_i}) = \xi/\sqrt{2}$. The figure is after *Gurevich et al.* [1966].

variable τ. Note the ion acceleration and the decreasing width of the distribution. The effective ion temperature was found to vary as $\exp(-2\xi)$. Therefore, the ion dynamics in the expansion region for large τ (or ξ) can be reasonably well described by using the cold ion fluid equations. This is an important physical conclusion since it specifies a condition (i.e., distance in space) where the fluid solutions based on the cold ion momentum equation can be applied.

A comparison between studies using the quasi-neutral assumption and those using numerical computer simulations which drop this assumption and use the potential determined from the Poisson equation was performed by *Crow et al.* [1975], *Denavit* [1979], *Singh and Schunk* [1982], and *Sack and Schamel* [1985]. The ion expansion front is a feature that is always produced. In the region between the expansion front and the rarefaction wave some of the general predictions of the quasi-neutral, self-similar theories are applicable. A simple way to describe the range of applicability (say, in x or t) of the self-similar solution vis-a-vis the solutions obtained by considering the Poisson equation is to say that the self-similar solutions are valid for times $t > \omega_{pi}^{-1}$. This is the time it takes the ions to respond to the fast expansion of the electrons and create a quasi-neutral plasma flow.

Smaller density gradients existing at $t = 0$ (as compared to the large gradient shown in Figure 2*a*) affect the expansion process by increasing the time required for the expansion to become a quasi-neutral flow [*Felber and Decoste*, 1978; *Singh and Schunk*, 1982].

The case of an expansion of a dense plasma into a more tenuous plasma was also treated by *Gurevich et al.* [1968], *Gurevich and Pitaevsky* [1975], and *Singh and Schunk* [1983b]. The boundary condition imposed by the second plasma population existing at $t = 0$ for $x > 0$ (see Figure 2a) adds to the variety of phenomena that occur in the expansion process. Limited acceleration of ions is a feature of this physical situation. Depending on the properties of the second plasma population,

there can be trapping of ions in potential wells, excitation of a two stream electrostatic instability, and jump discontinuities or shock waves occurring when the two plasmas have highly dissimilar ion temperatures [*Gurevich and Meshcherkin*, 1981*b*].

Figure 4 presents some experimental data obtained from pulsed plasma sources for investigating the one-dimensional expansion. Figure 4*a*, from *Eselevich and Fainshtein* [1981], shows a semi-log plot of the ion density at the front of an argon plasma versus $\sqrt{E_i}$, where E_i is the ion energy. The dashed line is the prediction obtained from combining (2.2) and (2.3); i.e., $n_i \propto \exp(-\sqrt{E_i})$. Figure 4*b*, also from *Eselevich and Fainshtein* [1981], shows the normalized ion front velocity (V_F/C_S) of the expanding argon plasma versus normalized time ($\omega_{pi}t$). Curve 1 gives the numerical simulation result of *Crow et al.* [1975], while curve 2 indicates the data behavior. The long time logarithmic behavior of the front velocity, in agreement with (2.6), is easily seen. The difference between curve 1 and the data is noted by *Eselevich and Fainshtein* [1981] to be due to: (1) the front width near the plasma source being greater than initial values in the numerical simulation; and (2) the uncertainty in the determination of the time and position at which the plasma is formed in the source. Plasma potential measurements during a plasma expansion were made by *Chan et al.* [1984] and are shown in Figure 4*c* as function of $\xi = x/C_S t$. The bulk motion of the plasma reaches a self-similar state [see (2.4)] in a few ion plasma periods. For the experiment, $\omega_{pi}^{-1} \simeq 10\,\mu$sec. The ion velocity at the expansion front reached $\approx 4C_S$ before the finite system length began to affect the ion motion.

The effective temperature of the ions at the front was observed to decrease, although at a much slower rate than the *Gurevich et al.* [1966] prediction, by *Eselevich and Fainshtein* [1981] and *Hairapetian and Stenzel* [1987]. The difficulty of simulating a truly one dimensional expansion probably affects this result strongly.

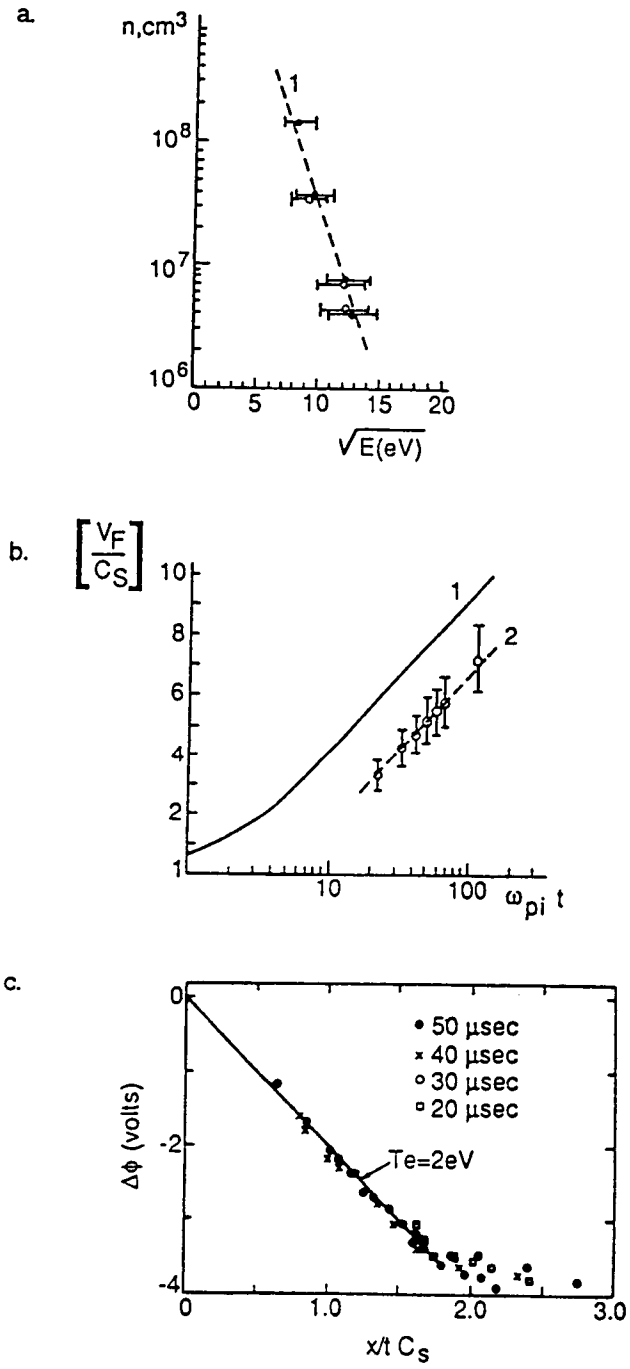

Figure 4. Measurements at the front of an argon plasma: (a) ion density versus $\sqrt{E}$, where E = ion energy. Data - (o, •), curve 1 - self-similar theory. (b) Normalized velocity (V_F/C_S) versus normalized time ($\omega_{pi}t$), curve 1 - result from *Crow et al.* [1975], curve 2 - data. (a) and (b) are after *Eselevich and Fainshtein* [1981]. (c) Plasma space potential versus self-similar varible $\xi = x/(C_S t)$ in an expanding argon plasma, line indicates self-similar theory (after *Chan et al.* [1984]).

That is, there is a coupling, probably through local random oscillations, between the dimensions transverse to the flow and parallel to the flow.

B. Binary ion and single electron temperature plasma

Planetary ionospheres and magnetospheres generally consist of more than one ion species. Studying the expansion of a binary ion, one electron temperature plasma is then of great practical value for understanding phenomena that occur in those environments; e.g., polar winds, wakes of bodies moving through these plasmas. The dynamics for the binary ion plasma depend on the similarity parameter

$$\gamma = Z_2 M_1 / Z_1 M_2. \tag{2.9}$$

Analytic solutions for this case are in general not possible and exist only under certain restrictive assumptions. Therefore, theoretical investigations have used numerical simulations extensively to gain insight into the behavior the binary ion plasma expansion [e.g., *Begay and Forslund*, 1982; *Singh and Schunk*, 1982].

To illustrate the behavior of the expansion in this case, however, consider that the following assumptions must be made so that an approximate analytic solution can be derived: (1) $Z_1 n_{10} \gg Z_2 n_{20}$, where Z_1, Z_2 = the charge state of each ion and n_{10}, n_{20} = the ambient ion density for each ion; (2) quasi-neutrality; and (3) $\xi \gg 1$ so that the fluid equations will apply. The subscript 1 will always refer to the major ionic constituent. The self-similar variable ξ is now defined in terms of the major ion as $\xi = x/C_{S1}t$, where $C_{S1} = (Z_1 k T_e / M_1)^{1/2}$.

The solutions for the density and velocity of M_1 are given by (2.2) and (2.3) respectively. From *Gurevich et al.* [1973*a*], the density solution for M_2 is given by

$$n_2 = \frac{2n_{20}}{\gamma} \exp\left[-\left(\frac{\xi}{\gamma} + 1\right)\right] \tag{2.10}$$

and the velocity solution for M_2 is given by

$$V_2 = C_{S1}(\xi + \gamma). \tag{2.11}$$

From (2.10) for $\gamma < 1$, it is seen that the minor ion density (n_2) decays much faster than the major ion density (n_1) given by (2.2). This density behavior for each ion species is illustrated in Figure 5*a* where $Z_1 = Z_2 = 1$, M_L = the lighter ion mass, and M_H = the heavier mass ion. Numerical simulations have demonstrated that in the $\gamma < 1$ case each ion species behaves roughly independently of the other and follows a self-similar description at large ξ [*Gurevich et al.*, 1973*a*; *Anderson et al.*, 1978; *Singh and Schunk*, 1982]. For $\gamma > 1$, the minor ion density (n_2) decays much slower than the major ion density (n_1) and at some value of ξ, n_2 becomes the dominant ion species, as illustrated in Figure 5*b*. The plasma motion in this case is thus seen to be significantly altered by the presence of the second ion. Note that in the *Gurevich et al.* [1973*a*] theory, the rarefaction wave for each ion species is predicted to propagate at different speeds, for each value of γ.

Figure 6 shows some results from a kinetic numerical simulation for the $\gamma > 1$ case [*Gurevich et al.*, 1973*a*]. The major ion is oxygen (O^+) and the minor ion is hydrogen (H^+), so $\gamma = 16$, with the ambient condition $Z_2 n_{20}/Z_1 n_{10} = 0.1$. The relative acceleration of hydrogen as compared with oxygen is readily seen. As the expansion begins, the relatively immobile oxygen initially provides a greater electric field to accelerate the hydrogen ions. As a result, the hydrogen ions gain an initial higher velocity than in the $\gamma < 1$ case. Note again the decreasing width of the distribution functions. At a time later in the expansion, the hydrogen density becomes comparable to the oxygen density at some value of ξ. A 'plateau region' in ion density, ion velocity, and potential is obtained, which implies constant values for density, velocity, and potential near the location where $n_1(O^+) = n_2(H^+)$. Although there are quantitative differences in the description of this plateau region by the analytical, quasi-neutral fluid solutions of *Gurevich et al.* [1973*a*] and

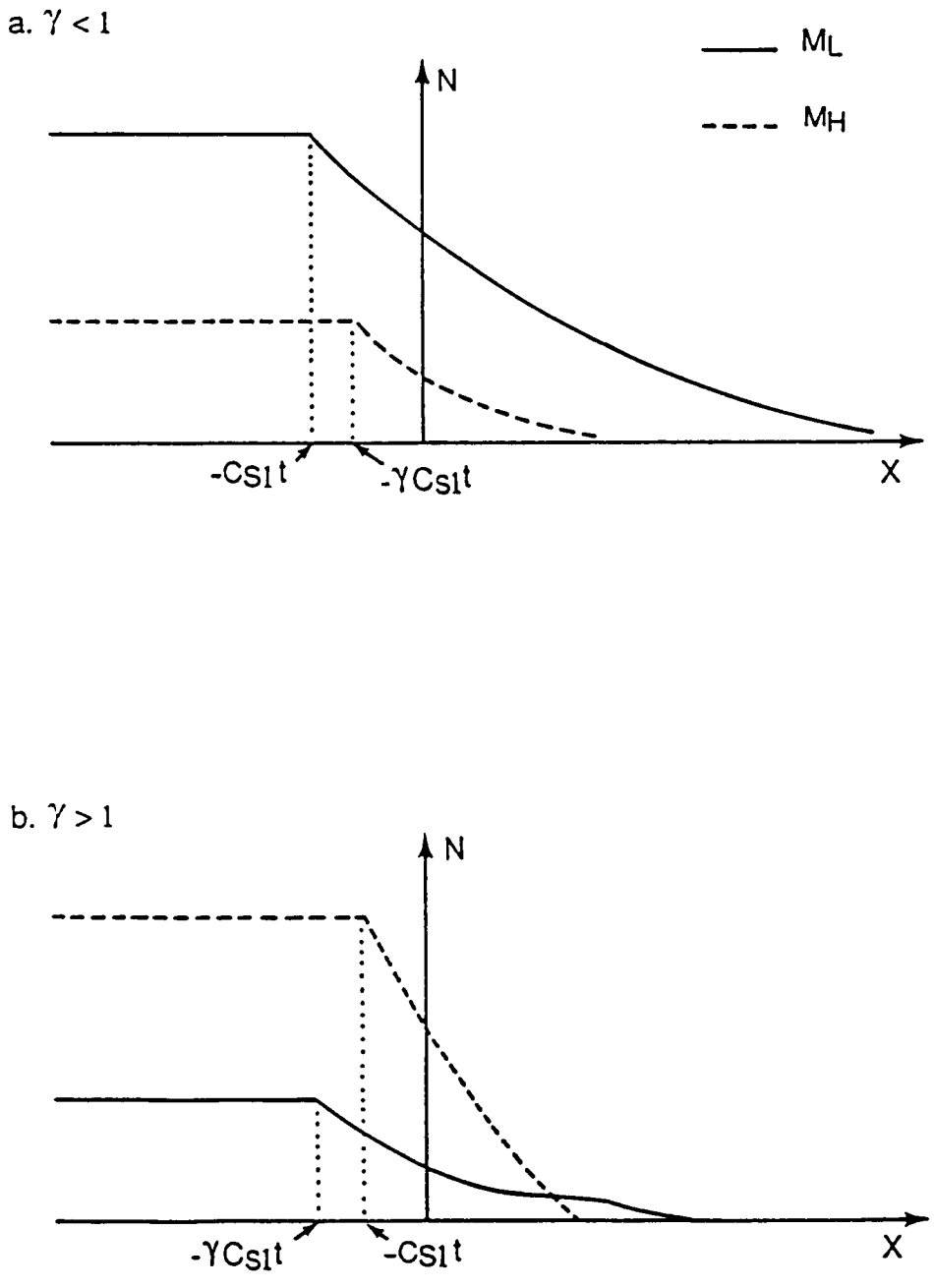

Figure 5. Ion density behavior for the binary ion plasma where $Z_1 = Z_2 = 1$, $M_L =$ the lighter ion mass, and $M_H =$ the heavier ion mass. (a) $\gamma < 1$. (b) $\gamma > 1$.

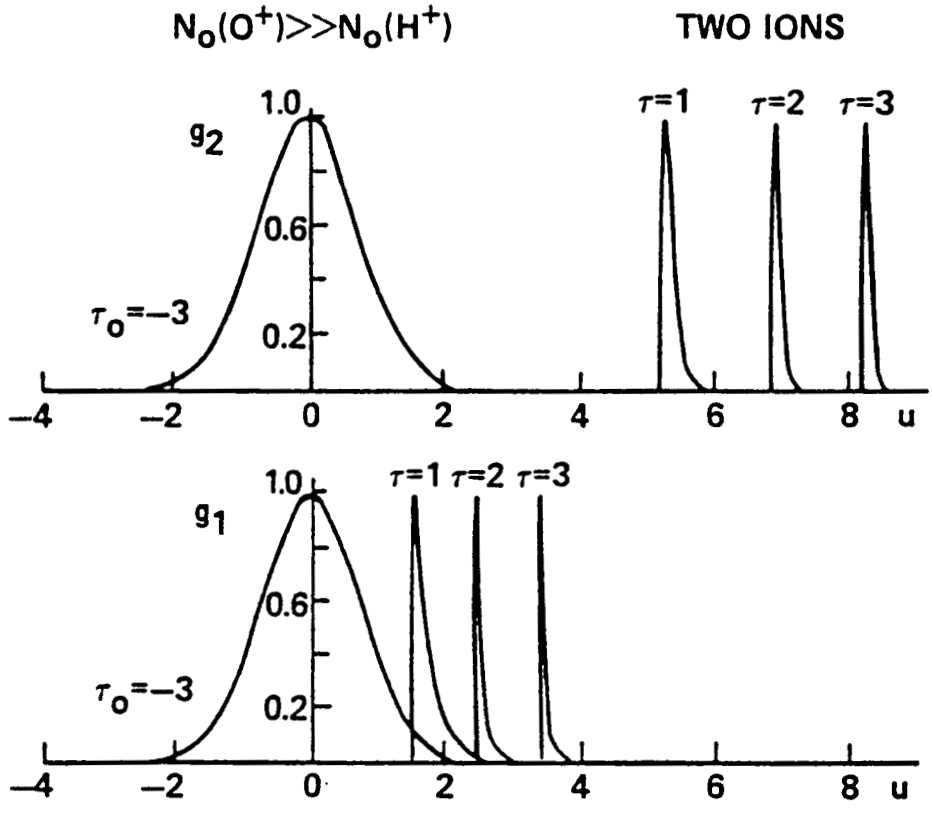

Figure 6. The variation of normalized distribution functions $g_1(O^+)$ and $g_2(H^+)$ with normalized velocity u for different values of τ. The plasma consists of two ionic species and one electron temperature for the case $n_{10}(O^+) \gg n_{20}(H^+)$, where n_{10} and n_{20} are the ambient densities of the two ionic species (after *Gurevich et al.* [1973*a*]).

the computer simulation kinetic, charge separation treatment of *Singh and Schunk* [1983*a*], the basic qualitative effects remain similar. These differences increase as the T_e/T_i ratio is increased. The width of the plateau region depends only on γ; i.e., the charge to mass ratios. Beyond the plateau region the hydrogen behaves as in the expansion of a single ion component plasma.

Gurevich et al. [1973*a*] predict oscillations to occur behind the ion front. These become more pronounced in hydrogen for $T_e > T_i$ and for certain ambient component density ratios. Differential streaming of the two ion species provides the free energy for any instabilities that may develop. Oscillations have been reported in the velocity spectra of the blow-off from laser-pellet interaction experiments [*Decoste and Ripin*, 1978; *Gurevich et al.*, 1979]. However, the study of *Singh and Schunk* [1983*a*] does not show the presence of any ion acoustic oscillations in their kinetic numerical simulation which includes Poisson's equation. A detailed analysis of the ion distribution functions was not performed by *Singh and Schunk* [1983*a*] to possibly understand the stability of the expanding plasma.

Experimental results for an argon-helium plasma expansion are shown in Figure 7 (again from *Eselevich and Fainshtein* [1981]). The density of helium is approximately 3 to 6 percent of the total ion density. For this plasma, $M_1 = Ar^+$ and $M_2 = He^+$, so that, from (2.9), $\gamma = 10$. Figure 7*a* shows the distribution function measured at the argon ion front at two positions, $x_2 > x_1$, from the plasma source. Two peaks are observed, corresponding to each ion, for each position. (*Eselevich and Fainshtein* [1981] state that the relative amplitude of the distribution function for x_2 is actually one-seventh of the amplitude at x_1.) Note the relative motion between helium and argon and that helium is accelerated more than argon in moving from x_1 to x_2. In Figure 7*b*, the variation of the time integrated ion current with $\sqrt{E_i}$, where E_i is the ion energy, is shown. The open circles are the ion current integrated for a time t at position x_2 from the plasma source for a

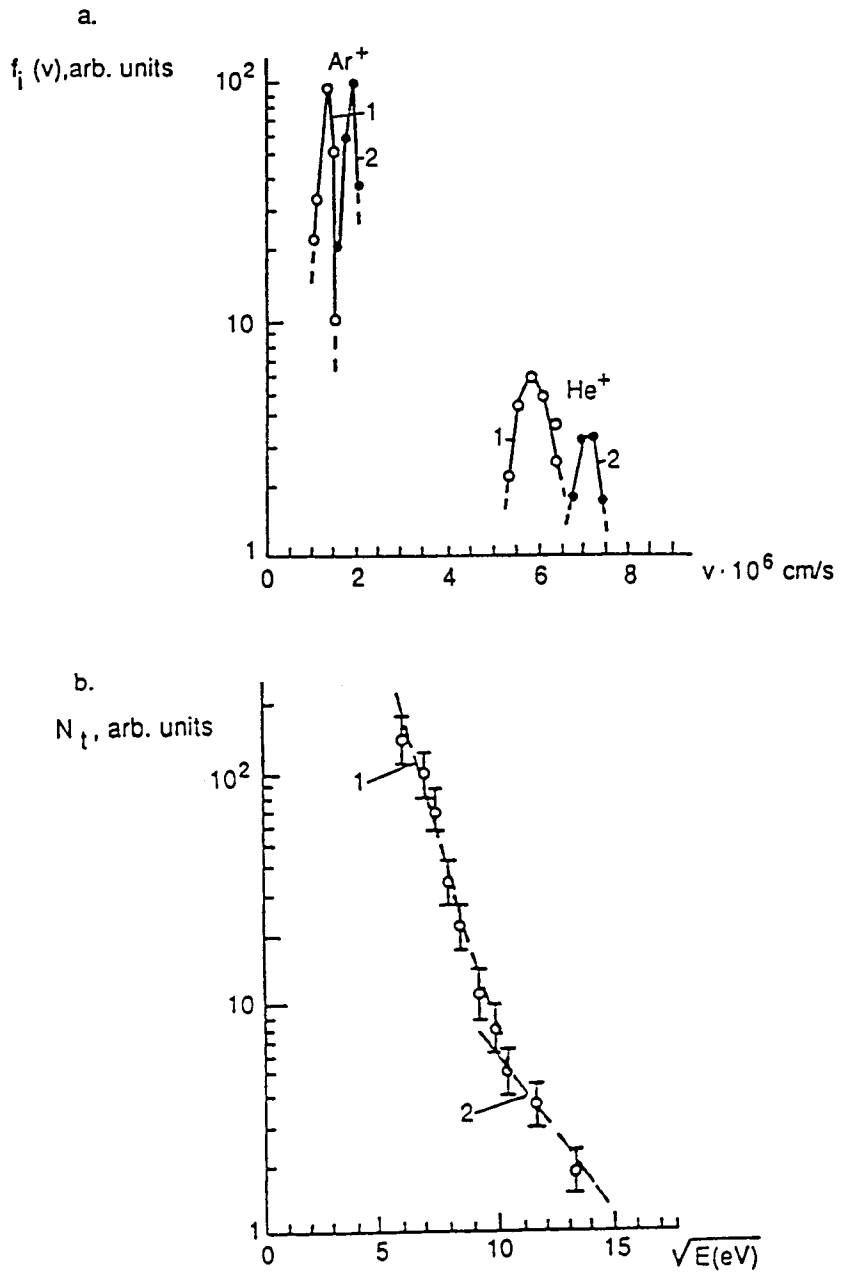

Figure 7. (a) Ion velocity distribution function in an argon - helium plasma at the argon ion expansion front at two distances ($x_2 > x_1$) from the plasma source, $n_0(He^+)/n_{tot} \approx 3 - 6\%$. ($b$) Time integrated ion flux versus $\sqrt{E}$, where E = ion energy. $N_t = \int j\, dt$. Dashed lines 1 and 2 are self-similar theory for $\gamma = 1$ and $\gamma = 10$, respectively. The figure is after *Eselevich and Fainshtein* [1981].

particular voltage (energy) setting of the detector. The dashed lines 1 and 2 indicate theoretical predictions, which are derived below [*Eselevich and Fainshtein*, 1981]. The measured value for the y-axis can be represented by $N \equiv \int j\,dt = \int nv\,dt$. For line 1, corresponding to Ar^+, integration of the product of (2.2) and (2.3) gives

$$N_1 \approx N_{10}\left(\frac{2E_1}{Z_1 kT_e}\right)^{-1/2} \exp\left[-\left(\frac{2E_1}{Z_1 kT_e}\right)^{1/2}\right]. \tag{2.12}$$

For line 2, corresponding to He^+, integrating the product of (2.10) and (2.11) gives

$$N_2 \approx \frac{N_{20}}{\gamma}\left(\frac{2E_2}{\rho kT_e}\right)^{-1/2} \exp\left[-\left(\frac{2E_2}{\rho kT_e}\right)^{1/2}\right], \tag{2.13}$$

where $\rho = \gamma Z_2/2$. Both (2.12) and (2.13) are derived under the assumption $E/Z \gg T_e$. The agreement between the data and (2.10) and (2.11) shows the general self-similar nature of the flow and the relatively higher acceleration of the lighter helium ions.

In summary, the various studies above using both fluid and kinetic treatments with and without the assumption of charge neutrality have shown that upon the expansion of a plasma into a vacuum:

(1) Ions are accelerated to high energies.

(2) A rarefaction wave is created which propagates into the ambient plasma.

(3) An ion expansion front moves into the vacuum region.

(4) The asymptotic behavior of the plasma flow is self-similar.

(5) Excitation of instabilities and plasma waves over certain volumes in space take place.

(6) Strong (or jump) discontinuities in the plasma occur at the expansion front.

The quantitative significance and intensity of the above phenomena and processes depend, in part, on the specific ionic constituents of the plasma and the relative concentration of the minor ion in the plasma; on the ambient electron temperature(s); on the ratio of a characteristic linear dimension to the Debye length; and on the density gradient at the plasma-vacuum interface.

CHAPTER III. SINGLE ION PLASMA WAKE EXPERIMENT

To investigate plasma expansion into a wake, a conceptually simple experiment was performed. A large, thin conducting plate was immersed in a mesosonic plasma flow. The subsequent plasma flow throughout the wake was measured, with particular emphasis on the ion behavior. The results are compared with the phenomena resulting from the 'plasma expansion into vacuum' process discussed in the preceeding chapter.

A. Experimental facility

Both the single ion and binary ion plasma experiments were conducted in one of the space plasma research facilities located at the NASA Marshall Space Flight Center. A cylindrical plasma wind tunnel (0.6 m diameter and 1.6 m long) is evacuated with two, 10 in. LN_2 baffled oil diffusion pumps which are backed by a 50 cfm rotary, piston type mechanical pump. The LN_2 cold traps serve to prevent backstreaming of oil vapor from the diffusion pumps. Typical base pressure attained for the single ion plasma experiment was $\simeq 7 \times 10^{-7}$ Torr. This facility has previously been referred to as MSFC No. 2 in *Stone* [1981*a*].

The plasma source, an electron bombardment type with an emissive wire neutralizer, is mounted in an appendage attached to one end of the chamber (see Figure 8). The source is operated in a continuous manner, thus requiring a continuous introduction of neutral gas into the discharge region. A sufficiently high current is passed through a tungsten ribbon cathode to heat it to the point of electron emission

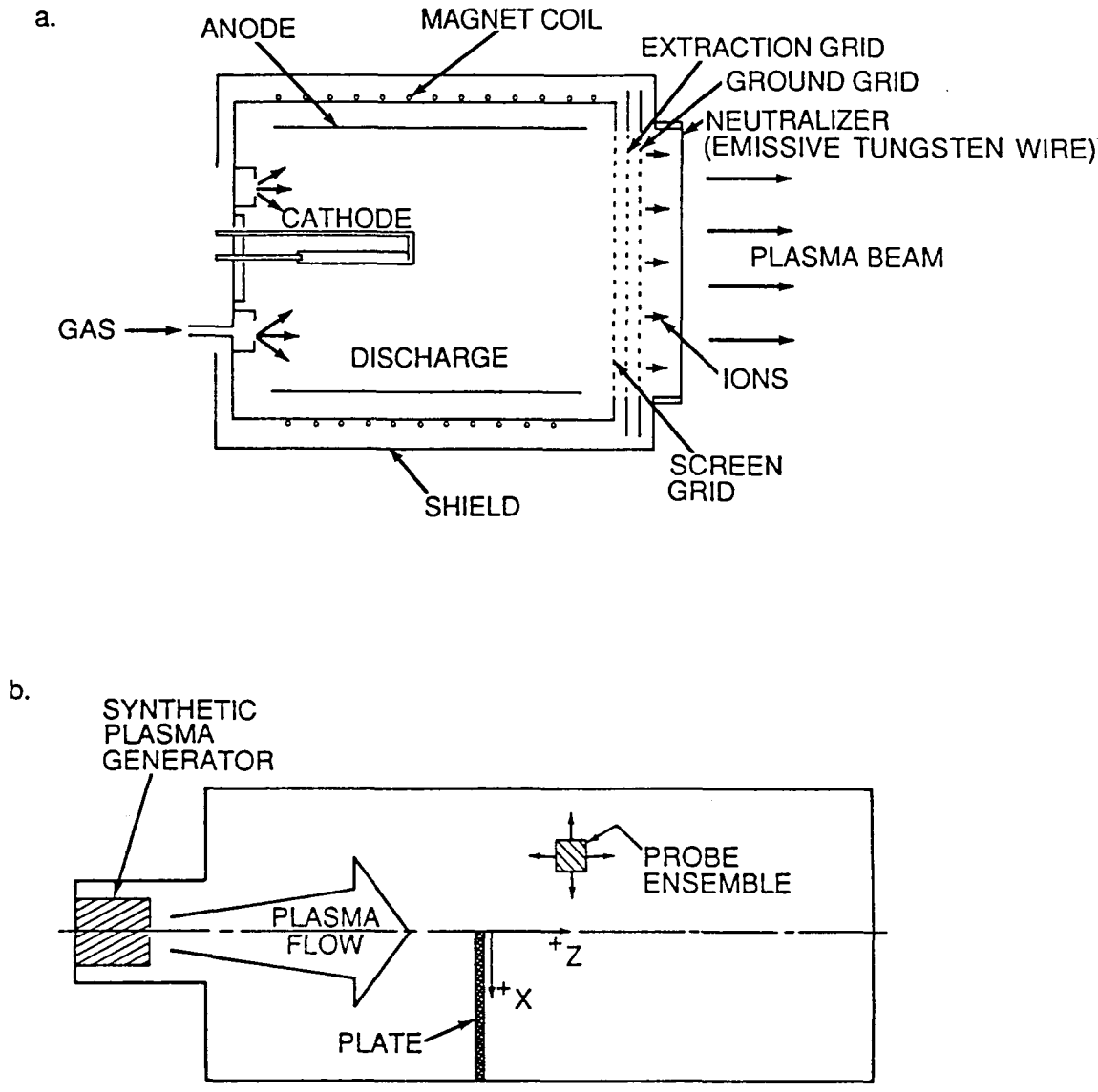

Figure 8. (*a*) Schematic of electron bombardment ion source (after *Stone and Rehmann* [1970]). (*b*) Schematic of experimental arrangement. Plasma is incident on a grounded plate whose edge lies on the vacuum chamber centerline. The origin of the indicated co-ordinate system is the plate edge (after *Wright et al.* [1985]).

from its surface. These electrons accelerate from the externally biased cathode and ionize the surrounding gas. To increase the electron residence time in the discharge region and the ionization efficiency, an azimuthal drift is imposed by an axial magnetic field and a radial electric field resulting from the anode potential. The ions are extracted by a voltage applied to the extraction grid and possess a kinetic energy near the applied anode potential. (The source for the single ion plasma has no screen grid.) The ions pass over an emissive tungsten wire, which provides electrons for the neutralization of the beam, and hence, a plasma flow is obtained. Details on this type of 'synthesized plasma stream' can be found in *Reader* [1964] and *Le Vaguerese and Pigache* [1971]. For this experiment, diatomic nitrogen was used as the working gas.

A probe ensemble was mounted on a traveling device that could be maneuvered in the direction along the chamber axis ($+z$ direction going away from the source) and in the direction transverse to the chamber axis ($+x$ direction to the right looking downstream) (see Figure 8*b*). The y direction is then out of the page in Figure 8*b*. Readouts from resistive slide wires were used to determine the actual position of the probes. Thus, the probe measurements were able to map the (x, z) plane indicated in Figure 8*b*. The probe ensemble consisted of three instruments: a guarded cylindrical Langmuir probe (0.14 cm in diameter and 3.9 cm in length), a gridded Faraday cup (0.125 in. diameter aperture with a 90 degree field of view), and a Differential Ion Flux Probe (DIFP) (0.5 cm by 2 cm aperture with a 5 degree geometric acceptance window that was electronically swept over 100 degrees angular range). See Appendix C for more detail about the probes. The Faraday cup and DIFP were mounted such that the instrument normals were parallel to the chamber axis (z axis), while the Langmuir probe axis was along the y direction.

The DIFP is an instrument specifically designed for use in body-plasmadynamic interaction experiments [*Stone*, 1977]. It has been successfully used in the

laboratory [*Stone*, 1981*a*,*b*], on the STS-3 and Spacelab 2 space shuttle missions [*Stone et al.*, 1983; *Stone and Wright*, 1985; *Stone et al.*, 1986], and on sounding rockets. The DIFP provides two-dimensional measurements of the vector ion flux in a plane that contains the instrument normal and is perpendicular to the collimation slits. The angular range is ± 50 degrees with respect to the instrument normal with one degree resolution (see Appendix C.3). For this experiment, the DIFP was oriented so that the measurements were made in the (x, z) plane.

The data collection sequence was performed as follows. The diagnostic probe array was moved to a downstream position from the source. The probe array, beginning at the most negative x position, was moved continuously in the $+x$ direction. The output of an electrometer connected to the Faraday cup was recorded versus position along the x axis on an X-Y plotter which has a 1 kHz low pass filter. After a transverse current profile was completed, the probes were moved back to various x positions of particular interest which were marked on the transverse current profile. Vector ion flux measurements were then made at these positions with the DIFP. The Faraday cup was located on top of the DIFP, so the two instruments always had the same x and z positions. The above sequence was repeated for various downstream locations from the plate. The Langmuir probe measurements were made at various times and locations in the plasma flow during the experiment.

B. Free-stream characteristics

In general, the plasma streams generated in the laboratory are neither uniform nor isotropic. Effects which contribute to the deviation from ideal characteristics are: charge exchange interactions with background neutrals, stream divergence, non-neutralized beam, anisotropic (and non-Maxwellian) ion thermal motion, and absorption of charge at the chamber walls. These limitations must be kept in mind

when interpreting results from plasma flow experiments.

Charge exchange interactions between the stream ions with the background neutrals produce a stream of fast neutrals and a slow ion background with no preferred direction. The slow ions are a function of chamber size and the residual neutral gas pressure. The operating pressure for the free-stream measurements and the experiments was $\approx 9 \times 10^{-6}$ Torr. From *Stone* [1981*a*], an estimate for the percentage of slow ions can be attained, $n_s/n_f \simeq 0.1$, where n_s = the density of slow ions and n_f = the density of fast (or stream) ions. This value is above the suggested acceptable value of $n_s/n_f \leq 0.03$ [*Oran et al.*, 1976]. Measurements obtained from the DIFP showed no extra deflection peaks or the presence of a low energy 'step' on the retarding potential curve . Therefore, no slow ions were present in levels above the instrument sensitivity limitation.

The plasma stream divergence depends on the properties of the plasma near the source exit. The initial acceleration process introduces a divergence (ratio of the transverse velocity component to the component parallel to the chamber axis) as do space charge potentials within the stream (due to imperfect neutralization). These effects become more pronounced as the source radius and beam energy are reduced. The extraction plate of the single ion plasma source consisted of one hole with a 3/16 in. radius (a relatively small radius). Beam energies were < 20 eV. Figure 9 shows an example of the evolution of the ion current. The normalized ion current density versus transverse position (x) is plotted as a function of distance downstream (z) from the source. For each z position, the current used for normalization is the maximum value at that downstream position and is observed to vary approximately as $1/z^2$ from the source exit. There is some beam asymmetry due to ions having a larger divergence for $-x$ than for $+x$. This is seen in Figure 10. The magnitude of the angle, relative to the chamber axis, measured by the DIFP is plotted versus transverse position. The divergence of the beam for $-x$ values is approximately

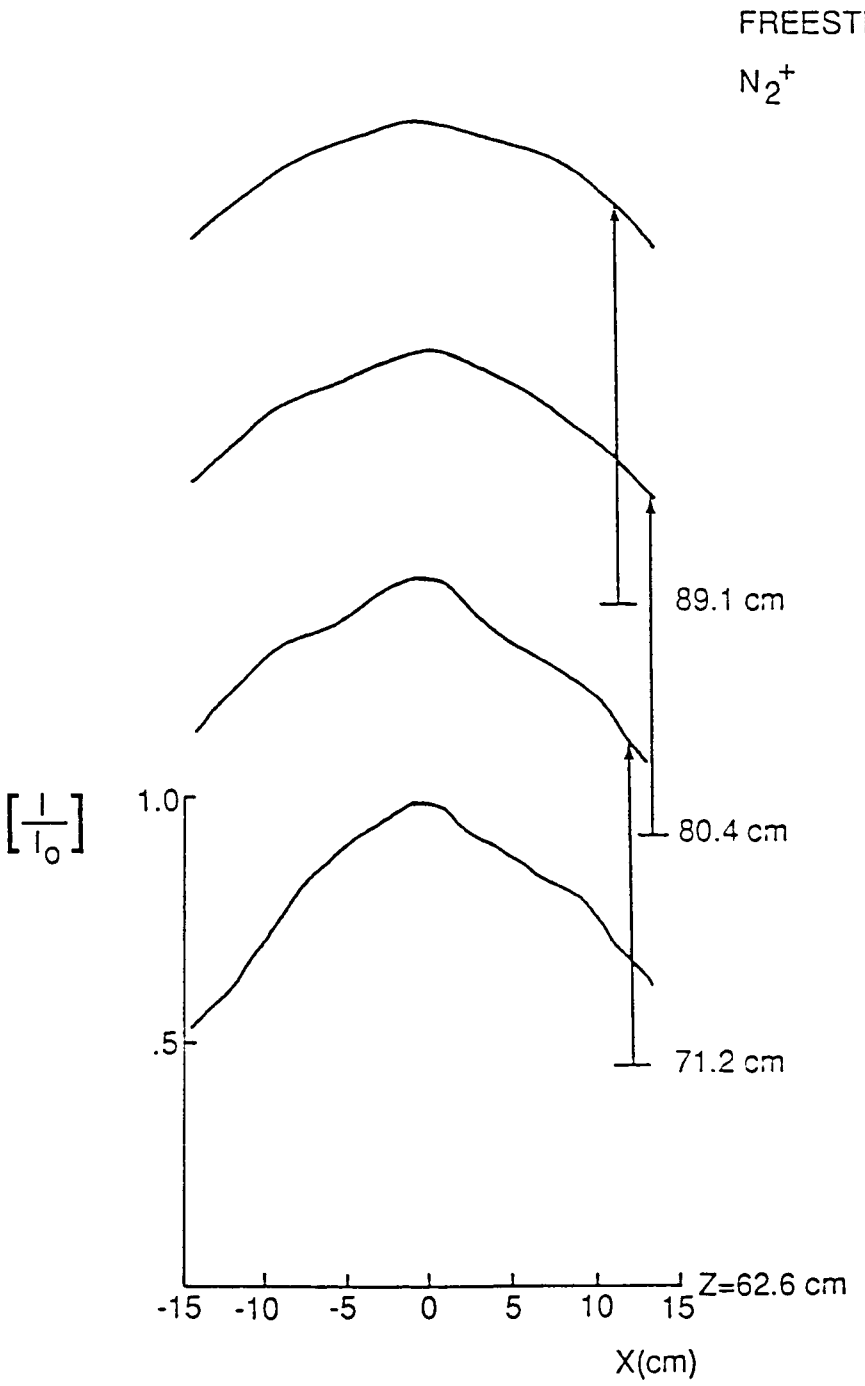

Figure 9. Freestream variation of the normalized ion current density (I/I_0) with transverse position (x) for several downstream distances (z) from the plasma source.

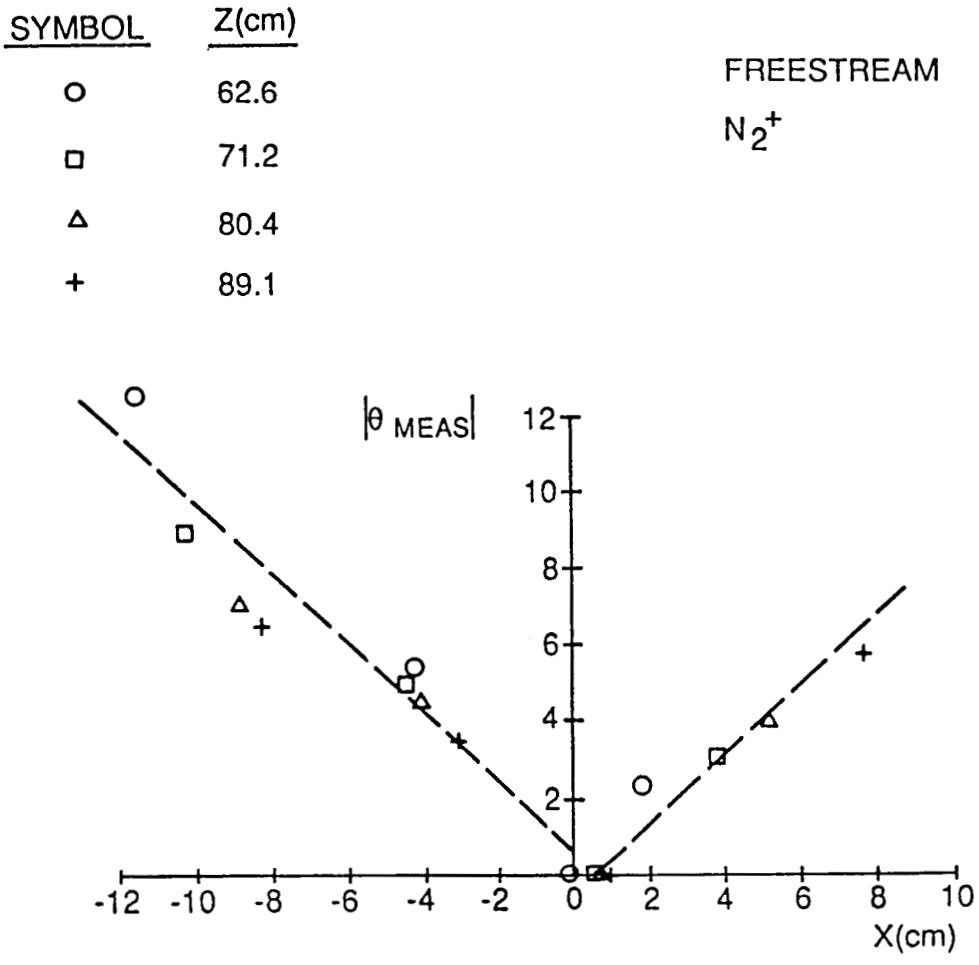

Figure 10. Freestream variation of $|\theta_{meas}|$, as determined by the DIFP, with transverse position (x) for several downstream distances (z) from the plasma source.

$\Delta\theta/\Delta x \simeq 1.0°$ per cm. The motion of the $I/I_0 = 0.8$ point for $-x$ values indicates a divergence of 10.5 degrees. This is a moderate value for the introduction of divergence effects into experiments.

In general, the parallel and perpendicular ion temperature are not equal due to the potential structure in the discharge region of the source and the geometry of the ion extraction. In Appendix C.3.a, the retarding potential curve is fit with a drifting Maxwellian ion stream [*Whipple*, 1959] and yields an effective parallel beam temperature of $T_{i_\parallel} \simeq 0.033\,\text{eV}$. The perpendicular ion temperature was not directly measured; however, an estimate for its value can be made based on the approximate expression developed by *Hester and Sonin* [1970]:

$$\overline{C}_{i_\perp} = \frac{4V_{flow}}{3\pi}(R_S/z), \tag{3.1}$$

where $\overline{C}_{i_\perp}$ = the mean ion thermal speed, V_{flow} = drift velocity of the plasma stream, R_S = source radius, and z = distance from source. The mean ion thermal speed is given by $(8kT_i/\pi M_i)^{1/2}$; then the effective transverse ion temperature (in eV) is given by

$$[T_{i_\perp}]_{eff} = \left(\frac{4}{9\pi}\right)\phi_{acc}(R_S/z)^2, \tag{3.2}$$

where ϕ_{acc} = accelerating potential for the ions. For the source radius of 3/16 in., an 18 eV beam at distances of 50 cm and 100 cm from the source gives $[T_{i_\perp}]_{eff} \simeq 2.3 \times 10^{-4}\,\text{eV}$ and $5.8 \times 10^{-5}\,\text{eV}$ respectively, implying essentially parallel ion flow.

If space charge effects on the beam are ignored, then another estimate for $[T_{i_\perp}]_{eff}$ can be made. Let the difference between the measured angle ($\theta_{meas.}$) at a point (x, z) and the geometric ray from (x, z) to the source be $\Delta\theta = \theta_{meas.} - \tan^{-1}(|x|/z)$. Then assume $\Delta\theta \simeq V_{i_{th}}/V_{flow}$, where $V_{i_{th}} = (2kT_{i_\perp}/M_i)^{1/2}$ = the ion thermal speed, $V_{flow} = (2eE_d/M_i)^{1/2}$ = the stream drift velocity, and $\Delta\theta$ in radians. Then $\Delta\theta \simeq (T_{i_\perp}/E_d)^{1/2}$. For the freestream measurements in Figure 10, an average $\langle\Delta\theta\rangle = 1.1°$, implying that $[T_{i_\perp}]_{eff} \simeq 0.005\,\text{eV}$. The beam is thus concluded to have negligible perpendicular ion thermal motion.

The electron temperture (T_e) values did not show much variation with position. T_e values for all x, z were within 15% of an average $\langle T_e \rangle$ value. Some systematic tendancy for $T_e(+x) > \langle T_e \rangle$ existed. Using $\langle T_e \rangle$ for the purposes of calculating plasma properties and parameters was assumed to valid. The space potential, which can be adjusted higher or lower by varying the source parameters, was determined by the inflection point method (see Appendix C.2) to be $\phi_{sp} \simeq -1$ to 0 volts. This value indicates an electron rich plasma.

C. Results and discussion

The experimental setup is shown schematically in Figure 8*b*. A large, conducting plate was located ≈ 96 cm from the plasma source to insure an incident plasma stream of fairly uniform density cross section (see Figure 9). The plate was mounted with an edge on the chamber axis (thus, simulating the $R_D \gg 1$ case) and was maintained at ground potential throughout the experiment. The coordinate origin for the measurements is located at the plate edge, with the $+z$ axis directed downstream and the $+x$ axis toward the 'expansion region' behind the plate; the y axis is then parallel to the plate edge. The region accessible for measurements was $-10\,\text{cm} \leq x \leq 19\,\text{cm}$ and $0 < z \leq 55\,\text{cm}$.

As mentioned in section III.A, the Faraday cup was mounted on top of the DIFP with each instrument-normal parallel to the chamber axis. The probes were mounted on the traveler mechanism at a y-position such that the halfway point between the center of the respective aperatures was on the chamber axis. The Faraday cup and the DIFP were used for ion measurements in both the ambient plasma and the region behind the plate while the Langmuir probe was used for ambient electron measurements.

The nominal conditions for the continuous, drifting N_2^+ plasma used in the experiment are shown in Table 1. The electron temperature, T_e, and plasma space potential, ϕ_{sp}, values represent an average over the ambient plasma region, while the density, n_0, pertains to the ambient value at the plate location. Other comments on notation are: the ion acoustic speed is given by $C_S = (kT_e/M_i)^{1/2}$; the Mach number is given by $\mathcal{M} = V_{flow}/C_S$; and the normalized body potential is given by $\Phi_B = e(\phi_{plate} - \phi_{sp})/kT_e$.

Table 1. Plasma conditions for the single ion experiment.

E_d(eV)	18
V_{flow}(cm/s)	1.1×10^6
n_0(cm^{-3})	1.2×10^5
T_e(eV)	0.27
T_i	$< 0.1T_e$
C_S(cm/s)	9.7×10^4
ϕ_{sp}(volts)	-0.5
$\mathcal{M}$	11.3
Φ_B	$+1.8$

In the electrostatic interaction between the flowing plasma and the plate, several mechanisms are responsible for bringing ions into the void region:

(1) deflection by electric fields existing in the sheath between the plasma and the plate edge

(2) acceleration by polarization electric fields developed from space charge effects at the plasma-void interface which extend downstream from the body

(3) diffusion from thermal motion

(4) scattering by plasma oscillations and/or instabilities

If mechanism (4) plays a role in wake filling, then the sequential acquisition of several transverse ion current profiles at the same z position should show differences between each trace. No differences, however, were observed; therefore, mechanism (4) is concluded to be unimportant. A spectral analysis was beyond the scope of the experimental investigation, so mechanism (4) was not investigated. The ambient plasma drift velocity in the experiment lies in the mesothermal regime; i.e., $V_{e_{th}} \gg V_{flow} \gg V_{i_{th}}$, where $V_{e_{th}}$ = electron thermal velocity, V_{flow} = ambient plasma drift velocity, and $V_{i_{th}}$ = ion thermal velocity. From this inequality (and remembering that $[T_{i_\perp}]_{eff}$ is the important property for thermal filling), one concludes that thermal effects, mechanism (3), cannot be a major contributor to the wake filling process within the experimentally accessible downstream distances. As stated above, the plate was maintained at ground potential. The space potential of the ambient plasma was adjusted as close to 0 volts as possible, so that mechanism (1) has essentially no effect on the wake filling process. The only remaining mechanism is the electric field due to space charge effects within the wake void. The phenomena resulting from the action of this electric field is considered in terms of the plasma expansion problem discussed in Chapter II.

As seen in Table 1, the Mach number of the plasma flow is given by $\mathcal{M} \simeq 11.3$. Since the plasma flow is at a high Mach number, there is a 'vacuum' immediately behind the plate; and hence, a strong density gradient exists. Therefore, the boundary conditions of the plasma wake immediately behind the plate are strongly suggestive of the initial conditions used in one-dimensional models of 'the expansion of plasma into a vacuum' .

The analogy between the one-dimensional, time dependent case and the two-dimensional, time-independent case is developed in Appendix D. These two cases can be made formally identical when certain assumptions are met (see *Gurevich*

et al. [1969]): the velocity v_z is independent of x and z (i.e., V_{flow} constant), $|\partial\phi/\partial x| \gg |\partial\phi/\partial z|$, and $x/z \ll 1$. Essentialy, these conditions imply that at sufficient distances from the plate edge, the analogy with plasma expansion is valid. In the present experiment, within the neighborhood of any given position, $\partial/\partial z \simeq 0$, while the small variation that does exist over larger distances in the z direction can be used as a parameter to represent time; i.e., $t = z/V_{flow}$. Further, most theoretical treatments of the plasma expansion problem assume a Boltzmann relation for electrons. Since this is also a reasonable assumption for our experiment, it is reasonable to compare the experimental results with the predictions of the one-dimensional, time-dependent theory. The vacuum chamber length and, more importantly, the plasma density limit the scale size of the experiment to an equivalent time of a few ion plasma periods. Therefore, the results elucidate only the early time evolution of the plasma expansion.

The plasma expansion process will produce high energy ions if given a sufficient spatial region, as predicted by *Gurevich et al.* [1966] and shown experimentally by *Eselevich and Fainshtein* [1979]. The above constraint on our present experiment precludes the observation of ions with energy gains of more than a few times the thermal energy. However, any velocity enhancement directed along the x axis is readily discernible with the DIFP.

Figure 11 presents typical ion current density measurements obtained from the Faraday cup. The ion current density is plotted versus x for various downstream locations, where the relative distance between z locations is drawn to scale. The normalization value of current, I_0, is chosen to be the maximum current observed at each downstream position. The negative current values result from electrometer overshoot at the bottom of the steep gradient. The point where the ion current density begins to deviate from ambient is denoted by '1' and represents the leading edge of the rarefaction wave (X_1). In the region of $x > 0$, there exists a sharp

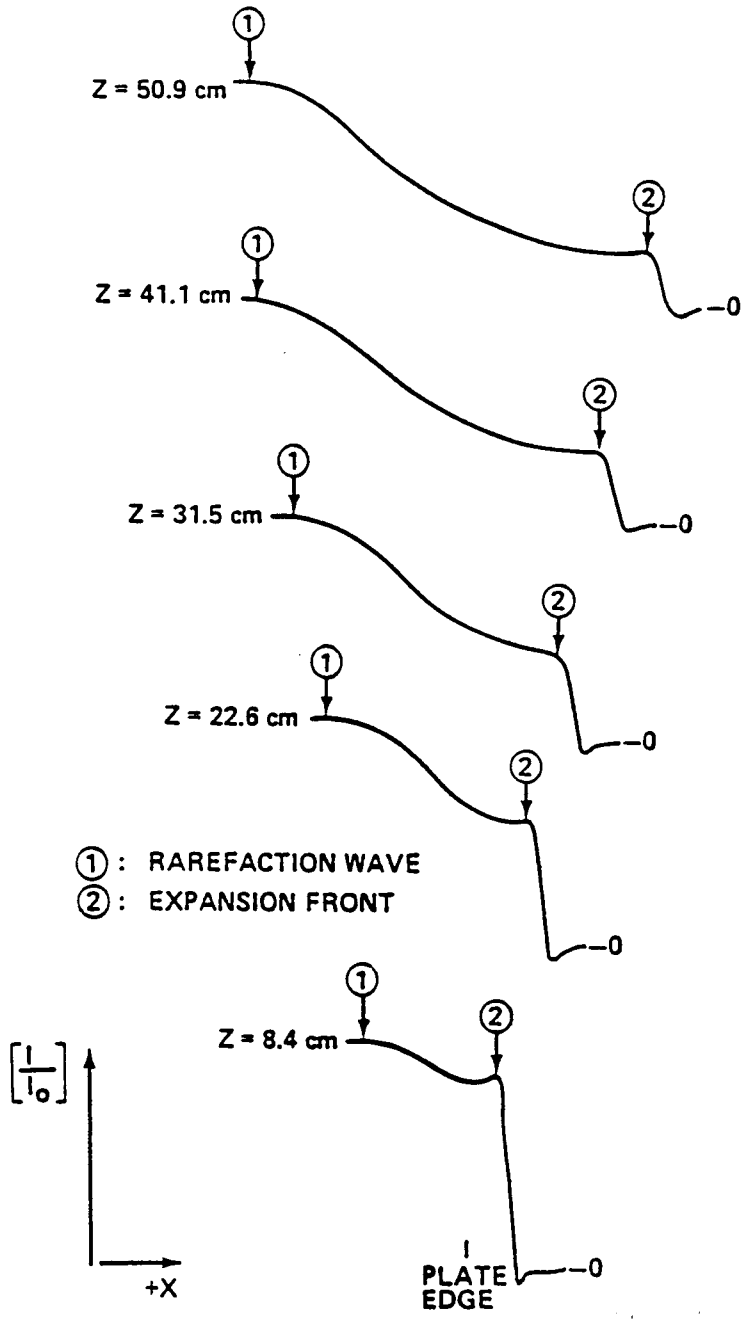

Figure 11. Variation of normalized ion current density (I/I_0) from Faraday cup with transverse position (x) at various downstream locations (z) from the plate. The zero current levels are marked on the right and the values of z in cm are on the left. $x = 0$ at the plate edge. 1, leading edge of the rarefaction wave; 2, expansion front. The figure is after *Wright et al.* [1985].

gradient in the ion current density, denoted by '2' . This gradient moves towards larger x locations further downstream at a rate to be shown later in Figure 19. This feature is the expansion front seen in numerical computations by *Crow et al.* [1975]. (In *Gurevich and Meshcherkin* [1981*a*,*b*], the expansion front is referred to as the 'leading front of the rarefaction wave'.) The expansion front was observed in several runs of this experiment and is a persistent feature of the wake in this experimental configuration.

Figure 12 presents a contour plot of the normalized ion current density shown in Figure 11. The shaded area represents the non-monotonic variation of the ion current density; i.e., the region around the local current minimum observed behind the expansion front shown, for example, in the $z = 8.4\,\mathrm{cm}$ profile of Figure 11. The motion of the rarefaction wave and of the expansion front is easily seen. In addition, the acceleration of the expansion front is indicated by the curvature of the $I/I_0 = 0.1$ contour and results in the pealing away of the contours from the expansion front.

At all downstream distances from the plate, the rarefaction wave, seen in Figure 11, was found to move into the ambient plasma at a constant speed, which very closely approximates $\sqrt{2}\,C_S$. Figure 13*a* shows this result in a plot of $\Delta X \cdot S$ versus z, where $S = \mathcal{M}/\sqrt{2} = V_{flow}/\sqrt{2}C_S$ and ΔX is given by the difference between the rarefaction wave point X_1 and the initial disturbance point, determined by extrapolation back to the plate location at $z = 0$. In the theory illustrated in Figure 2, a propagation speed of C_S is shown. The important physical point to note is that the plasma disturbance moves at a rate determined by properties of both constuituents; i.e., a property of the electrons (T_e) and a property of the ions (inertia or M_i). Previous measurements of rarefaction waves associated with supersonic body-plasma interactions in the laboratory [*Stone et al.*, 1978] are shown in Figure 13*b*, presented in a similar manner. ΔW is given by $[W(z) - W_0]/2$, where

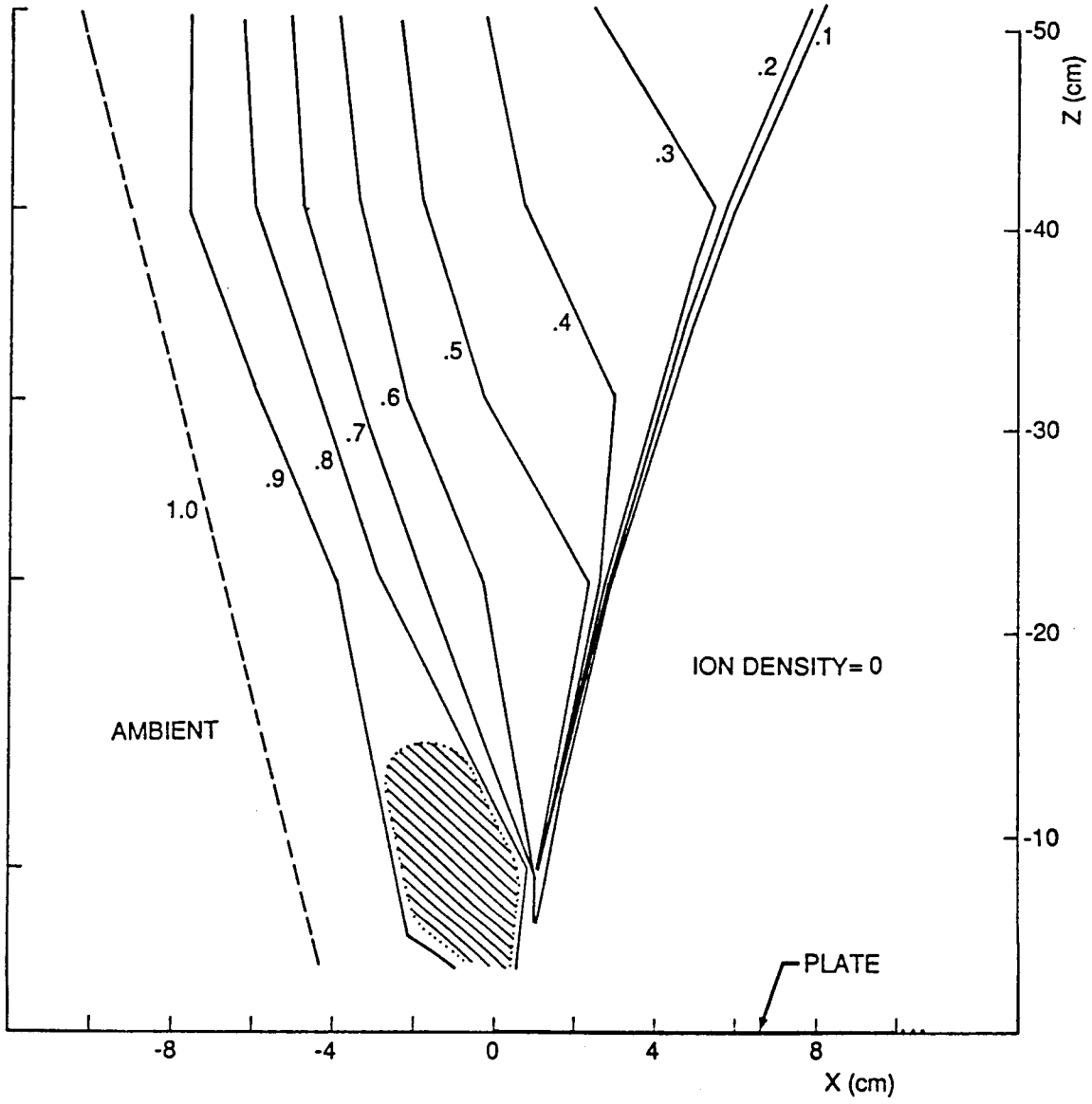

Figure 12. Contour plot of the normalized ion current density shown in Figure 11. The shaded area represents the non-monotonic variation of the current.

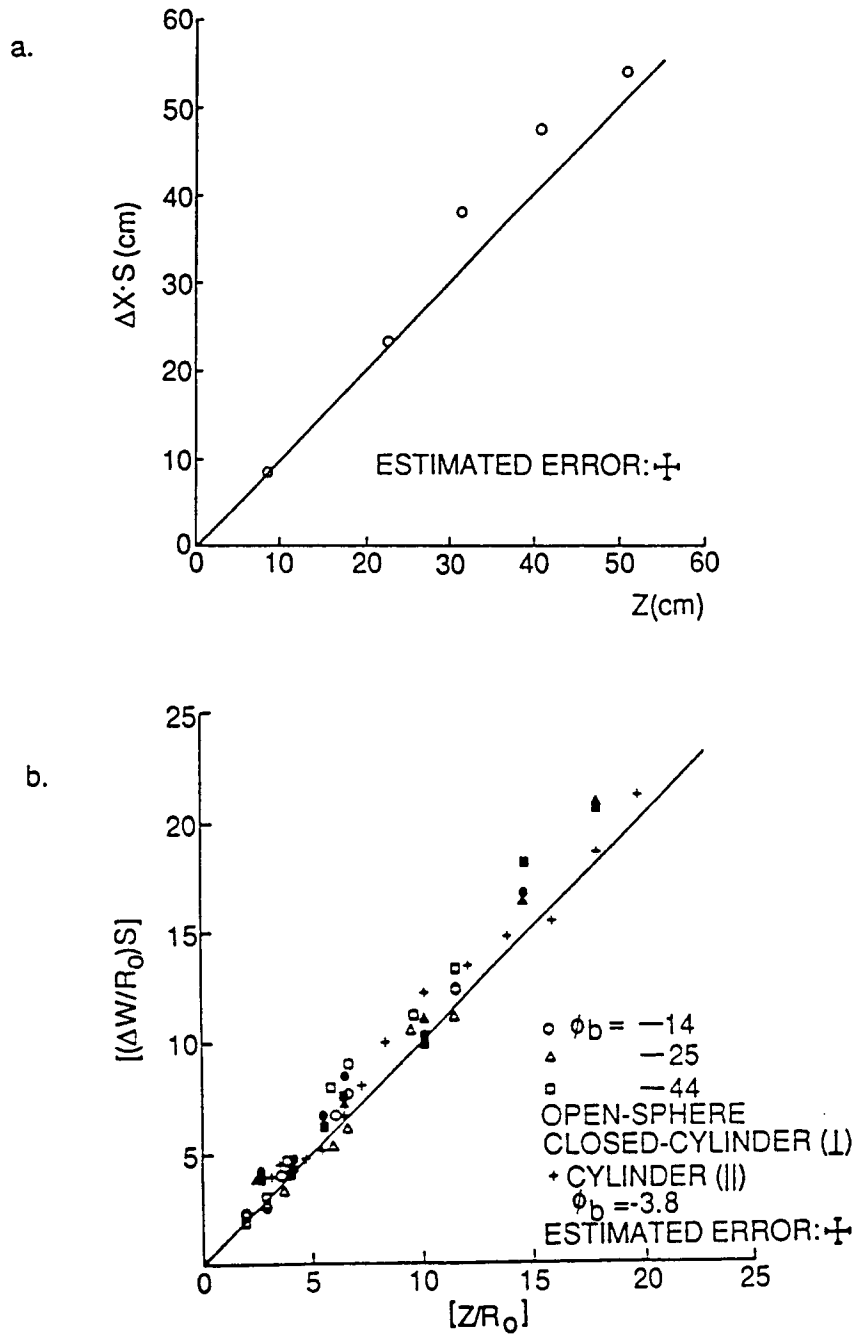

Figure 13. (a) Motion of the rarefaction wave point ΔX times S versus downstream position for the normalized current profiles shown in Figure 11. (b) Growth of the disturbed zone ΔW, normalized by R_0/S, with normalized downstream distance (z/R_0) (after *Stone et al.* [1978]).

$W(z)$ = the wake disturbance width at position z and W_0 = the initial disturbance width at the body location. ΔW and z are each normalized by the body radius R_0. The data were obtained for various body potentials and test body shapes and are seen to be independent of those properties for the small size bodies used ($R_D < 5$). This result is in agreement with an earlier theoretical treatment of body-plasma electrostatic interactions by *Martin* [1974]. The rarefaction wave motion is thus fundamental to this interaction.

Equation (2.2) predicts the ion density profile to have an exponential dependence or a concave shape. Since the plasma stream was highly supersonic and the transverse expansion velocity attained values $< 3C_S$ (see Figure 19), the resulting net increase to the total ion velocity was small. Therefore, the variation in ion current density ($\mathbf{j} = n\mathbf{v}$) with x position shown in Figure 11 is mostly due to the variation in ion number density rather than velocity. The curves between the points designated by the rarefaction wave point and the expansion front have the concave shape, but are not exponential. Ions in this region between the rarefaction wave and the expansion front did not originate from the same ambient density level. Recall the $1/z^2$ density variation in the ambient plasma mentioned in section III.B. Therefore, one must be cautious in comparing this experiment data with plasma expansion theories, which assume a constant ambient density. In addition, the exponential behavior for ion density is an asymptotic state, which may not apply for the equivalent early times of the present experiment. It is noted that profiles of ion density in the wake of a 'finite scale size' plate obtained in the experiment by *Alikhanov et al.* [1971] show the concave shape similar to the profiles in Figure 11 for comparable expansion times and also show the existence of an expansion front. However, in the experiment by *Raychaudhuri et al.* [1986], the observed ion density profiles, also in the wake of a 'finite scale size' plate, could be described by the self-similar exponential behavior of (2.2). The equivalent expansion times for

the *Raychaudhuri et al.* [1986] experiment were over an order of magnitude larger than for the present experimental situation, and the self-similar behavior could be obtained.

The ion current density at the expansion front, I_F, was observed to decrease with increasing downstream distance (or increasing time, since $t = z/V_{flow}$). This result is illustrated in Figure 14 in terms of normalized quantities. The current used to normalize I_F and the ion number density used in ω_{pi}, the ion plasma frequency, are chosen to be the ambient values at the location of the plate. The reason for this selection is that the expansion front consists of particles which originated near the plate edge. Any effect of the $1/z^2$ ambient current density variation on the expansion front is communicated by the electrons via changes in the local electric field at the front. It is the electron pressure gradient which maintains the expansion electric field (see Chapter II). Plasma expansion theory assumes a constant ambient number density; therefore, by using constant normalization factors, a valid comparison is allowed with the theory. *Gurevich and Meshcherkin* [1981*b*], which considers charge separation effects through Poisson's equation, predicts that the variation of ion density at the front with time should be $1/t^2$. This prediction is shown by the solid curve in Figure 14. At the longer times of the present experiment, the ion current density (and, hence, the ion number density as noted in the preceeding paragraph) is seen to follow generally the $1/t^2$ behavior.

DIFP measurements of the ion flow direction in the wake region are presented in Figure 15. The ambient region contains the natural divergence of the plasma stream. The rotation of the ion flow vectors with increasing z within the expansion region is quite evident. This indicates an increase in the x component of the ion velocity that results from acceleration of the ions by the expansion electric field noted in the above paragraph and discussed in Chapter II. The measurements obtained at the expansion front are indicated by the arrows at the largest $+x$ positions. If there

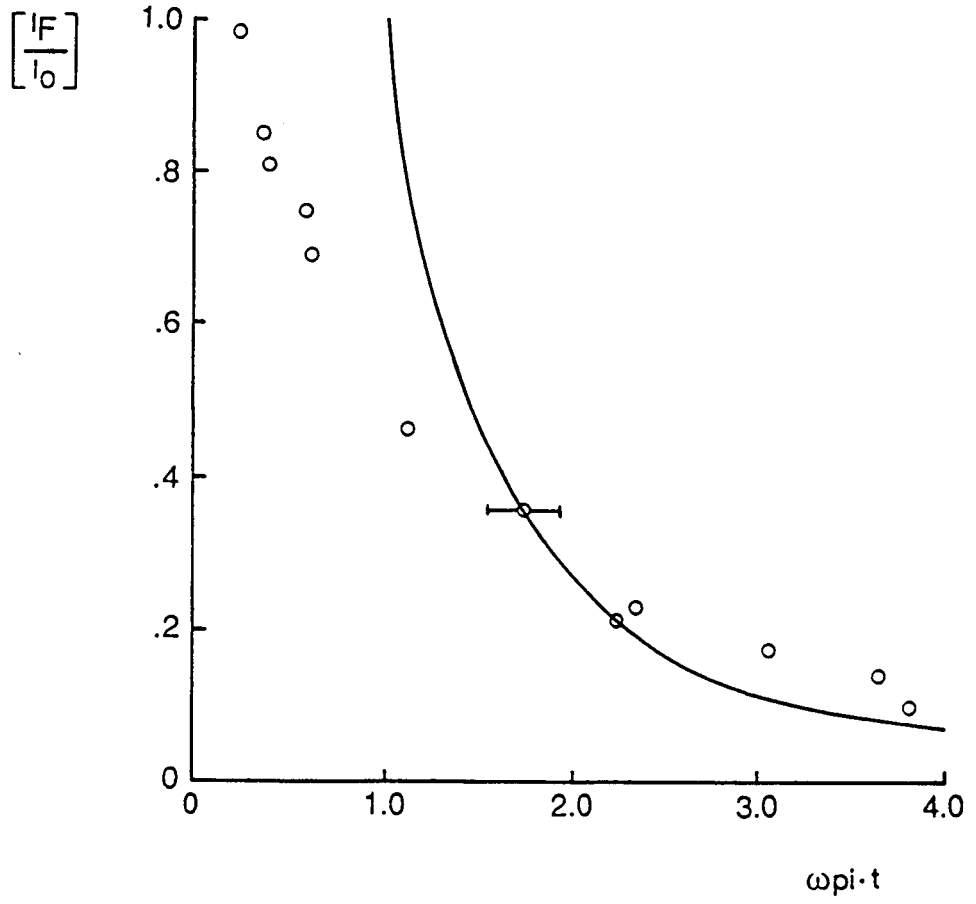

Figure 14. Variation of the normalized ion current density at the expansion front, I_F/I_0, with time, normalized by the ion plasma frequency, ω_{pi}. The values for I_0 and the density used the calculation of ω_{pi} are obtained from the ambient plasma at the plate location. The solid curve indicates a $1/t^2$ dependence.

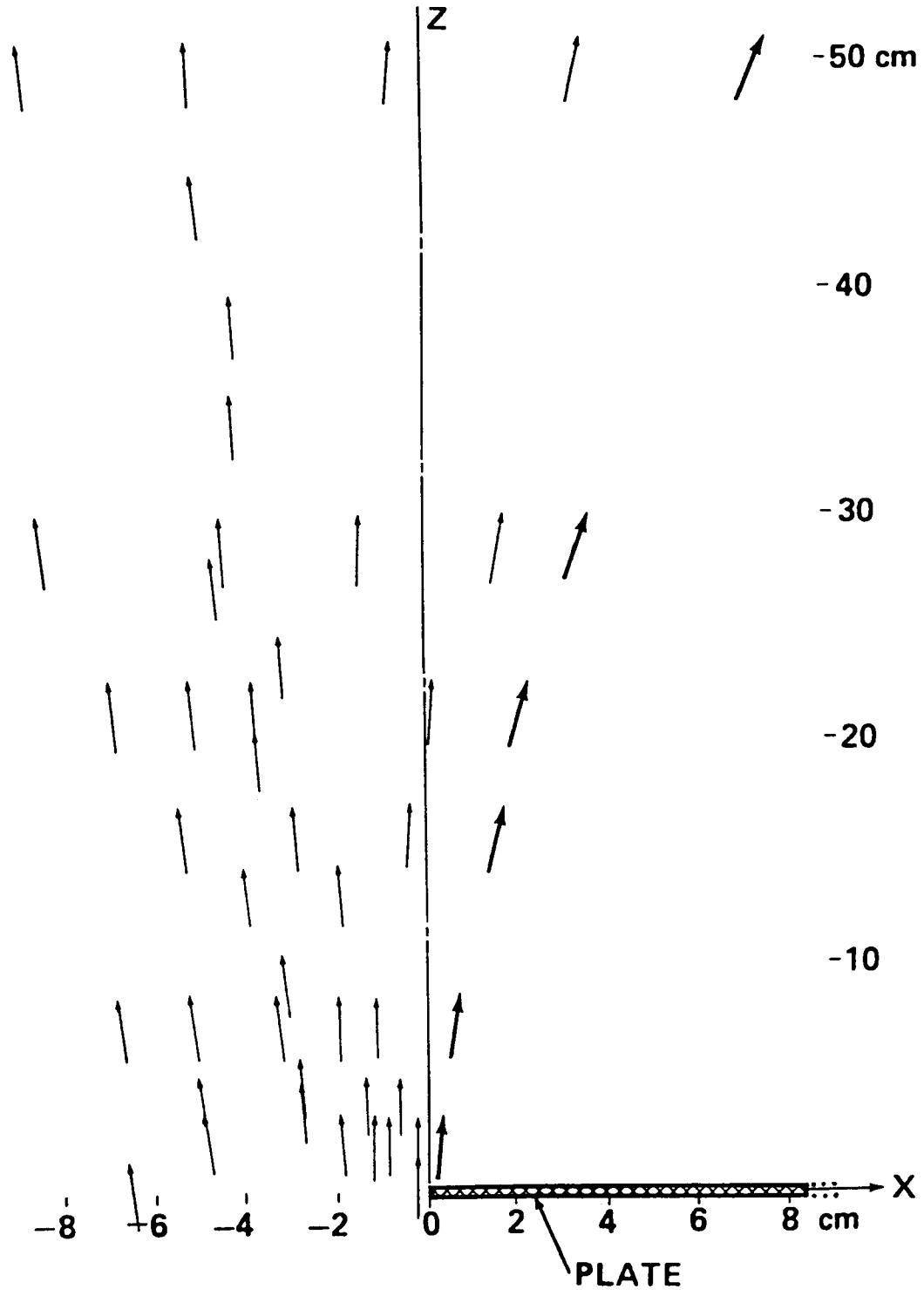

Figure 15. Ion velocity flow field measurements from the DIFP. Measurement location is at the tip of the vector. The figure is after *Wright et al.* [1985].

were flow around the opposite edge of the plate, the locations of the expansion fronts would define the region of maximum rarefaction, or the void boundary shown in Figure 1, in the wake of a 'finite' body [*Gurevich and Meshcherkin*, 1981*b*]. The behavior in the mid-wake region of such a case would be determined by the collisionless interaction of the two expansion fronts.

The action of the expansion electric field is illustrated in Figure 16. This is a plot of the expansion front position normalized by the Debye length, λ_D, versus time normalized by the ion plasma frequency, ω_{pi}. The density used in calculations for λ_D and ω_{pi} is the ambient value at the plate location, based on the reasons given in the discussion for Figure 14. The curvature of the data indicates a positive second derivative, implying the existence of a force directed toward the expansion region. The solid line illustrates constant motion at the ion acoustic speed, C_S. Therefore, the expansion front motion is seen to exceed the speed C_S.

At a downstream distance of $z = 22.4\,\mathrm{cm}$ (an equivalent expansion time of $\omega_{pi}t = 1.7$), the response of the ions to a change in plate potential was recorded. Figure 17 shows the normalized transverse ion current profiles for both $\phi_{plate} < 0$ and $\phi_{plate} > 0$. The overall shapes of the profiles are similar, but the expansion front is observed to change position as ϕ_{plate} is varied. Figure 18 shows a plot of the normalized expansion front position versus normalized plate potential, $\Phi_B \equiv (\phi_{plate} - \phi_{sp})/kT_e$. The behavior appears to be linear, indicating the superposition of the sheath electric field with the expansion electric field. The prevalence of this behavior throughout the wake region is not known since only measurements at this one z position were obtained. For planar geometry, which this experimental set-up approximates, separation of the action of sheath and expansion electric fields into distinct, independent effects is clearer. For smaller, finite-sized objects where spherical geometry best describes the physical situation, the separation of the action of sheath and expansion electric field effects may not be apparent due to ion

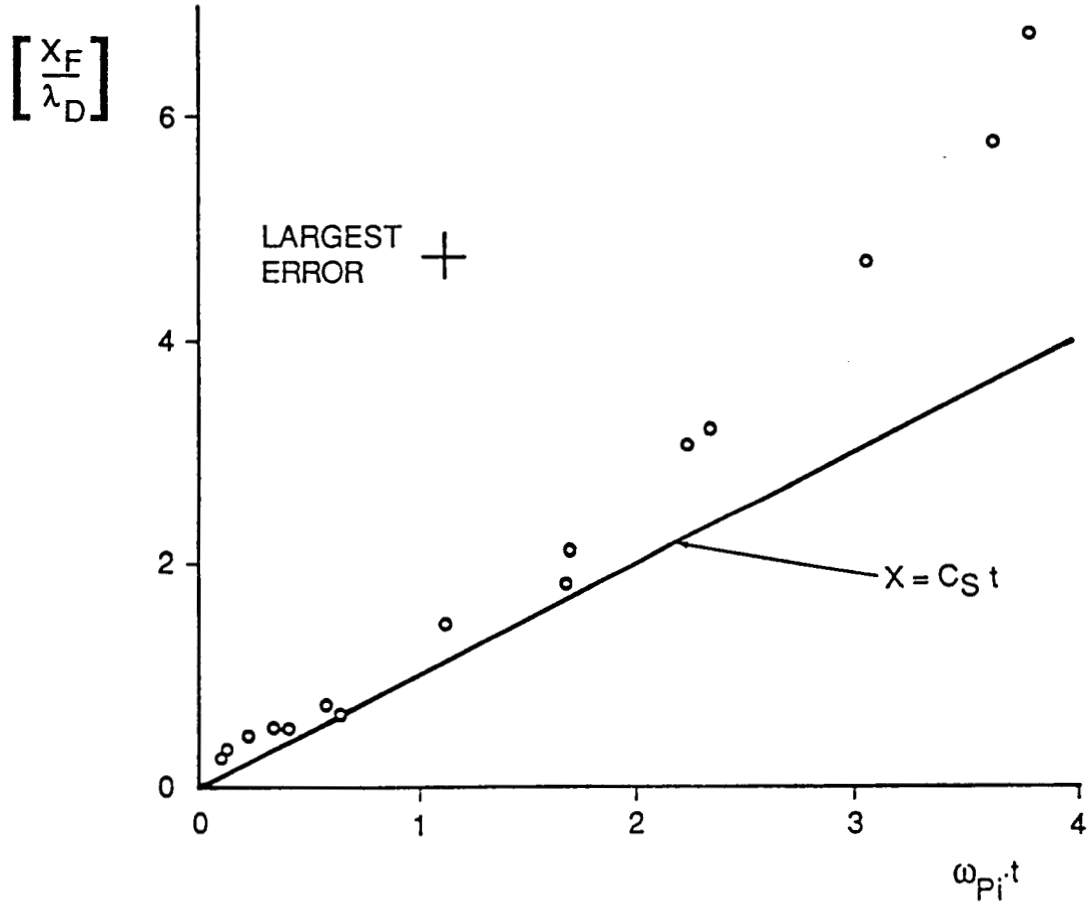

Figure 16. Variation of the expansion front position (X_F), normalized by Debye length, with time, normalized by the ion plasma frequency. The density used in the Debye length and ion plasma frequency is obtained from the ambient plasma at the plate location. The straight line indicates expansion at the ion acoustic speed. The figure is modified from *Wright et al.* [1985].

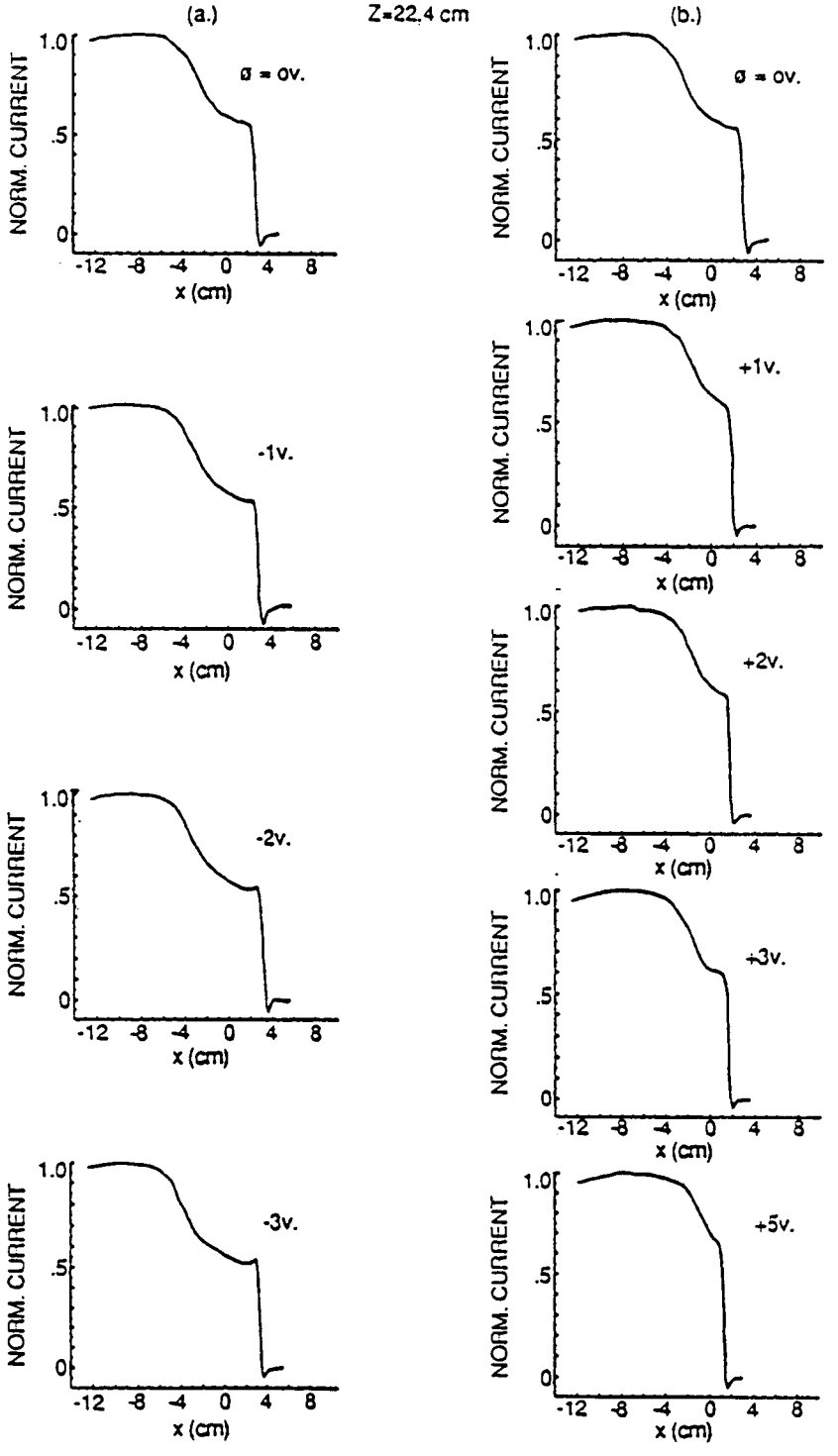

Figure 17. Variation of the normalized ion current density with transverse position at a downstream distance of $z = 22.4$ cm: (a) negative plate bias; (b) positive plate bias.

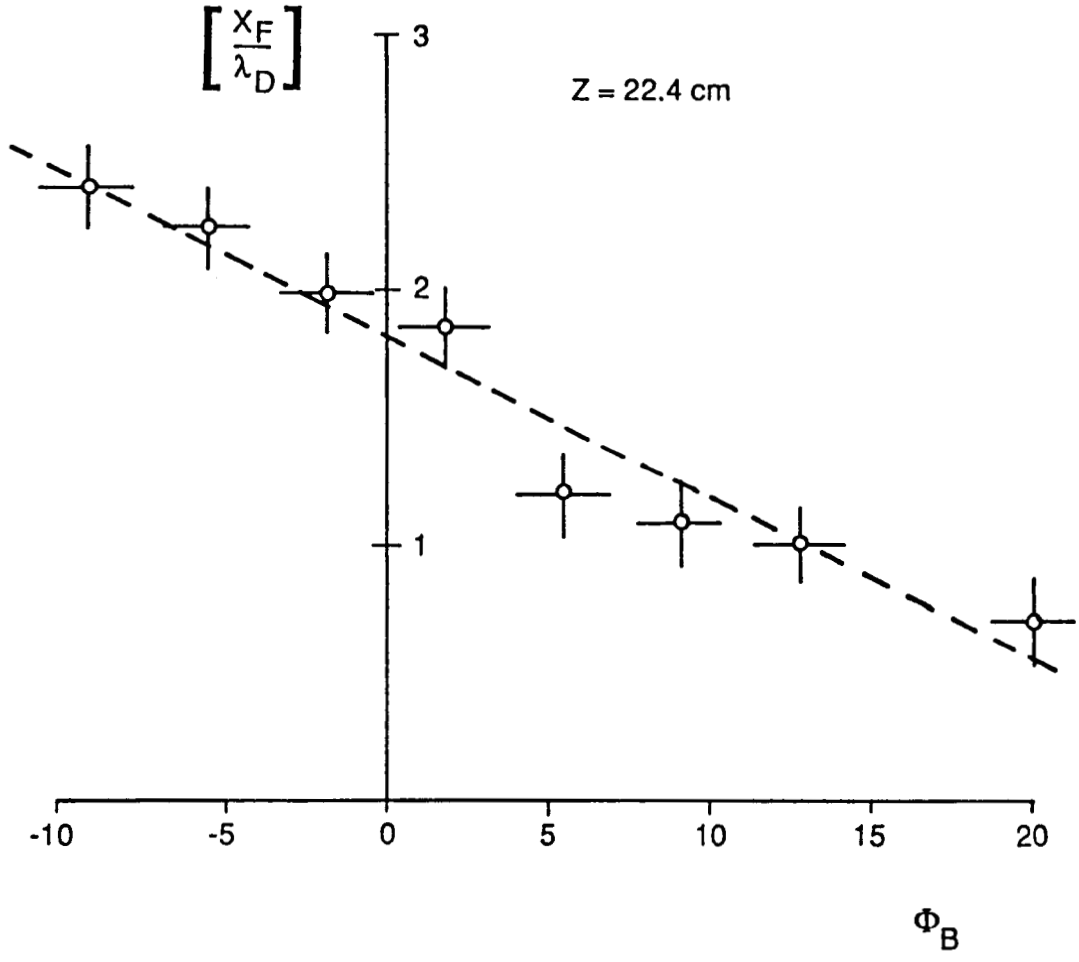

Figure 18. Variation of the expansion front position (X_F), normalized by Debye length, with normalized plate potential $\Phi_B(\equiv e(\phi_{plate} - \phi_{sp})/kT_e)$ at a downstream distance of $z = 22.4\,\mathrm{cm}$.

focussing, which can occur in either case.

Expansion front velocities, normalized by C_S given Table 1, versus $\omega_{pi}t$ for several laboratory experiments and numerical simulations are presented in Figure 19. The value for ω_{pi} was calculated in the same manner as was done for Figures 14 and 16. The present experimental data were derived from the x component of velocity measured by the DIFP at the positions of the expansion front (see Figure 15). These values are in good agreement with results obtained by calculating the derivative of the data shown in Figure 16. Results from the other experiments shown in Figure 19 were obtained by finding the rate of change of the expansion front with time. The numerical simulation curves are the calculated ion velocities at the expansion front for initial conditions that are pertinent to the experiments; namely, a planar expansion from a very steep gradient a time $t = 0$.

The early time plasma expansion is very sensitive to the initial conditions. Discrepancies in the values from numerical simulations can be traced to the particular scheme for treating the large electric fields existing at $t = 0$. In the experiments of *Eselevich and Fainshtein* [1980] and *Alikhanov et al.* [1971], the bodies were at floating potential, whose value was not stated. If the body potential was more positive relative to the space potential than in the present experiment, then the initial conditions for expansion may vary from those of the present experiment and the numerical simulations resulting in the lower ion velocities shown in Figure 19. The temperature ratio in *Eselevich and Fainshtein* [1980], $T_e/T_i \simeq 2 - 4$, would contribute to a larger ion acoustic speed and hence, a lower value for the V_F/C_S ratio; and also, a non-zero T_i will modify the electric potential established during the expansion for the same time period as compared with the $T_i = 0$ case. However, the point to be emphasized from Figure 17 is not the discrepancies, but the agreement of the data on fundamental points. Each experiment and numerical simulation shows that the ion velocity should monotonically increase with time and

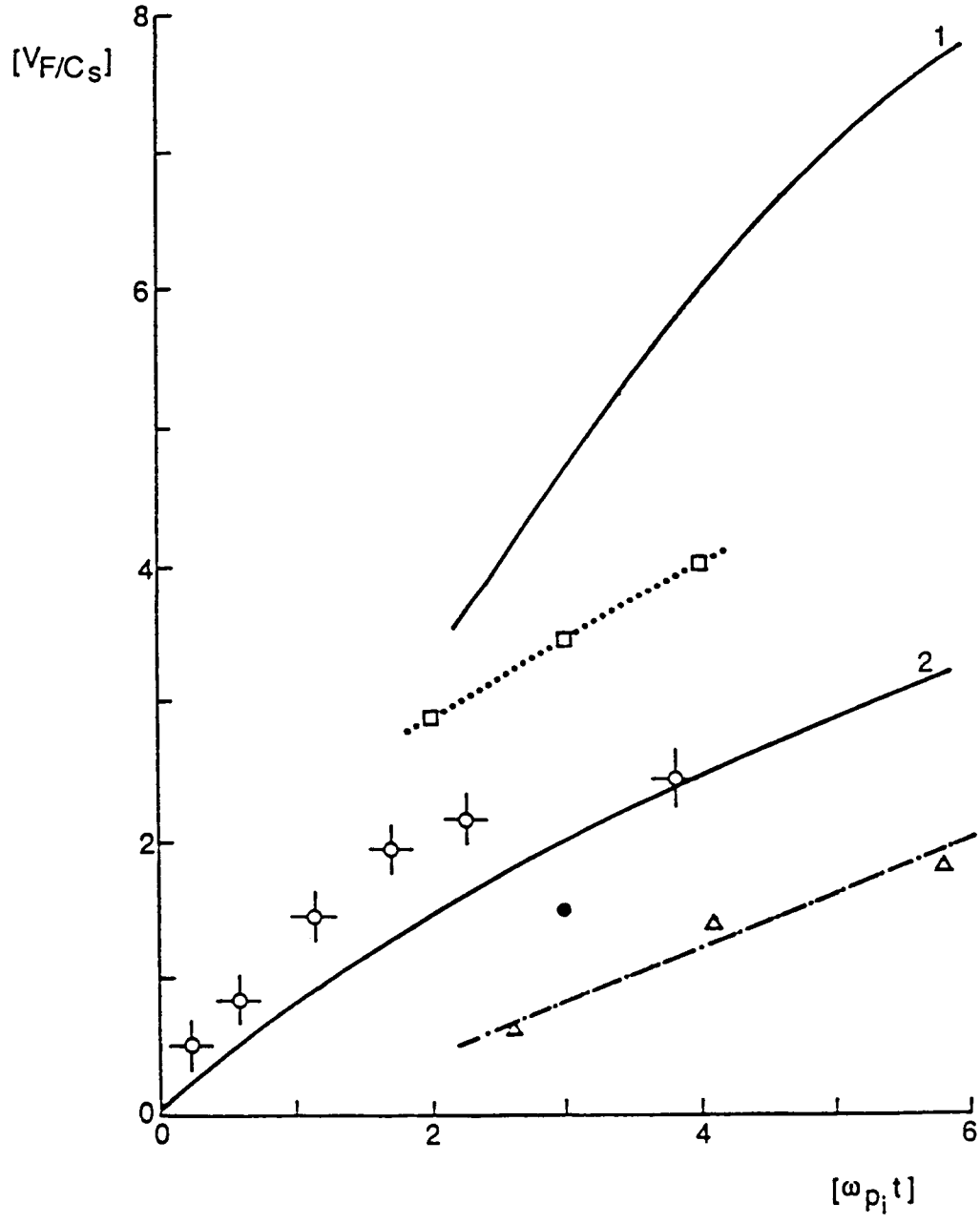

Figure 19. Variation of the ion velocity at the expansion front (V_F), normalized by the ion acoustic speed, with normalized time, $\omega_{pi}t$. Laboratory experiments: o this paper; ◻ *Chan et al.* [1984]; △ *Eselevich and Fainshtein* [1980]; • *Alikhanov et al.* [1971]. Numerical simulations: curve 1, *Gurevich and Meshcherkin* [1981*a*]; curve 2, *Crow et al.* [1975]. The figure is modified from *Wright et al.* [1985].

attain values greater than the ion acoustic speed.

At the farthest z positions an increase in the width of the expansion front is observed (see Figure 11). This may be connected with the apparent slowing down of the front as shown by the transverse velocity at the largest $\omega_{pi}t$ value in Figure 19. As discussed earlier, the decreasing ambient density should affect the electron pressure gradient which maintains the electric field that accelerates the ions. Similar spreading of the front width was observed by *Eselevich and Fainshtein* [1980] in a similar plasma chamber.

The self-similar, quasi-neutral solution for the velocity is shown in Figure 2*c*. Figure 20 shows the experimental data in terms of the self-similar variable $x/(C_S t)$. The ordinate value is the x component of the measured ion velocity normalized by C_S given Table 1. Results for four downstream locations, or times in the expansion, are shown. The solid line on the graph is (2.3); i.e., $V_i/C_S = (x/C_S t) + 1$. This line represents the asymptotic state of the plasma expansion. For the early times, for which this experiment pertains, one should not expect the plasma to be in the asymptotic state and the experimental values lying below the line reflect this situation. (The freestream divergence and the fact that all particles in the expansion region did not originate from a common density may also contribute to the points lying below the line.) However, at farther downstream locations, or later in time, the data are approaching the line at the higher $x/(C_S t)$ values. The plasma, therefore, approaches the asymptotic self-similar state in a few ion plasma periods, which is consistent with the time scales given in the numerical and experimental work noted in Figure 19.

Approximate analytical expressions were derived by *Katz et al.* [1985] which describe the numerical simulation results of *Crow et al.* [1975] to an accuracy of about 10 percent at the longer times and of about 15 percent at the earlier times. Recall that in *Crow et al.* [1975] the planar expansion of a semi-infinite plasma into

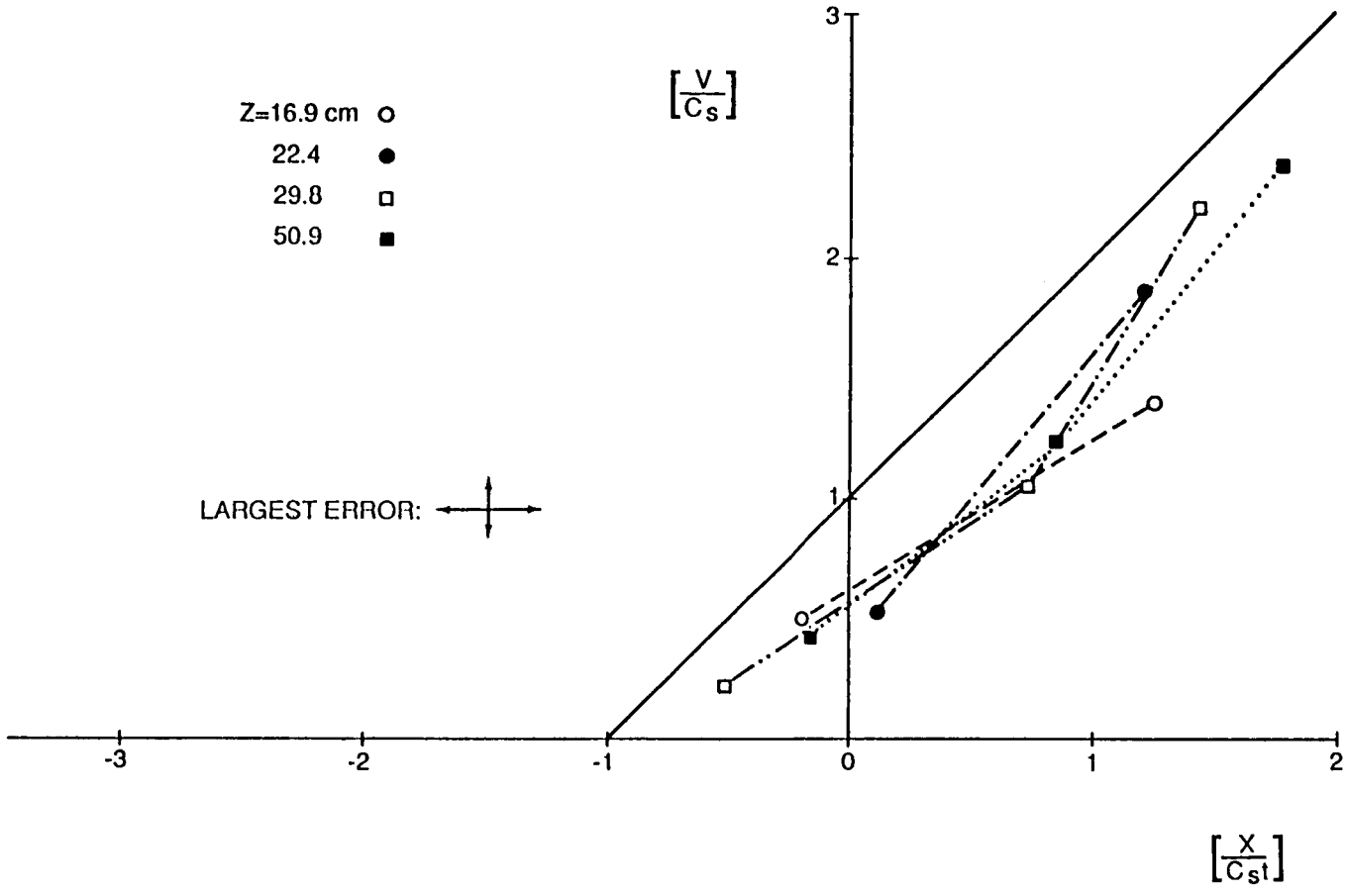

Figure 20. Variation of the transverse ion velocity, normalized by the ion acoustic speed, with the self-similar variable $x/(C_S t)$ for several z positions. The theory is represented by the straight line: $V/C_S = (x/C_S t) + 1$. The figure is after *Wright et al.* [1985].

a vacuum was solved in a self-consistent manner (including Poisson's equation). The ion fluid equations were used and T_i was assumed to be zero. The model of the *Crow et al.* [1975] results for the normalized front velocity and position as functions of $\omega_{pi}t$ are [*Katz et al.*, 1985]:

$$\frac{V_F}{C_S} = 2\left\{\ln(1+\nu\omega_{pi}t) - \left(1-\frac{0.43}{\nu}\right)\frac{\nu\omega_{pi}t}{1+\nu\omega_{pi}t}\right\}, \tag{3.3}$$

$$\frac{X_F}{\lambda_D} = 2\left\{\left(\omega_{pi}t+\frac{1}{\nu}\right)\ln(1+\nu\omega_{pi}t) - \omega_{pi}t - \left(1-\frac{0.43}{\nu}\right)\left(\omega_{pi}t-\frac{1}{\nu}\ln(1+\nu\omega_{pi}t)\right)\right\}. \tag{3.4}$$

The logarithm term in (3.3) exhibits the well known asymptotic behavior of the ion velocity at the expansion front [see (2.6)]. Note that $X_F \equiv \int V_F\, dt$ and the free parameter ν is determined from a fit to the *Crow et al.* [1975] numerical results to be about 1.6. The coefficient of the second term in (3.3) contains a numerical factor (0.43) that is proportional to the value of the electric field at $t = 0$, following *Crow et al.* [1975]:

$$\frac{Z_i e E}{M_i} = \frac{2C_S\,\omega_{pi}}{(2e)^{\frac{1}{2}}}, \tag{3.5}$$

where e is the base of the natural logarithm ($1/\sqrt{2e} = 0.43$).

Figure 21 shows the present experimental data compared with the above expressions. Figure 21*a* contains the data from Figure 19 and the solid line representing (3.3). Figure 21*b* contains the data from Figure 16 and the solid line representing (3.4). The measurements are quantitatively higher than the expressions, but display the same behavior with time. For the front velocity, the difference between the data and (3.3) appears to be a constant value. In *Wright et al.* [1986], this value was suggested to be an initial transverse velocity at the plate edge due to thermal motion. In the previous section (III.B), however, it was argued that the most important thermal motion, due to $[T_{i_\perp}]_{eff}$, was negligible. $[T_{i_\parallel}]_{eff}$ was noted

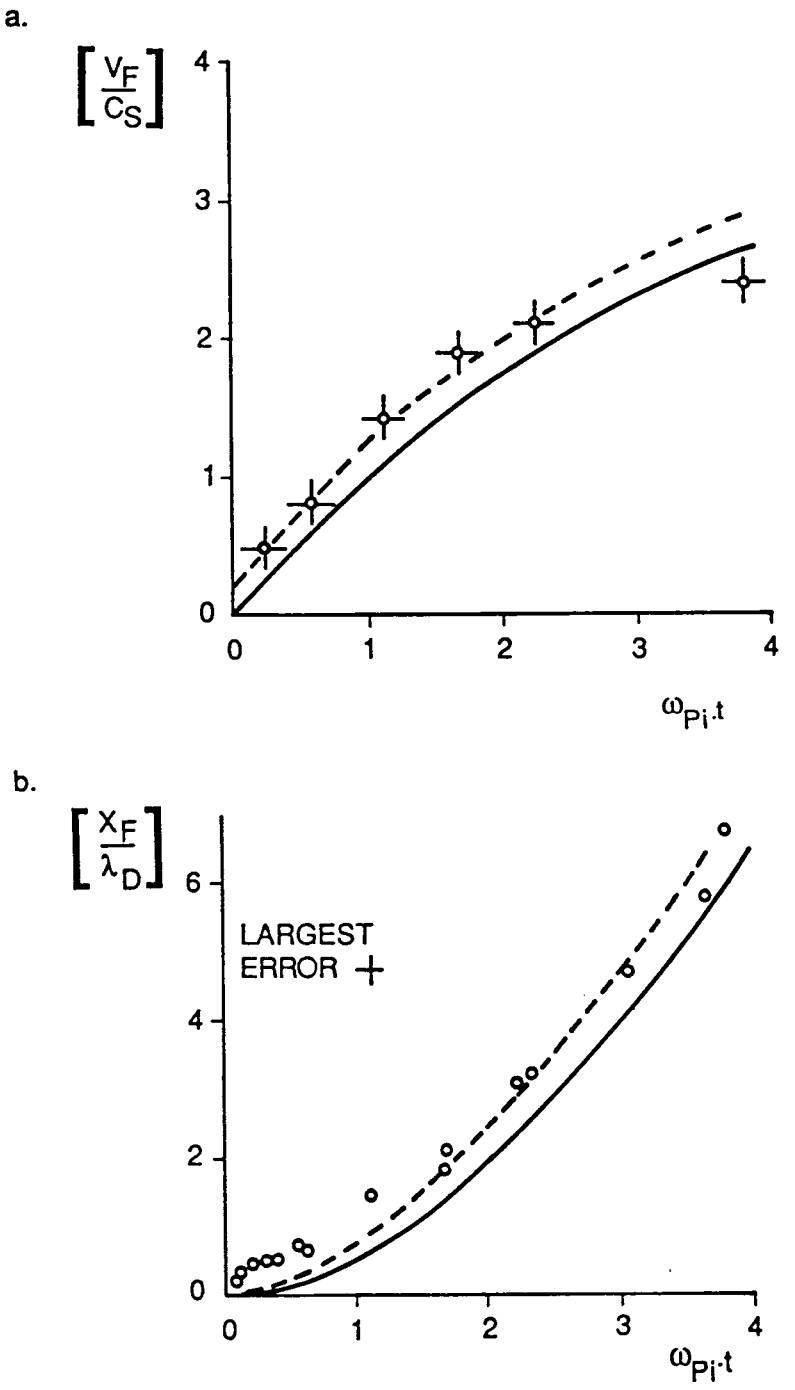

Figure 21. The normalized time dependence of: (*a*) the expansion front velocity normalized by the ion acoustic speed – o experiment, solid line (3.3), dashed line (3.6); (*b*) the expansion front position normalized by ambient Debye length – o experiment, solid line (3.4), dashed line (3.7). The figure is modified from *Wright et al.* [1986].

to be $\simeq 0.033\,\mathrm{eV}$. The velocity offset probably represents some kind of combination of ion thermal motion and sheath effects at the plate and upstream of the plate. Adding a constant value $V'/C_S = 0.25$ to (3.3) gives

$$\frac{V_F}{C_S} = \frac{V'}{C_S} + 2\left\{\ln(1+\nu\omega_{pi}t) - \left(1 - \frac{0.43}{\nu}\right)\frac{\nu\omega_{pi}t}{1+\nu\omega_{pi}t}\right\}, \tag{3.6}$$

and is represented by the dashed line in Figure 21*a*. Integrating (3.6) yields the equation

$$\begin{aligned}\frac{X_F}{\lambda_D} = (V'/C_S)\omega_{pi}t + 2\Bigg\{&\left(\omega_{pi}t + \frac{1}{\nu}\right)\ln(1+\nu\omega_{pi}t) - \omega_{pi}t \\ &- \left(1 - \frac{0.43}{\nu}\right)\left(\omega_{pi}t - \frac{1}{\nu}\ln(1+\nu\omega_{pi}t)\right)\Bigg\},\end{aligned} \tag{3.7}$$

which is shown as the dashed line in Figure 21*b*. The data, obtained from two independent instruments, shows good quantitative agreement with (3.6) and (3.7).

The experimental situation should be described by the collisionless kinetic equations while the model equations were derived from the fluid approach. As noted in Appendix A, the fluid approach should be valid at large $\xi = (x/C_S t)$, which is not the case here. However, the long range nature of the electrostatic forces and the experimentally imposed fact of no crossing ion streams in the wake would allow the expansion front to retain the character of a fluid-like element such that the above model equations apply. These equations may be used to predict, at even longer times, the results of other experimental situations where plasma expansion may be realized.

D. Summary of the results

The plasma expansion into the wake of a large rectangular plate immersed in a single ion, collisionless, streaming plasma is examined. Several characteristics of the process involved in 'plasma expansion into vacuum' that have been predicted

theoretically were observed, including (1) the creation and propagation of a rarefaction wave disturbance; (2) the creation and motion of an expansion front; and (3) the acceleration of ions into the wake at speeds above the ion acoustic speed. The expansion was limited to early times (i.e., a few ion plasma periods) by the combination of plasma density, plasma drift speed, and vacuum chamber size. This prevents any agreement with the self-similar theory, but results are in good agreement with numerical simulations and other laboratory experiments for the early time expansion. In particular, good quantitative agreement is found between approximate analytical expressions [*Katz et al.*, 1985], based on the results of the numerical simulation by *Crow et al.* [1975], and the data for the expansion front velocity and position. The conclusion is that the plasma expansion process is the dominant wake filling mechanism in the near wake of a large body, whose potential is approximately the plasma space potential.

CHAPTER IV. BINARY ION PLASMA WAKE EXPERIMENT

When a body moves through a planetary plasma environment, it usually encounters two or more ionic constituents. For example, in the earth's ionosphere, oxygen and hydrogen exist, along with other minor constituents, with relative abundances which vary with altitude and latitude. At latitudes away from the polar regions, oxygen is the major ion at the lower altitudes and hydrogen is the major ion at the higher altitudes. The orbits of ionospheric spacecraft typically carry them through large changes in the oxygen-to-hydrogen density ratio. In examining in situ data from such spacecraft, *Samir and Kaufmann* [1980] concluded that the relative hydrogen concentration and the electron temperature have a much greater effect than other plasma properties and parameters in determining the ion distribution in the wake. In a comparison of a numerical wake model with these and other in situ wake measurements, *Samir and Fontheim* [1981] found orders of magnitude discrepancies for the maximum rarefaction zone; i.e., the region immediately behind the satellite. The wake model, from *Parker* [1976, 1977], solves the steady-state, Vlasov-Poisson equations for a single ion mass self-consistently. To remove the discrepancies, *Samir and Fontheim* [1981] suggested using a separate Vlasov equation for each ion mass. *Gurevich et al.* [1969], in treating such a case, showed that for regions near the satellite surface, the hydrogen density substantially exceeds the oxygen density even if the relative hydrogen concentration in the ambient is only a few percent. It is clear that for the practical case of an ionospheric satellite, or for plasma-body interactions in general, an understanding of the particle behavior in the wake region will require knowledge about its parametric dependence on the ion

species density ratio and the ion mass ratio (or the $\gamma = Z_2 M_1 / Z_1 M_2$ parameter of Chapter II) in addition to the other parameters governing the interaction, outlined in Chapter I.

To date, no laboratory experiment has addressed the wake of a body in a supersonic, binary ion plasma in a parametric fashion. In *Raychaudhuri et al.* [1986], a small amount of helium was introduced to the source of a flowing argon plasma and measurements were performed in the wake of a plate. The value for γ in this case is 10. (Recall that in the definition for γ the subscript '1' refers to the major ion species.) Two groups of accelerated ions were found whose velocity ratio depended on the square root of the mass ratio between the two species. This indicates that the helium ions were accelerated by the potential difference between argon and electron space charge distributions formed in the wake filling process, in accord with the *Gurevich et al.* [1973*a*] plasma expansion theory. However, in the laboratory, the experiment is conducted in the reference frame of the body; and to simulate the interaction properly, both ion species need to be moving at the same velocity. This necessitates the independent generation of each ion species for the plasma stream.

A source is described below that can produce a supersonic plasma stream consisting of two ion components, having a common flow velocity, with a controllable ion density ratio. Results are reported from three wake experiments using such plasma streams, in which the ion density ratio is varied more than an order of magnitude, while variations in the other plasma conditions are less than a factor of 1.5. This class of experiments is an extension of the single ion plasma-plate experiment that employs the same experimental configuration. The equivalent 'expansion time' of the experiment is still small, again limited by plasma density, flow velocity, and chamber length. The measured ion behavior is discussed in terms of the plasma expansion theory presented in Chapter II.

A. Binary ion plasma source

For ions with different masses to move at the same velocity, they must be accelerated to different energies. This drift energy ratio is given by the mass ratio; i.e.,

$$\frac{E_1}{E_2} = \frac{M_1}{M_2}. \tag{4.1}$$

If a mixture of two different gases is introduced into a source, like that shown in Figure 8*a*, the ions subsequently produced will have the same drift energy, given approximately by the anode potential. Therefore, to obtain a common flow velocity for two ion species, two independently operated sources must be used to create ions moving with different drift energies as given by (4.1). The two ion streams must then be merged to form a single plasma stream that can be utilized for for experiments.

Figure 22 shows a schematic of the source used to produce a binary ion plasma. The appendage containing the single ion plasma source, used in the experiment described in the preceeding chapter (see Figure 8*b*), was modified to accomodate the new source. The boxes labeled #1 and #2 represent the two independent ion sources, which are mounted at right angles to each other. The axis of source #1 is aligned with the vacuum chamber axis. Each source is constructed in much the same manner as the typical electron bombardment source shown in Figure 8*a*. Each of the grids in the ion optics section is a stainless steel plate with a 52-hole pattern with an overall diameter of 4 inches. Emissive tungsten wires are also placed at the exit of each source to achieve plasma beam neutralization. The heavier mass ion is produced by source #1, while the lighter mass ion is produced by source #2. A conducting ring, designated by ϕ_{R_2}, is placed near the exit of source #2 and is biased at a positive voltage to help keep the light ion plasma beam from spreading

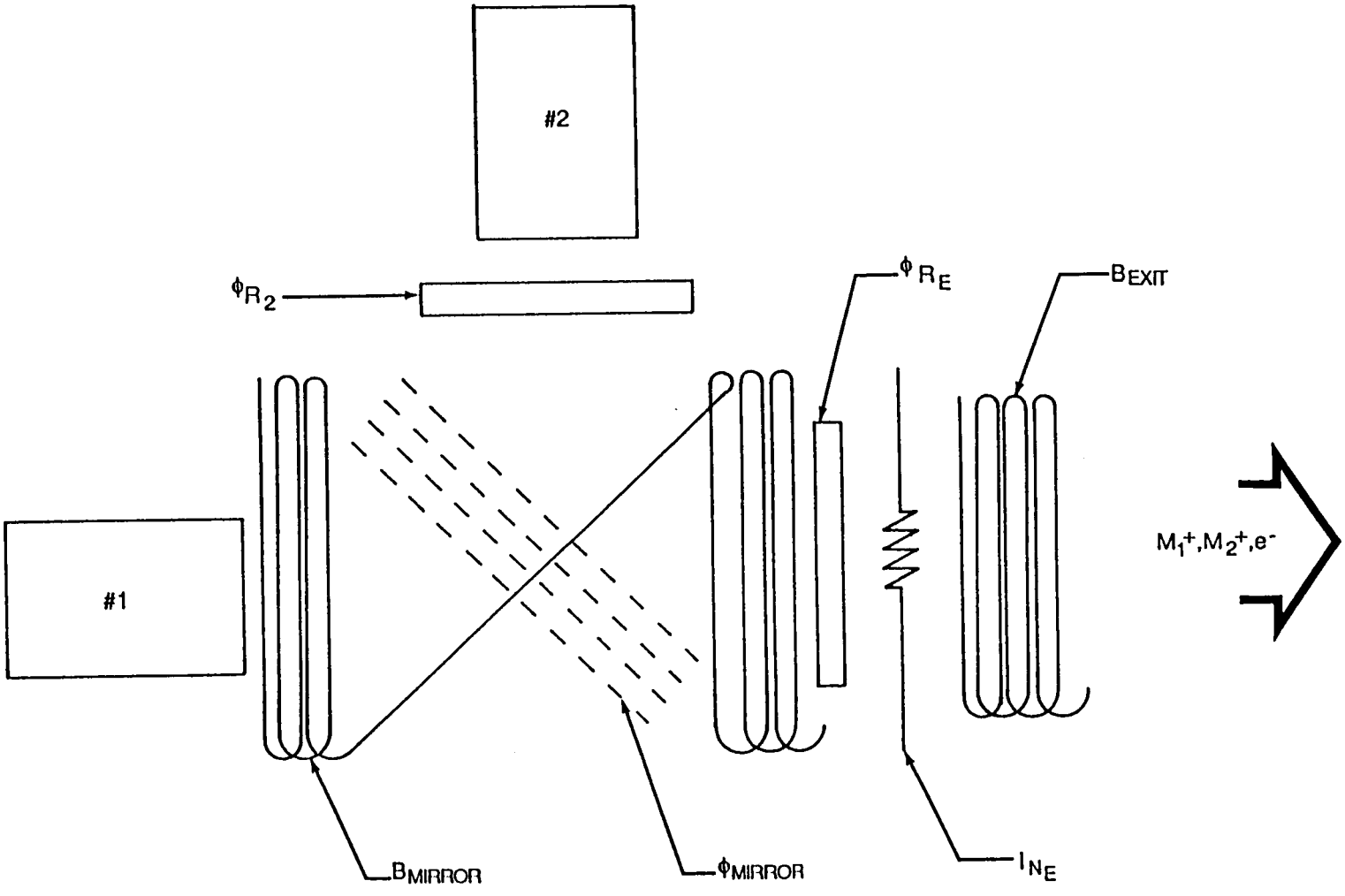

Figure 22. Schematic of binary ion plasma source.

apart. The ion sources can be controlled to produce the desired output ion current density for each ion species.

Each plasma stream subsequently enters the region containing an electrostatic mirror structure. This structure consists of four parallel grids electrically isolated from each other and mounted in an insulating frame. The outer surface of the insulator is covered with a thin aluminum strip and attached to chamber ground. The grid system is mounted such that the normal to the grids is 45° to the chamber axis. Each grid of the mirror consists of a series of parallel wires (1 mm. dia.) in one direction, not a cross-hatched mesh, in order to improve the total transparency of the mirror system. The outer two grids in the mirror are maintained at ground potential while the inner two grids are biased at a voltage of the same magnitude, but opposite in polarity (ϕ_{MIRROR}). The positive grid of the inner two grids is closest to source #2. The applied biased voltage is high enough such that the entire energy spread of the mass 2 ion (M_2^+) is redirected along the chamber axis. The ions from source #1, M_1^+, possess a much higher drift energy and are not significantly affected by ϕ_{MIRROR}. However, the electrons in the plasma stream from source #1 do not pass through the mirror system, while the electrons in the plasma stream from source #2 are redirected with the M_2^+ ions. An additional emissive tungsten wire (I_{N_E}) is introduced in the plasma downstream from the electrostatic mirror to provide more electrons for beam neutralization. Also, another biased, conducting ring (ϕ_{R_E}) is added between the mirror and the exit neutralizer. The post mirror region thus contains a plasma consisting of electrons and two ion species moving at a common stream velocity.

Two coils of wire are wrapped around the vacuum chamber to allow for the addition of magnetic fields (B_{MIRROR} and B_{EXIT}) in the particular regions indicated. These fields served to keep the plasma from spreading and confine it closer to the chamber axis, but are not high enough to confine plasma in the electrostatic

mirror region. It is observed that changes in the B_{MIRROR} and B_{EXIT} fields provide an additional way to adjust the ion density ratio in the plasma stream, particularly in regard to the Ne^+ component.

The highest ion current density values in the middle region of the chamber are attained for a particular alignment of all the magnetic fields in the source. Recall from the discussion in Chapter III, describing the operation of an electron bombardment-type plasma source, that magnetic fields will be present in each ion source. The orientation of the fields from the sources are such that they pointed towards the electrostatic mirror. Best results are obtained with B_{MIRROR} and B_{EXIT} aligned but anti-parallel to the plasma flow direction. The resulting cusp-type field in the mirror region introduces some extra effects into the plasma beam, as is pointed out below.

B. Binary ion plasma free-stream characteristics

The free-stream measurements as well as the experiments have been conducted using a mixture of neon (at. wt. = 20.2) and krypton (at. wt. = 83.8). The use of inert gases eliminates any chance of additional ions being created by the disassociation of a molecular gas such as nitrogen (although nitrogen was used in the single ion plasma experiment, no traces of an additional ion were found). The mass ratio of the two gases, $M(Kr^+)/M(Ne^+)$ is 4.15. As mentioned in the discussion of plasma expansion in Chapter II, the larger the mass difference the greater the change in the density distribution in the expansion region; i.e., the effects scale with γ ($= Z_2M_1/Z_1M_2$). A helium-argon mixture was attempted initially, but the helium current density was too low to provide measurable variation. The neon-krypton mixture represents an increase by one row in the Group VIII column of the Periodic Table of the Elements. The heaviest gas in Group VIII that is availiable

for practical use in experiments is xenon, but it is quite expensive. The $Ne^+ - Kr^+$ plasma used in the present experiment provides a starting point for future experiments where the parametric dependence of γ will be investigated.

A particular ion component density ratio, $n(Ne^+)/n(Kr^+)$, is established by first obtaining a desired current from one of the ion sources. The cathode current or the anode voltage for this source is lowered and then power is supplied to the second ion source. After the desired output of the second source is set, full power is restored to the first source. The measured current density is the sum of the outputs of the two sources. This implies that there is no interaction of the streams in the electrostatic mirror region, or at least very little as determined by a probe measurement at the closest approach of 60 cm from the exit neutralizer.

The configuration of the measurement region is the same as diagrammed in Figure 8*b*. That is, the (x, z) plane defines the mapping plane for the probe movement. The characteristics and operation of the probes are described in Chapter III and in Appendix C. The procedures used in the single ion plasma experiment for obtaining measurements are again followed, except that a MASSCOMP 560 computer is used for acquisition and storage of the Langmuir probe and DIFP data. Since the plasma contains two ion species, the operation of the DIFP has to be performed twice in order to diagnose each ion. This operational sequence is described in Appendix C.3.b.

The plasma stream has been measured to have the following nominal properties for both the free-stream and the experiment and are presented in Table 2. The value of n_{tot} is given for a location at ≈ 70 cm from the source. The neutral gas pressure in the chamber during source operation was $6 - 7 \times 10^{-6}$ Torr. Base pressure was $2 - 3 \times 10^{-7}$ Torr.

Table 2. Properties for binary ion plasma stream.

$E_d(Ne^+)$ eV	$20-25$
$E_d(Kr^+)$ eV	$85-95$
$n_{tot}(\mathrm{cm}^{-3})$	$0.8-1.1\times10^5$
$n(Ne^+)/n(Kr^+)$	variable
$T_e(\mathrm{eV})$	$0.25-0.35$
$\phi_{sp}(\mathrm{volts})$	$+(2-3)$
$[T_{i_\perp}]_{eff}$	$<0.3T_e$

The perpendicular component of the ion beam temperature in the binary ion plasma was not directly measured. As mentioned in Appendix C.3.b, information from the width of the DIFP deflection mode profiles could not be translated into a perpendicular beam temperature value. However, an estimate of the effective perpendicular ion temperature can be obtained from (3.2). With the above ion energies at a position of 70 cm from the source and with a source radius of 2 in. (see Section IV.A), the effective perpendicular temperature components are: $[T_{i_\perp}(Ne^+)]_{eff}\simeq 0.017\,\mathrm{eV}$ and $[T_{i_\perp}(Kr^+)]_{eff}\simeq 0.069\,\mathrm{eV}$. Since the Ne^+ ions must make a 90° turn in the source as a result of the electrostatic mirror voltages, a better temperature estimate for Ne^+ would be obtained by using the effective radius of the mirror (= 3.5 in). The result is $[T_{i_\perp}(Ne^+)]_{eff}\simeq 0.051\,\mathrm{eV}$. In either case, the estimate from (3.2) indicates that more than two orders of magnitude difference exists between this and the $[T_{i_\perp}]_{eff}\simeq 1\times10^{-4}\,\mathrm{eV}$ estimated for the single ion plasma. Also note that the transverse motion implied by $[T_{i_\perp}]_{eff}$ is not expected to be Maxwellian.

Typical parallel beam temperatures are indicated in Appendix C.3.b. These values are $[T_{i_\parallel}(Ne^+)]_{eff}\simeq 0.3\,\mathrm{eV}$ and $[T_{i_\parallel}(Kr^+)]_{eff}\simeq 0.1\,\mathrm{eV}$. Both $[T_{i_\parallel}]_{eff}$

values are observed to vary with spatial position. The largest variation occurrs for $[T_{i_\parallel}(Ne^+)]_{eff}$ which changes by factors of $2-3$, the highest values existing in the outer edges of the beam. The variation in $[T_{i_\parallel}(Kr^+)]_{eff}$ is less than a factor of two. These variations represent the evolution of the space charge in the beam as it flows through the chamber. Recall that $[T_{i_\parallel}]_{eff}$ for the single ion case is $\simeq 0.03\,\mathrm{eV}$. Most of the difference in the $[T_{i_\parallel}]_{eff}$ values between the two cases can be attributed to the difference in the ionization of an inert gas and a diatomic gas in the source. Extra vibrational and rotational degrees of freedom are availiable for energy absorption when an ionizing electron hits a diatomic molecule. In summary, the T_e/T_i ratio is substantially larger for the binary ion plasma stream.

The flow velocity for the binary ion plasma stream is greater than the stream velocity in the single ion case. The Mach number range is $\mathcal{M} = 14-20$. The ion acoustic speed in a two ion component plasma is defined by [e.g., *Sharma et al.*, 1986]:

$$C_S = \left(\frac{\beta k T_e}{M_H}\right)^{\frac{1}{2}}, \tag{4.2}$$

where $\beta = (1-\alpha)Z_H + \alpha\mu Z_L$, $\mu = M_H/M_L$, and $\alpha = Z_L n_L/n_0$. The subscript 'H' designates the heavy ion mass while subscript 'L' designates the light ion mass; i.e., $M_H = M(Kr^+)$, $M_L = M(Ne^+)$. The quantity α represents the light ion percentage in the plasma. In comparing (4.2) with the acoustic speed in a single ion plasma, an 'effective' mass of the plasma is noted; i.e., $M_{eff} = M_H/\beta$ or $1/M_{eff} = (1-\alpha)/M_H + \alpha/M_L$.

The ambient total plasma density in the binary ion plasma case is only slightly less than in the single ion plasma case, while the range of values for the electron temperature includes the values in the single ion plasma case. The space potential in the binary ion case is a few volts more positive.

The following two sections present data that illustrate the general ion behavior in the free-stream obtained for two different orientations of the plasma source. In

Case A, the plasma source is attached to the vacuum chamber such that the plane containing the axes of the Ne^+ and Kr^+ sources is parallel to the x, z plane. In Case B, the plane containing the sources' axes is oriented perpendicular to the x, z plane.

1. Free-stream Case A. Figure 23 presents Faraday cup measurements in a plasma where the ion component density ratio is given by $n(Ne^+)/n(Kr^+) < 0.5$. The normalized total ion current density (I/I_0) is plotted versus the transverse position (x) for several downstream positions (z). The vertical arrows in the figure connect a particular current profile with its zero current level. The $x = 0$ point marks the location of the chamber axis. The downstream distances are referenced to the exit neutralizer (I_{N_E} in Figure 22). This is the last point in the source where the plasma is affected by an external control. The gradients in the current profiles are larger than in the single ion plasma case. For the downstream position at $z \simeq 60$ cm, the width of the profile at the $0.5I_0$ point is ≈ 15 cm. In the single ion plasma case, the corresponding width at about the same z position is greater than 30 cm (see Figure 9). The beam profile is observed to spread as it moves downstream and also develop an asymmetry about the chamber axis. The divergence of the $I/I_0 = 0.8$ and $I/I_0 = 0.5$ points are 6.2° and 5.8°, respectively. This accounts for the relative flattening of the current profile at the farthest downstream position.

The behavior of each ion component, as determined by the DIFP, is shown in Figure 24. The percentage current densities (I^+/I_0) of Kr^+ and Ne^+ are plotted versus transverse position for the same downstream locations indicated in Figure 23. The normalization factor for a given z position, is chosen to be the largest total sum of the individual currents in that particular transverse profile. The current density for each ion at the measurement location is determined in the manner described in Appendix C.3.b. The error associated with the percentage current density points is $\approx \pm(5 - 10)\%$ of the indicated values. Highest accuracy occurs for the higher

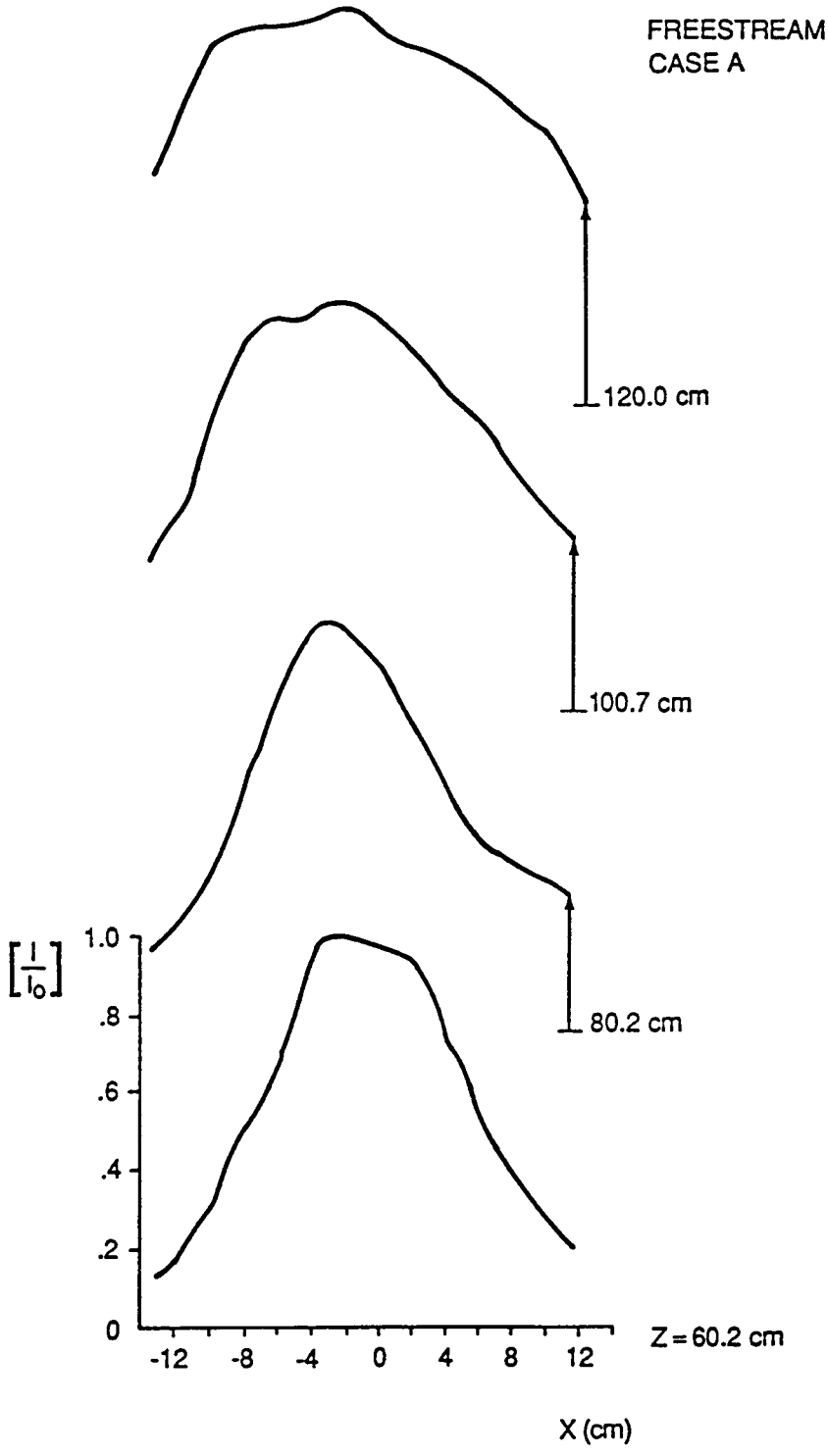

Figure 23. Variation of the normalized total ion current density with transverse position for several downstream locations from the plasma source. Free-stream Case A.

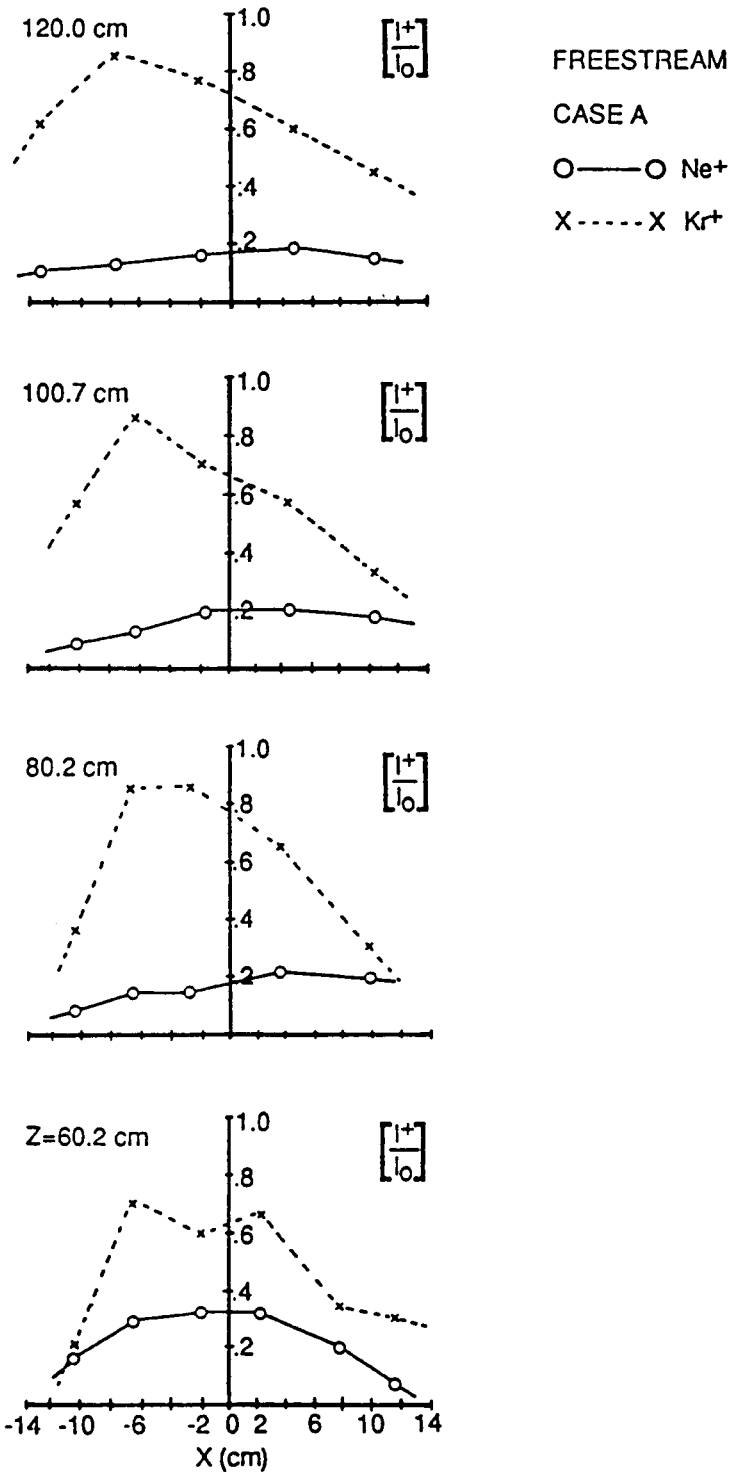

Figure 24. Variation of the normalized percentage ion component current densities with transverse position for the downstream locations of Figure 23. Free-stream Case A.

currents and for flows near the instrument normal. The error doubles for the lowest current measurements ($I^+/I_0 < 0.1$).

An estimate of the ion component density ratio, $n(Ne^+)/n(Kr^+)$, can be found from the ratio $[I(Ne^+)/I_0]/[I(Kr^+)/I_0]$. The density ratio is observed to vary with transverse position and also to decrease with increasing downstream distance. Part of the z variation is due to the evolution of the beam and part is due to a temporal change in the source. In general, it was found that the output of the Kr^+ source increased more over time than the output of the Ne^+ source. During the experiment, an effort was made to periodically check the ambient Kr^+ and Ne^+ characteristics and make minor adjustments in the plasma source to maintain relatively constant beam conditions. The assignment of a particular value for $n(Ne^+)/n(Kr^+)$ is thus seen to be approximate.

The vector flow for each ion component is presented in Figure 25. The measurement location is at the head of the arrows. The most obvious feature is the general non-alignment of the Ne^+ flow with the Kr^+ flow. This is a pervasive feature of this plasma beam for a wide range of $n(Ne^+)/n(Kr^+)$ ratios. There is some flow alignment for the smaller negative x values, which can be associated with the off-axis peak in the FC measurements shown in Figure 23. Both the general non-alignment of Ne^+ with Kr^+ and the divergence of the total beam current was also observed for zero B_{MIRROR} and B_{EXIT} fields. These magnetic fields served to concentrate the plasma closer to the chamber axis. It is believed that the divergence of Ne^+ relative to Kr^+ results from space charge effects in the beam in the region of the electrostatic mirror. For zero B_{MIRROR} and B_{EXIT} fields, the alignment of the flow vectors (and hence the off-axis peak in the FC current profiles) occurs at larger negative x values. This divergence of the bulk flow indicates that the normal to the grids in the electrostatic mirror may not be aligned at precisely 45° to the chamber axis.

C-2

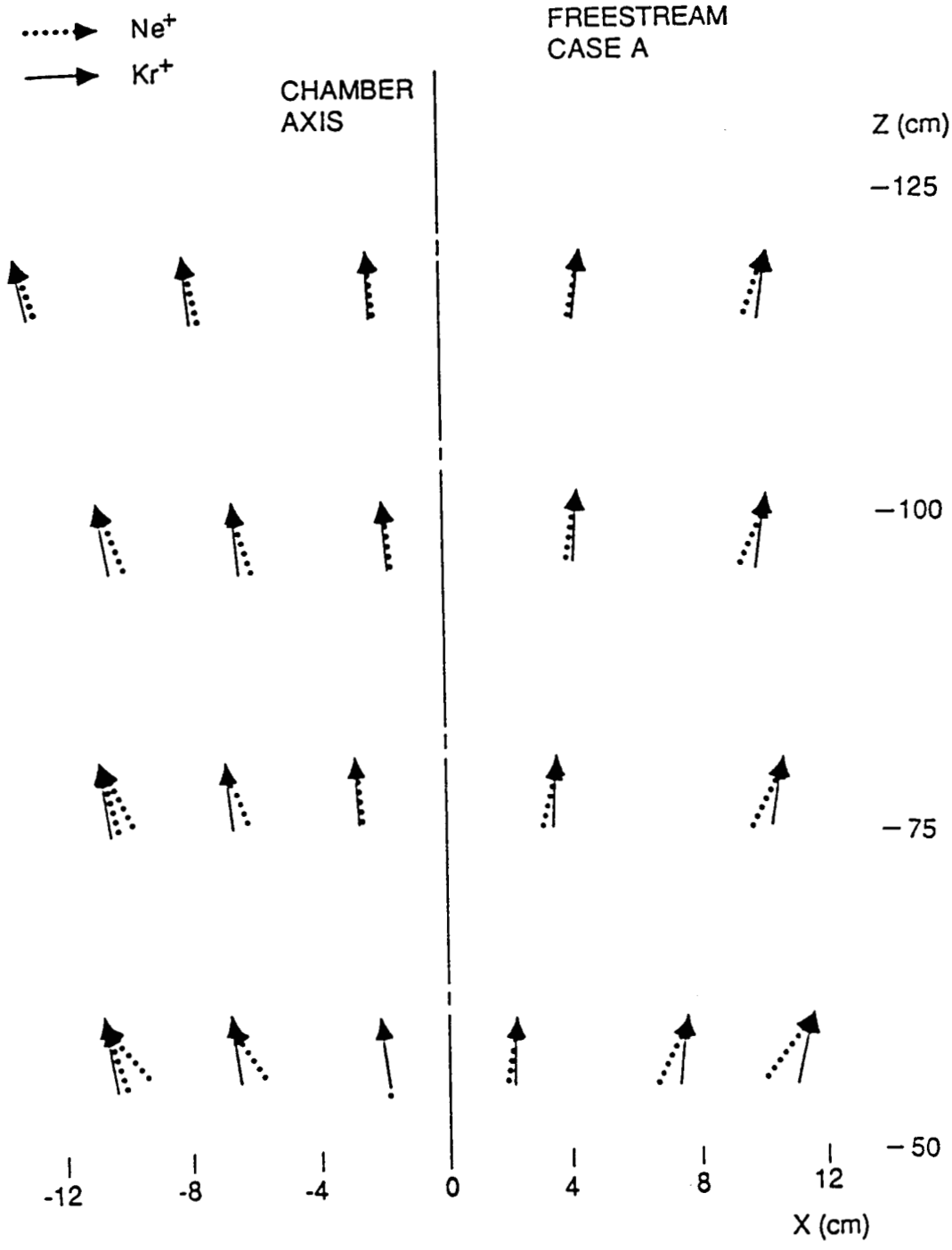

Figure 25. Velocity flow field for each ion constituent in free-stream Case A. Solid arrows represent Kr^+ while the dotted arrows represent Ne^+. The measurement location is at the tip of the vector. A vector with a dot at the base indicates that the Ne^+ and Kr^+ flow is co-aligned.

Another feature to point out is the occurrence of a second Ne^+ stream for the largest $|-x|$ positions at the $z = 60.2\,\text{cm}$ and $80.2\,\text{cm}$ locations. This observation implies the possibility of a shell on the outer edge of the plasma beam where an additional Ne^+ stream exists. The action of the complicated magnetic field geometry in the electrostatic mirror is the suspected cause of this effect. No additional Ne^+ stream was observed in the same measurement region for zero values of both B_{MIRROR} and B_{EXIT}. When two Ne^+ streams are detected at a particular point, the combined current of both Ne^+ streams is used to calculate the values for plots such as Figure 24.

The quantitative differences between the Ne^+ and Kr^+ flow vectors can be seen in Figure 26. The absolute value of the angle measured by the DIFP is plotted versus transverse position for the downstream positions. Note the difference in the y-axis scale between the Ne^+ and Kr^+ angle values. The vertex of the V-shaped profiles is the location at which the stream orientation changes from positive to negative. Again note the presence of two Ne^+ streams for the particular negative x positions. The envelope of the Kr^+ streams has a much smaller width than the envelope of the Ne^+ stream.

In summary for Case A, the orientation of the plasma source is such that the plane containing the Kr^+ and Ne^+ sources' axes is parallel with the x, z mapping plane. The total ion current density is observed to (1) peak off-axis, (2) develop an asymmetry about this peak, and (3) possess larger transverse current gradients than in the single ion experiment. The Ne^+ flow diverges relative to the Kr^+ flow over almost the entire measurement region. An additional Ne^+ stream is detected in the outer negative x region of the plasma beam for part of the beam volume. There is a tendancy for the Ne^+ and Kr^+ to move to opposite sides of the vacuum tank.

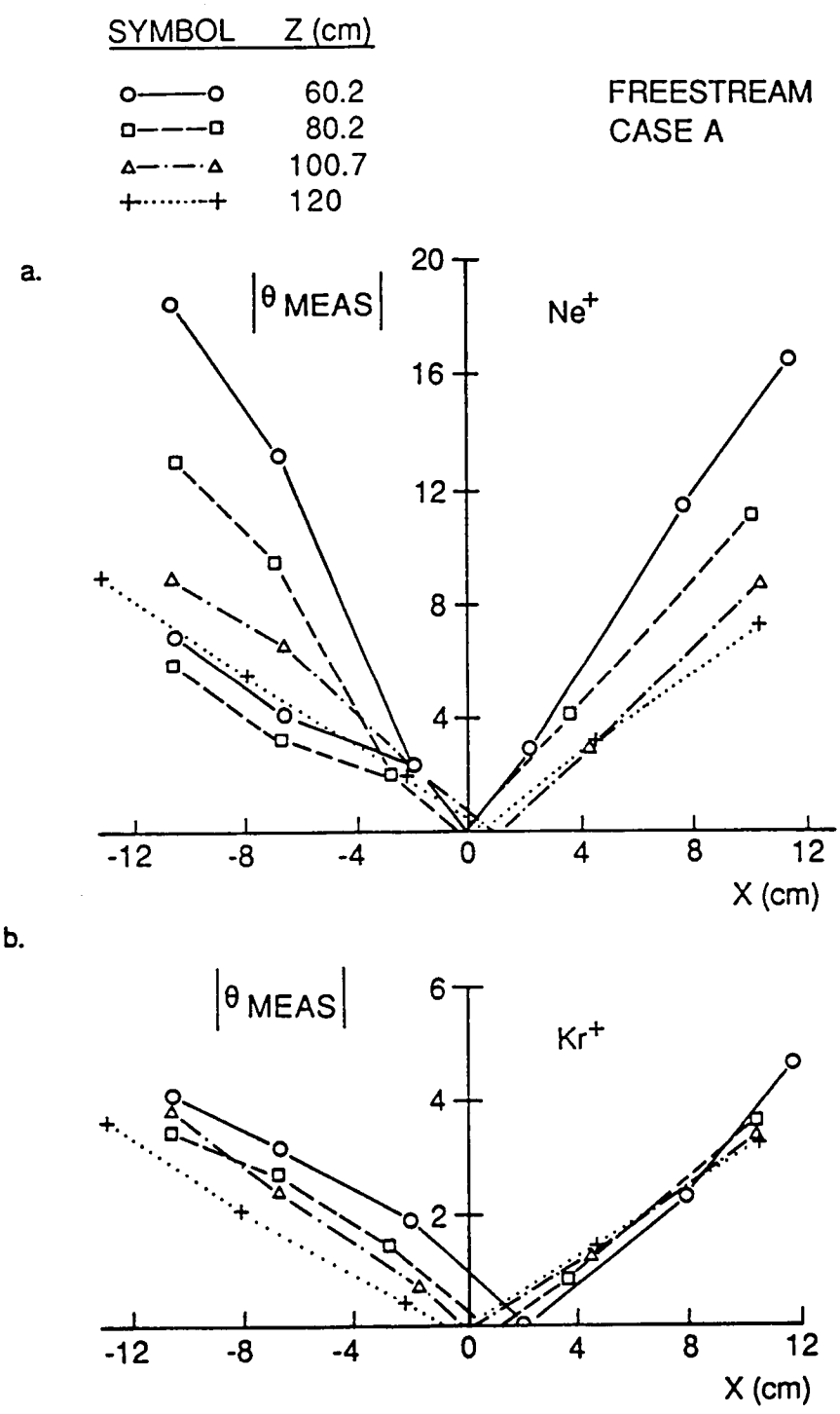

Figure 26. Variation of the measured ion flow angle magnitude with transverse position for the downstream locations in Figure 23 for free-stream Case A. (*a*) Ne^+. (*b*) Kr^+.

2. Free-stream Case B. For this case, the plasma source was rotated 90° such that the plane containing the two sources' axes was perpendicular to the x, z mapping plane. Any effects of misalignment of the mirror system are now out of the measurement plane. Measurements for two values of the ion density ratio are presented: Case B.1 - $n(Ne^+)/n(Kr^+) \approx 2.5$ and Case B.2 - $n(Ne^+)/n(Kr^+) \approx 4.5$. There is no substantial difference between Case B.1 and Case B.2 except that more measurements along x were performed at a particular z location to illustrate a peculiar ion behavior. The reference points for the coordinate positions are the same as in Case A.

The variation of the normalized ion current density with transverse position for two downstream positions is presented in Figures 27 and 28. The total ion current density from the FC is shown in Figure 27 while the separate ion component current densities are depicted in Figure 28. The normalization used in Figure 28 is calculated in the same manner as Case A (see Figure 24). The peaks in the total ion current density in Figure 27 are approximately located on the chamber axis for each case and each z position. The Ne^+ data (the major ion in this case) shows an off-axis peak in Figure 28. Adjustments to Ne^+ in the plasma source during DIFP data acquisition and between FC profile measurements are responsible. This data was acquired shortly after full power was applied to the plasma source. It was found that the plasma source needs $30-45$ minutes to stabilize. In the experiments described below, adequate time was allowed for stabilization. The gradients in the transverse ion current are approximately the same as in Case A. The Kr^+ appears in general to spread evenly in the plane of the mapping region. Additional data indicates that when asymmetries develop in the Ne^+ and Kr^+ profiles, both ion streams are moving to the $-x$ side of the chamber.

Figure 29 shows the vector flow field for each case. The general non-alignment of the Ne^+ and Kr^+ streams is still apparent. There is even a Ne^+ divergence on

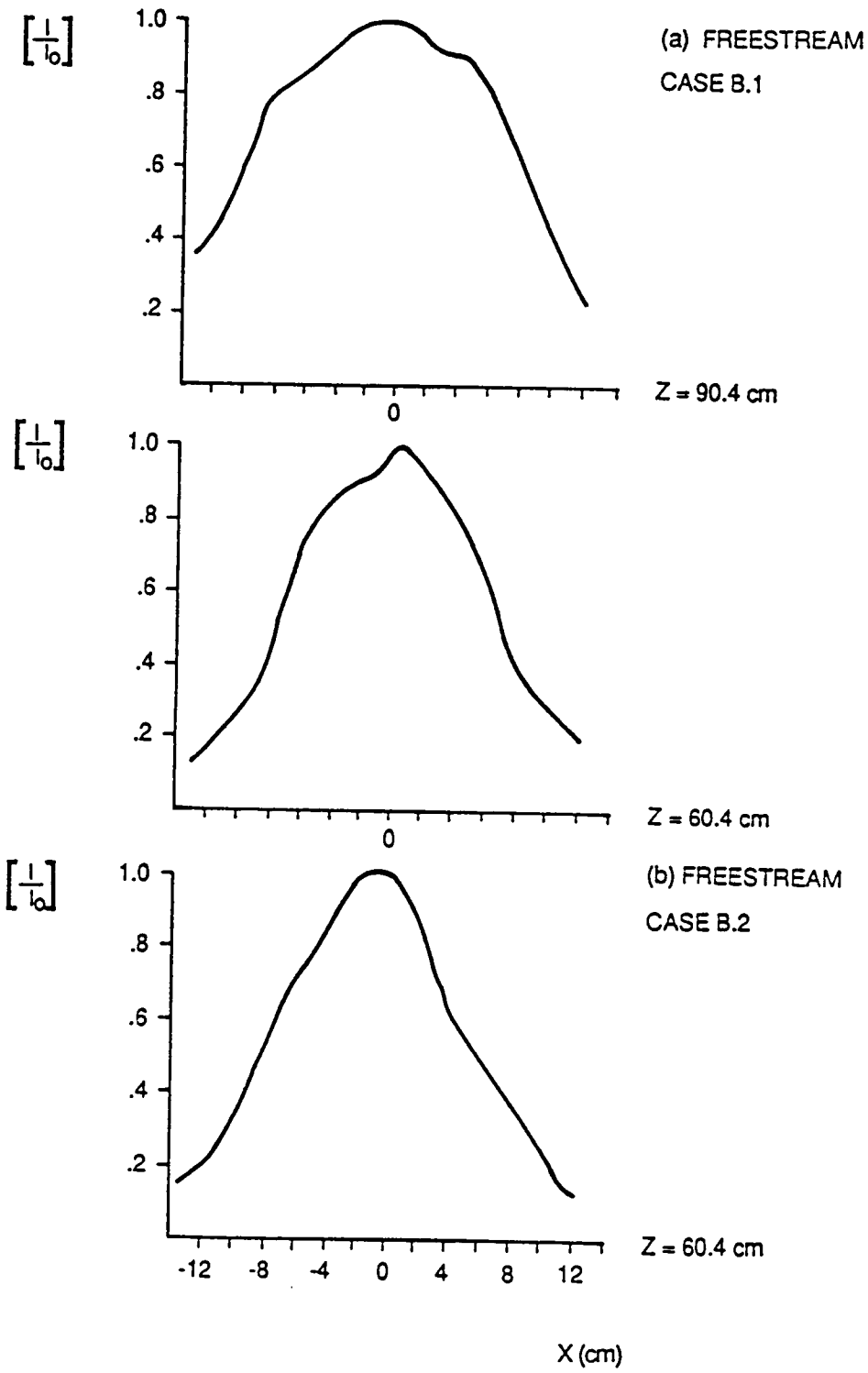

Figure 27. Variation of the normalized total ion current density with transverse position for various downstream locations from the plasma source. (a) Free-stream Case B.1. (b) Free-stream Case B.2.

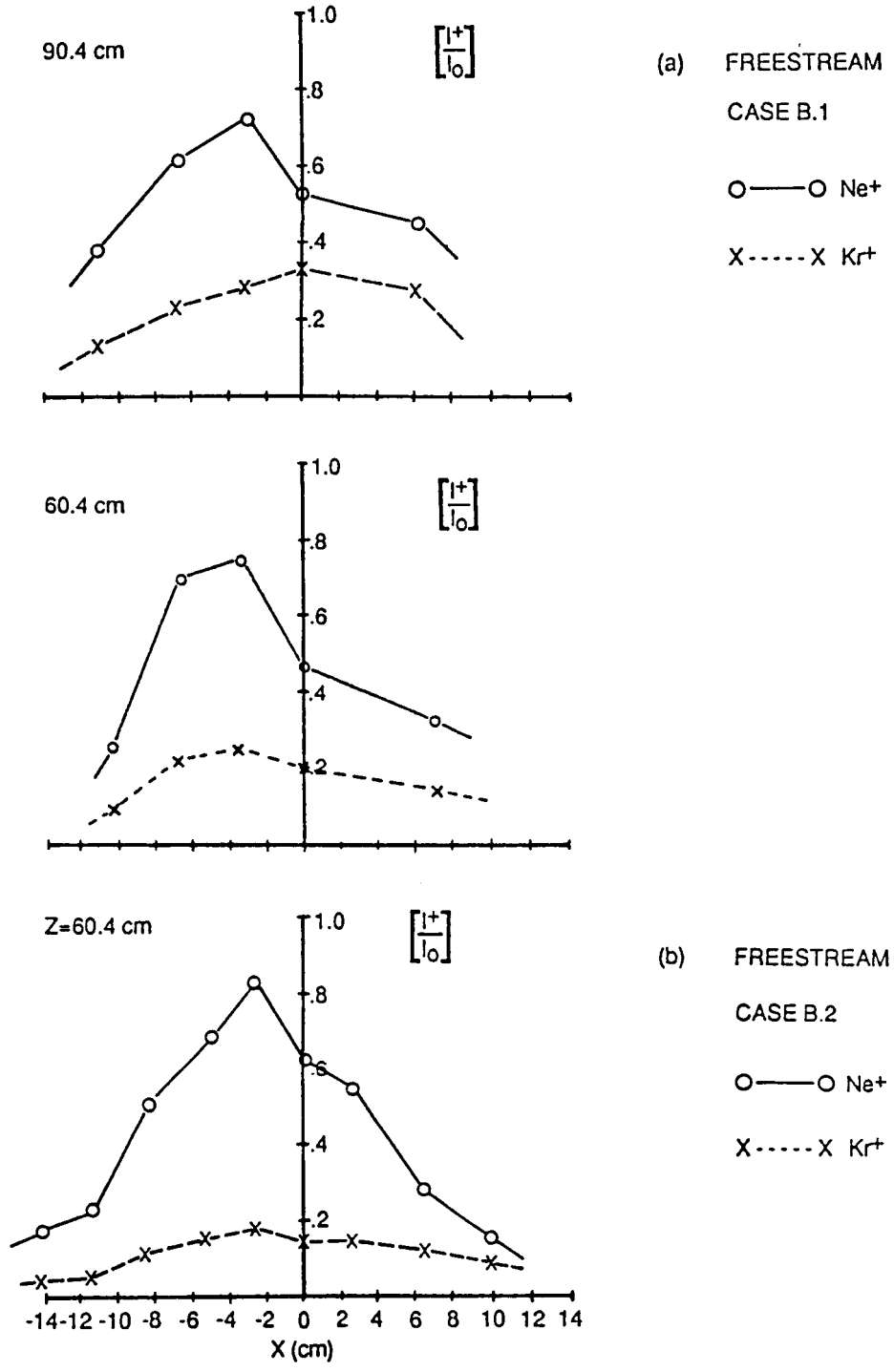

Figure 28. Variation of the normalized percentage ion component current densities with transverse position for the downstream locations in Figure 27. (*a*) Free-stream Case B.1. (*b*) Free-stream Case B.2.

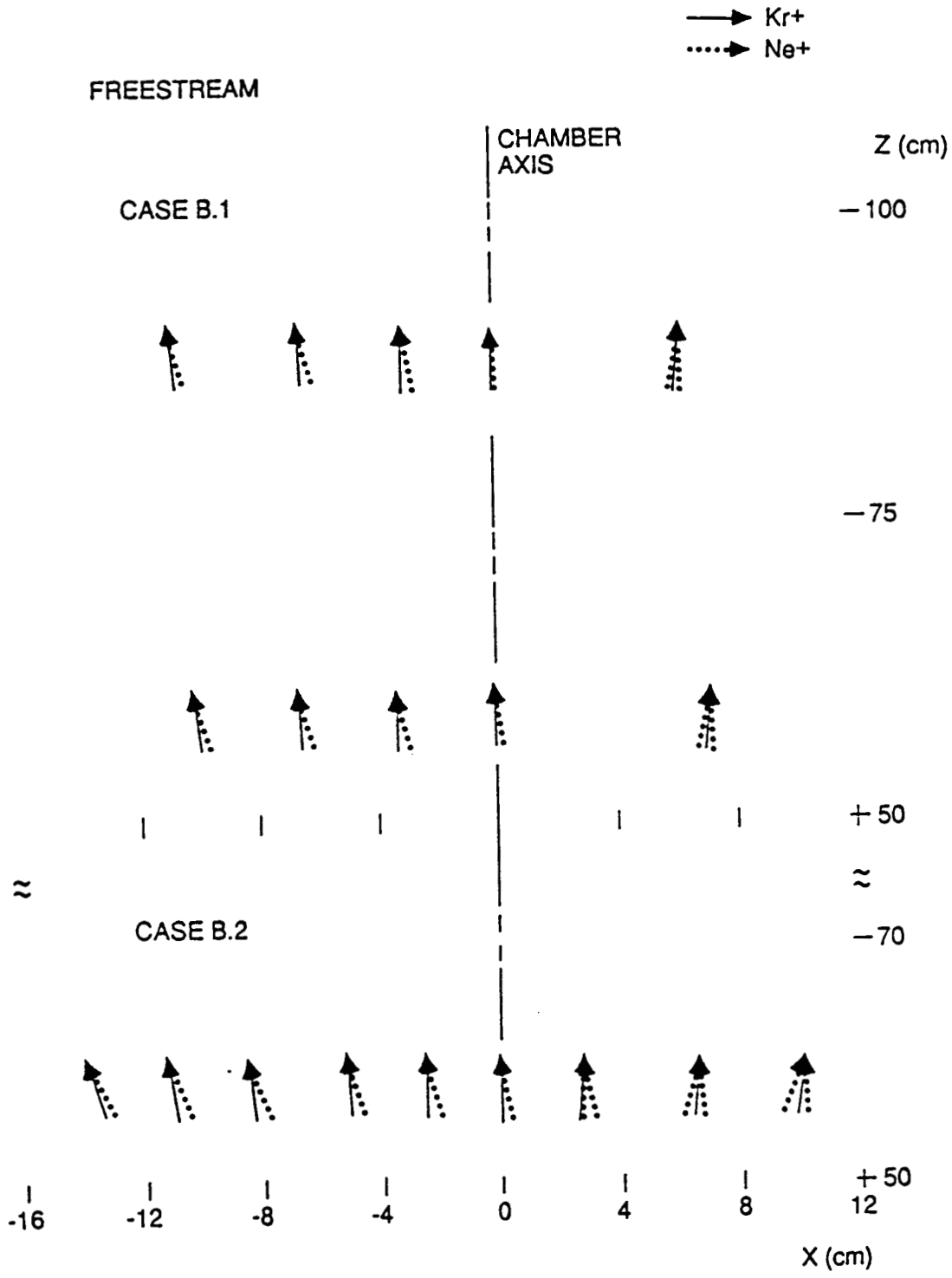

Figure 29. Velocity flow field for each ion constituent in the free-stream Cases B.1 and B.2. Notation is the same as in Figure 25.

the chamber axis; i.e., $\theta_{Ne^+}(x = 0) \neq 0°$. No additional Ne^+ streams were observed for $x < 0$; but now, it appears that the region for $x > 0$ is occupied by two Ne^+ streams. The presence of the extra Ne^+ stream is due to the B_{MIRROR} and B_{EXIT} fields. If $B_{MIRROR} = 0$ and B_{EXIT} is below a critical value, the additional Ne^+ stream is not present or at least is below the instrument sensitivity. As mentioned above in section B.1, the additional Ne^+ streams apparently have their origin in the complicated magnetic field geometry of the mirror region.

Figure 30 presents the quantitative difference between the Ne^+ and Kr^+ flow. Note the different y-axis scales used in the graphs for each ion. The Ne^+ angle data for $x > 0$ is complicated because of the presence of the second stream. The V-shaped profile (showing the change in polarity of the angle) is still present. The points which do not follow that profile are negative angles. For $x < 0$, the Ne^+ angles have a smaller variation in angle with x position and are smaller in magnitude as compared with Case A, while the Kr^+ angle variation and values are similar to Case A.

In summary for Case B, the orientation of the binary ion plasma source is such that the plane containing the Kr^+ and Ne^+ sources' axes is perpendicular to the x, z mapping plane. The FC data for total ion current shows a more or less symmetric profile with respect to the chamber axis and similar transverse current gradients to those of Case A. The divergence of Ne^+ relative to Kr^+ is still present. The region for $x > 0$ is occupied by two Ne^+ streams, while the variation of the Ne^+ flow angles for $x < 0$ is less than the variation measured for Case A. The Kr^+ flow angles are similar to those in Case A.

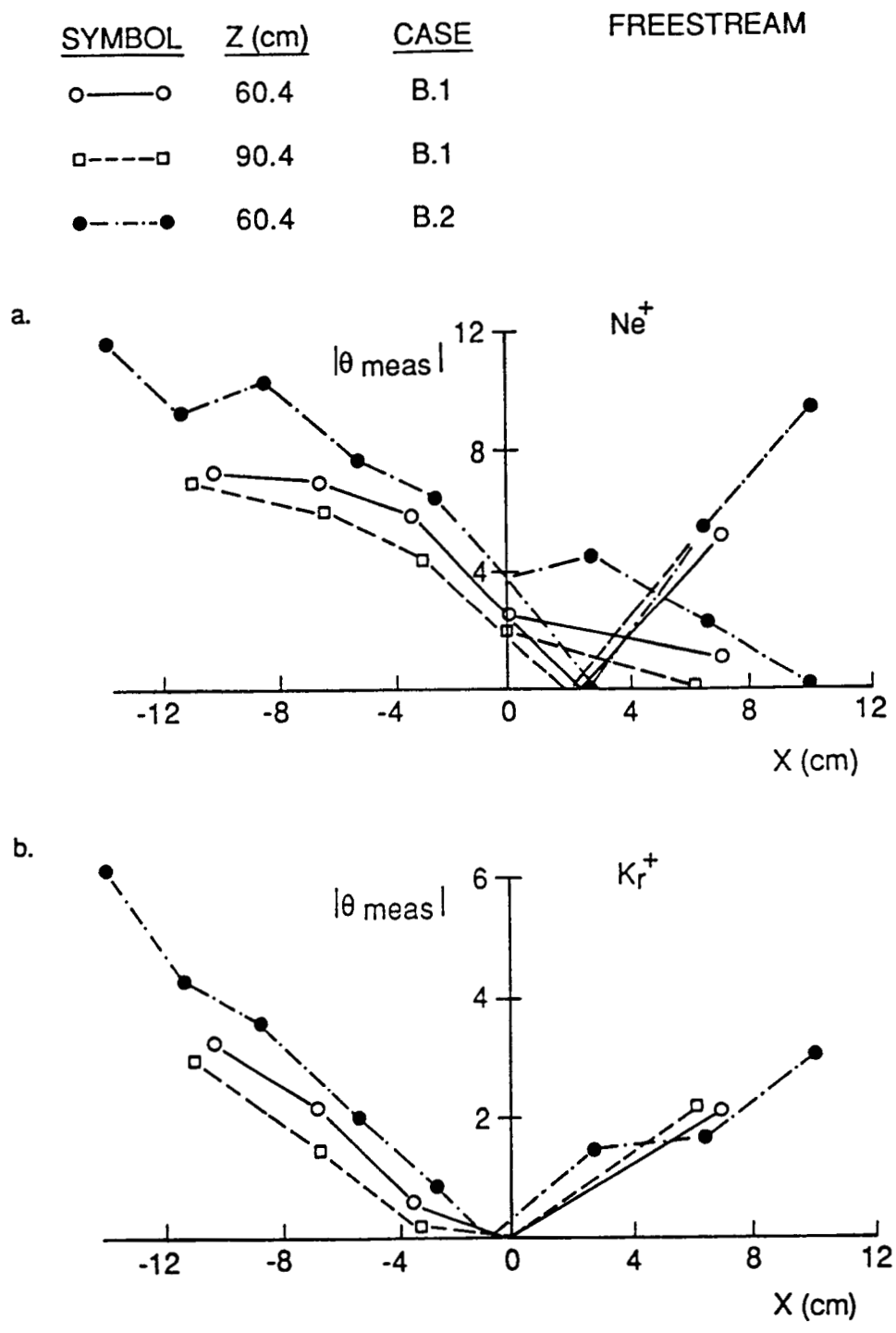

Figure 30. Variation of the measured ion flow angle magnitude with transverse position for the downstream locations in Figure 27. (*a*) Ne^+. (*b*) Kr^+.

C. Binary ion plasma wake experimental data

The experiment was performed with the binary ion plasma source oriented as in the free-stream Case B. Figure 22 then represents a side view of the source with the vacuum chamber on the right. A large conducting flat plate was placed in the chamber at $z \simeq 62\,\text{cm}$ from the exit neutralizer. If the plate is placed at $z \simeq 100\,\text{cm}$ from the plasma source, as in the single ion plasma experiment, only a range of 20 cm is accessible in the z position for probe movement. The plate location of $z \simeq 62\,\text{cm}$ then allowed for roughly the same spatial mapping area as before. The plate was positioned so that it occupies the $x > 0$ region with one edge on the chamber axis. The additional Ne^+ streams are thus blocked and did not effect the experiment. Allowing the plasma to flow over only one edge of the plate simulates the large body case; i.e., $R_D \gg 1$.

The plate was maintained at ground potential throughout the experiment. With the space potential at +2 to + 3 volts, the potential difference between the plasma and the plate serves to decrease the Ne^+ flow divergence near the plate edge. That is, the Ne^+ flow becomes more aligned with the chamber axis and also with the Kr^+ flow. Recall from Figure 29 the non-zero flow angle for Ne^+ occurring on the chamber axis.

Some general reminders about the plasma beam are now mentioned. The divergence of the Ne^+ stream at the plate location is smaller than its divergence for the source orientation of Case A, but it is still larger than the beam divergence at the plate location in the single ion plasma experiment. Also the transverse current gradient at the plate location is much larger than in the single ion plasma experiment. The plasma beam profile in the $y-$direction along the plate edge, as illustrated by the measurements in free-stream Case A, cannot be considered constant. Three dimensional aspects will, therfore, play a role in the wake filling process, but are

not addressed in the present study. The pertinent electron temperature to ion temperature ratio is estimated to be $T = T_e/[T_{i_\perp}]_{eff} \simeq 4.5 - 7.5$.

Three experiments were performed for different values of the ion component density ratio: Case I $- n(Ne^+)/n(Kr^+) \simeq 2$; Case II $- n(Ne^+)/n(Kr^+) \simeq 0.5$; and Case III $- n(Ne^+)/n(Kr^+) < 0.2$. These particular values are only approximate since, as was shown in the preceeding section, the $n(Ne^+)/n(Kr^+)$ ratio varies with both x and z positions. Therefore, the value assigned for $n(Ne^+)/n(Kr^+)$ for each case represents the condition determined from the ambient measurements near the plate edge. The measurement procedure was the same as in the single ion plasma experiment. The probes are located at a particular z position and maneuvered along the x position. This is repeated for the next larger z position until the mapping region has been covered.

The data for each case is presented in the following three sub-sections, with only brief comments about the data for the purpose of clarification. General discussion and comparison are deferred to section D.

1. Case I: $n(Ne^+)/n(Kr^+) \simeq 2$. Figures 31 and 32 present the normalized transverse current density profiles for various downstream positions from the plate. Figure 31 shows the total ion current density measured by the FC while Figure 32 shows the percentage of each ion component current density as determined by the DIFP. In Figure 31, and in subsequent plots of this type, the curve is truncated when the ion current level reaches zero. The difference in the location where the ion current reaches zero between Figures 31 and 32 is due to the difference in sensitivity between the electrometers of the DIFP and the FC.

The z variation of the ambient $n(Ne^+)/n(Kr^+)$ ratio seen in Figure 32 is in general an effect of the evolution of the beam. It is difficult to control the $n(Ne^+)/n(Kr^+)$ ratio far downstream from the plate. It appears that space charge effects in the beam are spreading the Ne^+ both in and out of the measurement

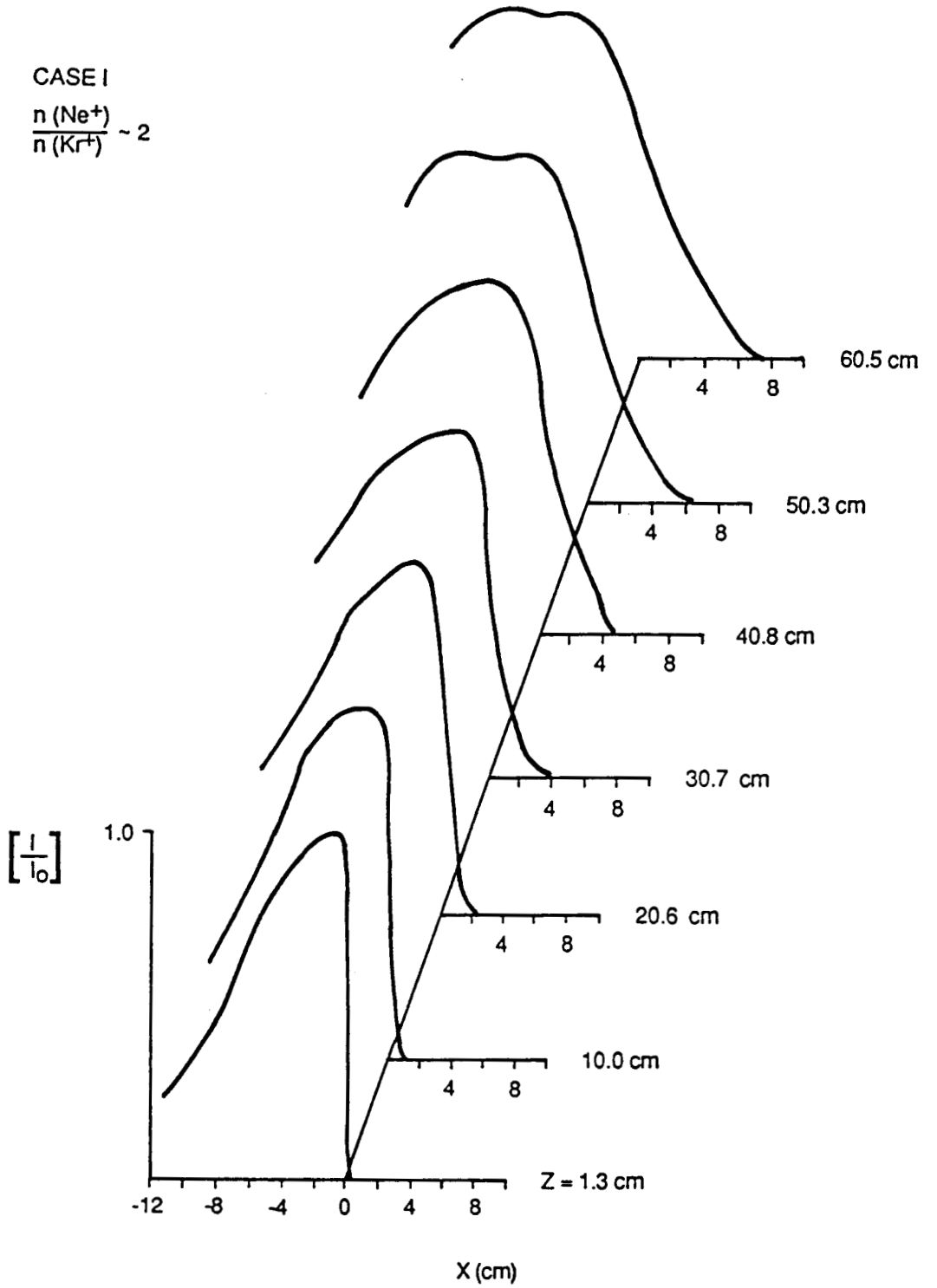

Figure 31. Variation of the normalized total ion current density with transverse position for several downstream locations from the plate for experiment Case I: $n(Ne^+)/n(Kr^+) \simeq 2$. The plate extends in the $+x$ direction with the edge located at $x = 0$. A current profile is truncated when the value of the current is zero.

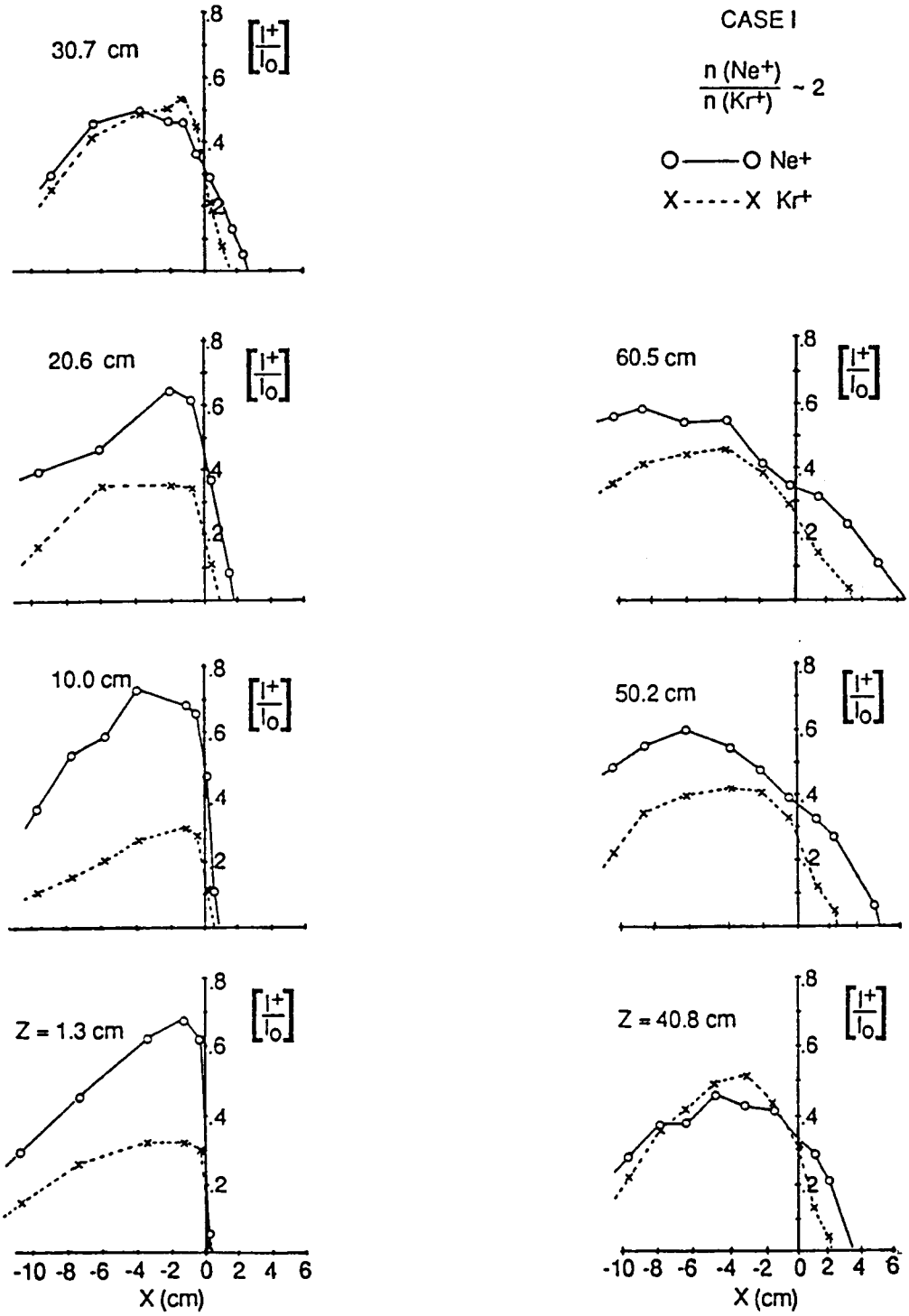

Figure 32. Variation of the normalized percentage ion component current densities with transverse position for the downstream locations in Figure 31 for experiment Case I: $n(Ne^+)/n(Kr^+) \simeq 2$.

plane. However, it was discovered that the output of the plasma source changed during the DIFP data acquisition for the $z = 40.8\,\text{cm}$ position. The beam conditions were re-adjusted at the $z = 1.3\,\text{cm}$ postion and then the data for $z = 50\,\text{and}\,60\,\text{cm}$ was obtained. The data for $z = 30.7\,\text{cm}$ was obtained from a different run (Case I.2), in which conditions of the beam near the plate were matched to those near the plate for the rest of the data (Case I.1). Obviously some differences did exist since the density ratio is approximately unity at $z = 30.7\,\text{cm}$.

Figure 33 shows the vector flow for each ion constituent. The action of the electric field between the plasma and the grounded plate is seen to roughly align the Ne^+ and Kr^+ flow near the plate edge. An additional Ne^+ stream has appeared in the left edge of the plasma beam, as viewed from the plasma source. It is apparent that the boundary condition of the plate imposed on the plasma beam has brought what was the outer edge of the free-stream closer to the chamber axis. This region of the additional Ne^+ stream apparently existed for free-stream Case B, but measurements were not made far enough away from the source axis or close enough to the source to detect it. The existence of the second Ne^+ stream at the outer edge of the ambient plasma should not affect the filling process in the wake of the plate. When an extra Ne^+ stream exists at a measurement point, the currents of both streams are added to obtain the value for Ne^+ shown in plots like that of Figure 32.

The plasma conditions for Case I are shown in Table 3. The T_e and ϕ_{sp} values represent an average over the ambient plasma region, while the other values pertain to the region near the plate edge. Other comments on notation are: the total ion density is represented as n_{tot}; the % ion species refers to the ion fraction of the total density; the ion acoustic speed, C_S, is determined from (4.2); and the normalized body potential is given by $\Phi_B = e(\phi_{plate} - \phi_{sp})/kT_e$. These comments also apply to the following tables for the other two cases.

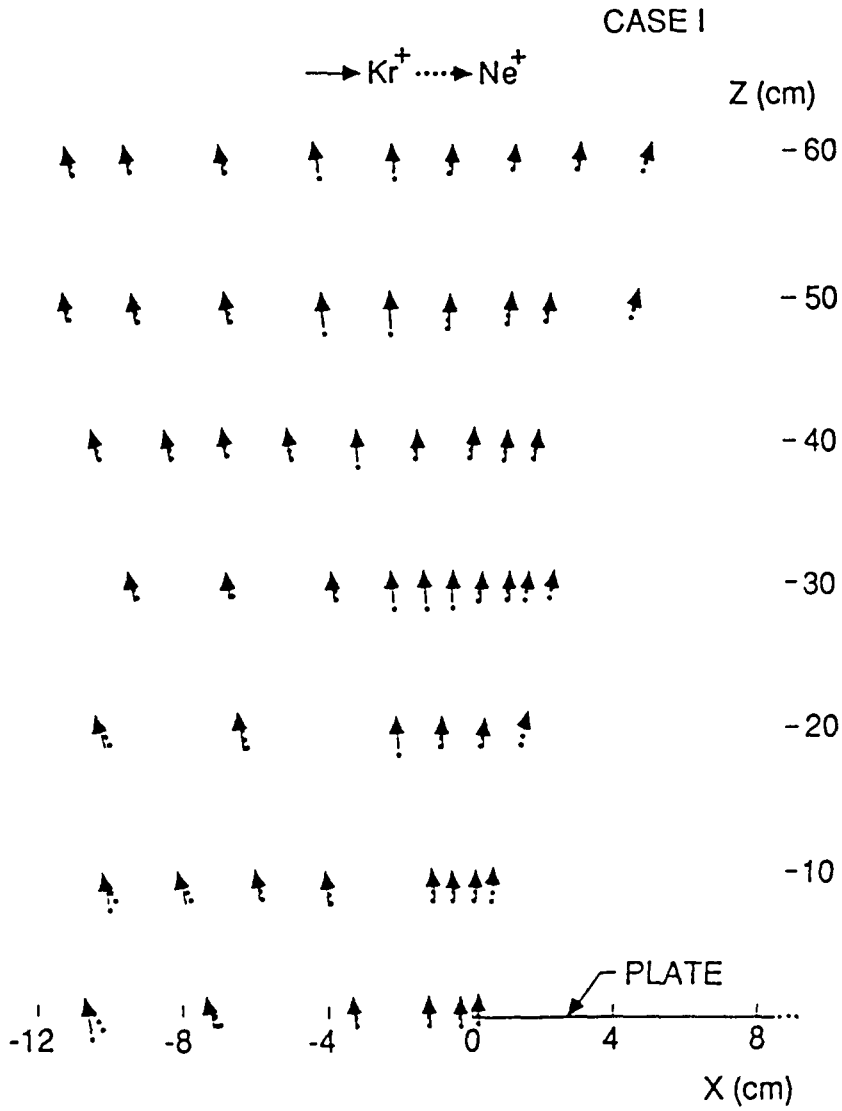

Figure 33. Velocity flow field for each ion constituent in experiment Case I: $n(Ne^+)/n(Kr^+) \simeq 2$. Notation same as Figure 25.

Table 3. Plasma conditions for Case I.

	I.1	I.2
V_{flow}(cm/s)	1.47×10^6	1.41×10^6
n_{tot}(cm^{-3})	8.1×10^4	7.8×10^4
$\%Ne^+$	0.67	0.63
$\%Kr^+$	0.33	0.37
T_e(eV)	0.29	0.29
C_S(cm/s)	1.02×10^5	1.0×10^5
ϕ_{sp}(volts)	+2.2	+2.0
$\mathcal{M}$	14.4	14.1
Φ_B	−7.6	−6.9
$n(Ne^+)/n(Kr^+)$	2.0	1.7

2. Case II: $n(Ne^+)/n(Kr^+) \simeq 0.5$. Figures 34, 35, and 36 serve the same functions as the corresponding figures in Case I. The current density profiles are compiled from three different experiment runs: II.1 for $z = 1.3, 9.7$ cm; II.2 for $z = 30.7$ cm; and II.3 for $z = 21.1, 40.6, 49.9, 60.5$ cm. The occurrence of an additional Ne^+ stream for a region of the ambient plasma is still present, as in Case I. Table 4 gives the plasma conditions for Case II.

Table 4. Plasma conditions for Case II.

	II.1	II.2	II.3
V_{flow}(cm/s)	1.49×10^6	1.42×10^6	1.46×10^6
n_{tot}(cm^{-3})	11.3×10^4	8.8×10^4	9.3×10^4
$\%Ne^+$	0.35	0.35	0.40
$\%Kr^+$	0.65	0.65	0.60
T_e(eV)	0.34	0.32	0.38
C_S(cm/s)	9.07×10^4	8.8×10^4	9.94×10^4
ϕ_{sp}(volts)	+2.2	+2.0	+2.1
$\mathcal{M}$	16.5	16.1	14.7
Φ_B	−6.5	−6.3	−5.5
$n(Ne^+)/n(Kr^+)$	0.54	0.54	0.67

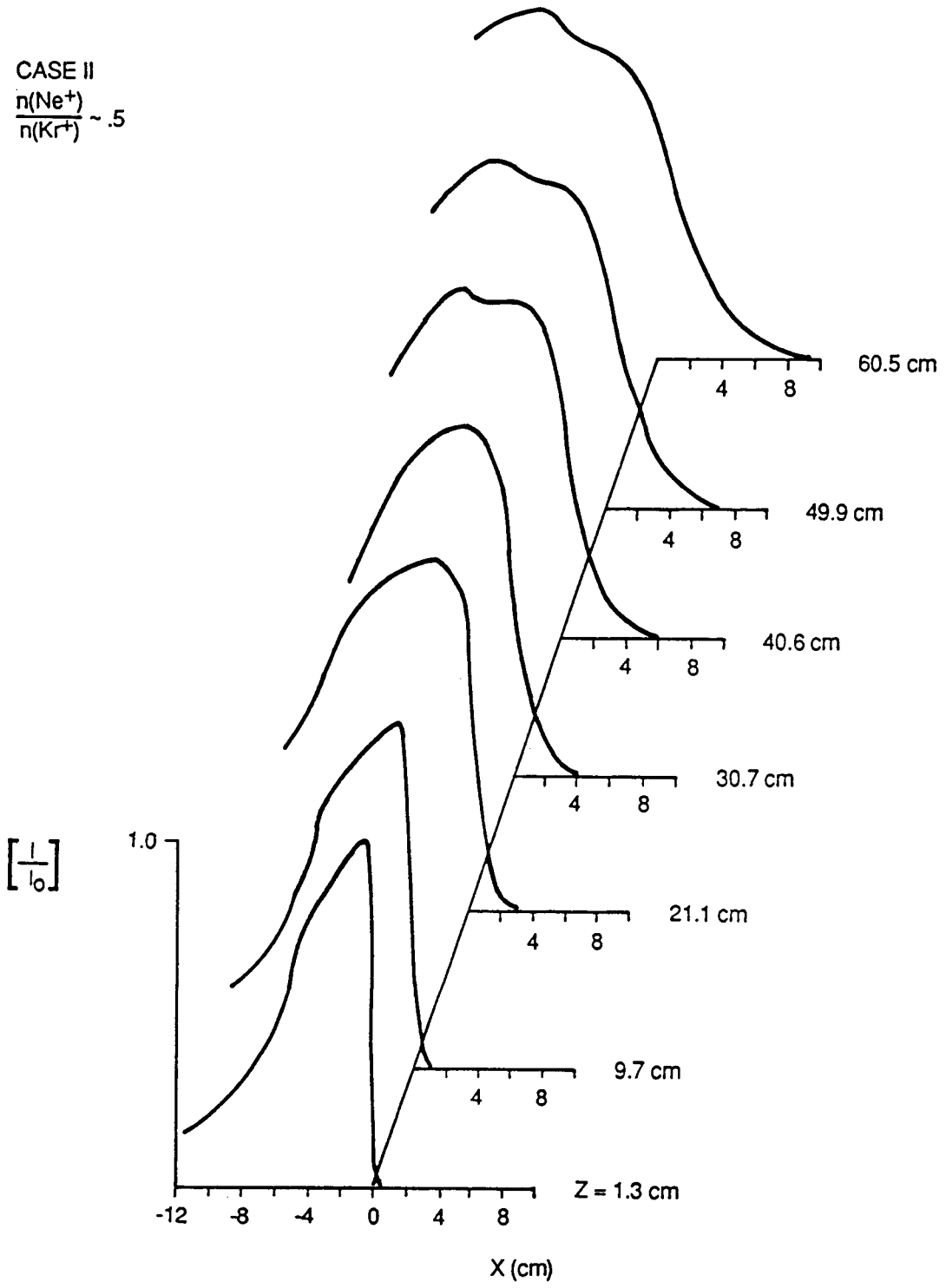

Figure 34. Same as Figure 31, except for experiment Case II: $n(Ne^+)/n(Kr^+) \simeq 0.5$.

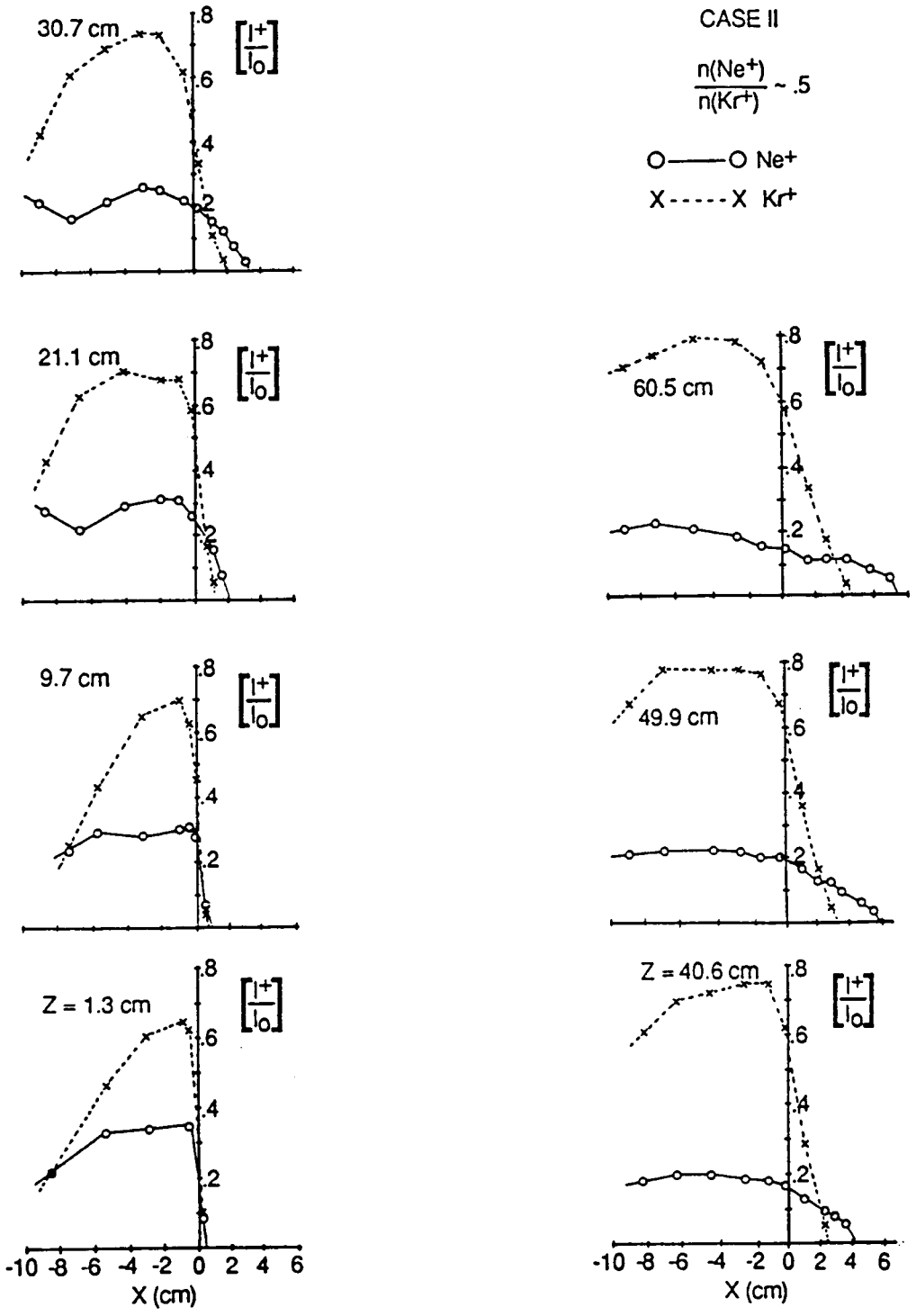

Figure 35. Same as Figure 32, except for experiment Case II:

$n(Ne^+)/n(Kr^+) \simeq 0.5$.

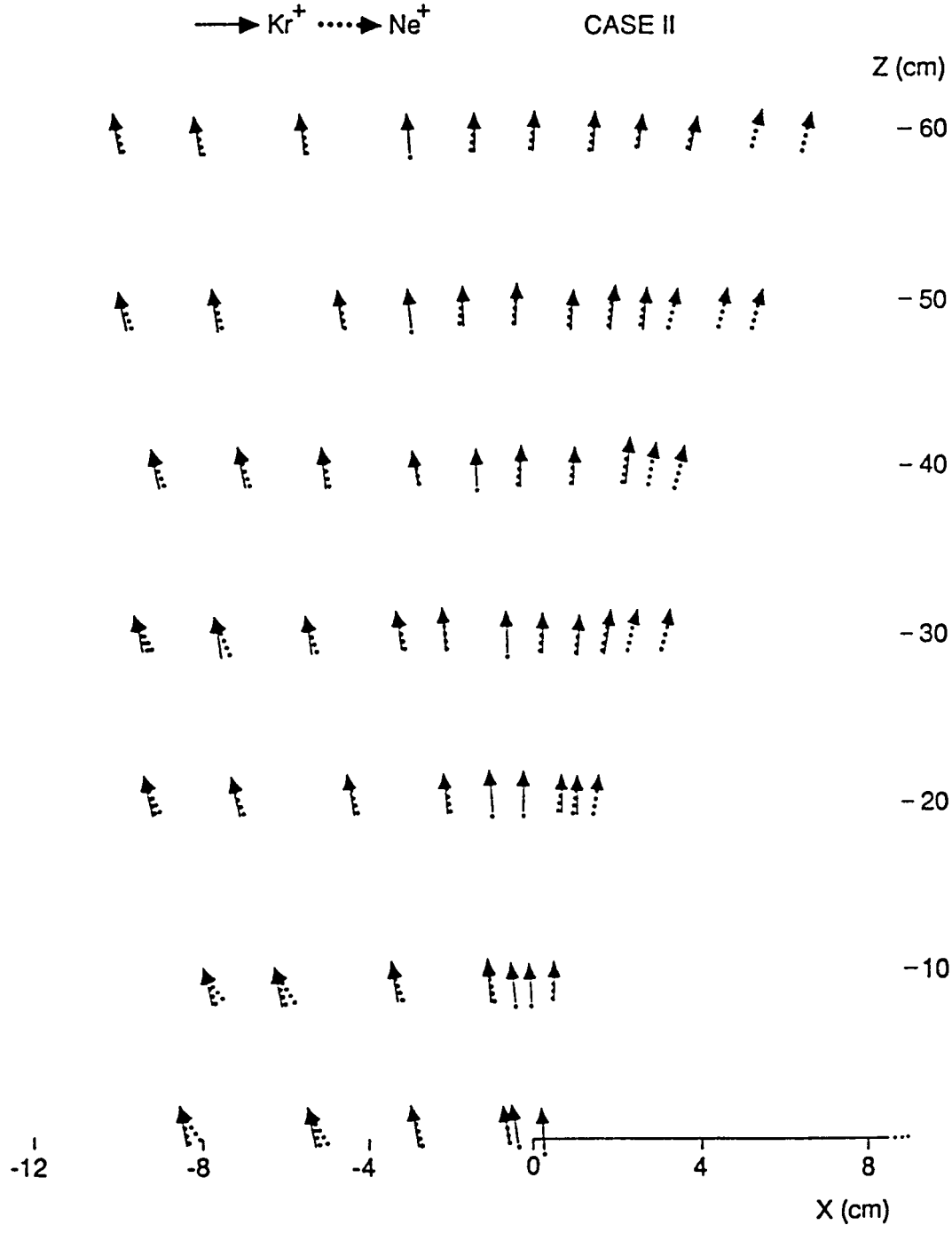

Figure 36. Same as Figure 33, except for experiment Case II:
$n(Ne^+)/n(Kr^+) \simeq 0.5$.

3. Case III: $n(Ne^+)/n(Kr^+) < 0.2$. Figures 37, 38, and 39 again serve the same functions as the corresponding figures in Case I. Note that the $y-$axis scale for the Ne^+ current density in Figure 38 is increased by a factor of two and displayed on the right of each panel. All data are obtained from the same experiment run. Again the additional Ne^+ stream is present in Figure 39 as in the two previous cases. Table 5 shows the plasma conditions for Case III. Note that the space potential is higher than for the other two cases.

Table 5. Plasma conditions for Case III.

V_{flow}(cm/s)	1.45×10^6
n_{tot}(cm^{-3})	9.4×10^4
$\%Ne^+$	0.15
$\%Kr^+$	0.85
T_e(eV)	0.34
C_S(cm/s)	7.6×10^4
ϕ_{sp}(volts)	+2.8
$\mathcal{M}$	19.1
Φ_B	-8.2
$n(Ne^+)/n(Kr^+)$	0.17

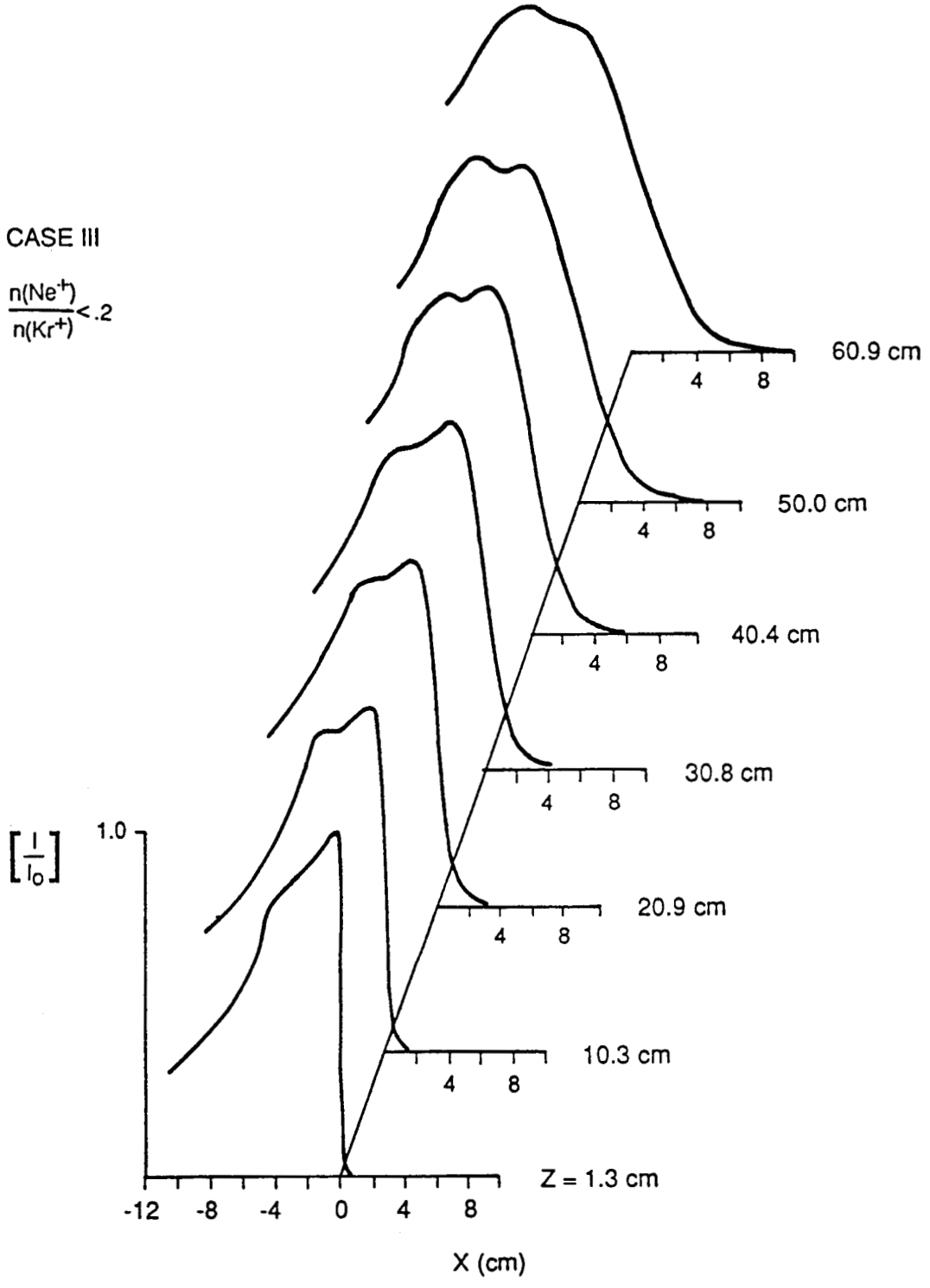

Figure 37. Same as Figure 31, except for experiment Case III: $n(Ne^+)/n(Kr^+) < 0.2$.

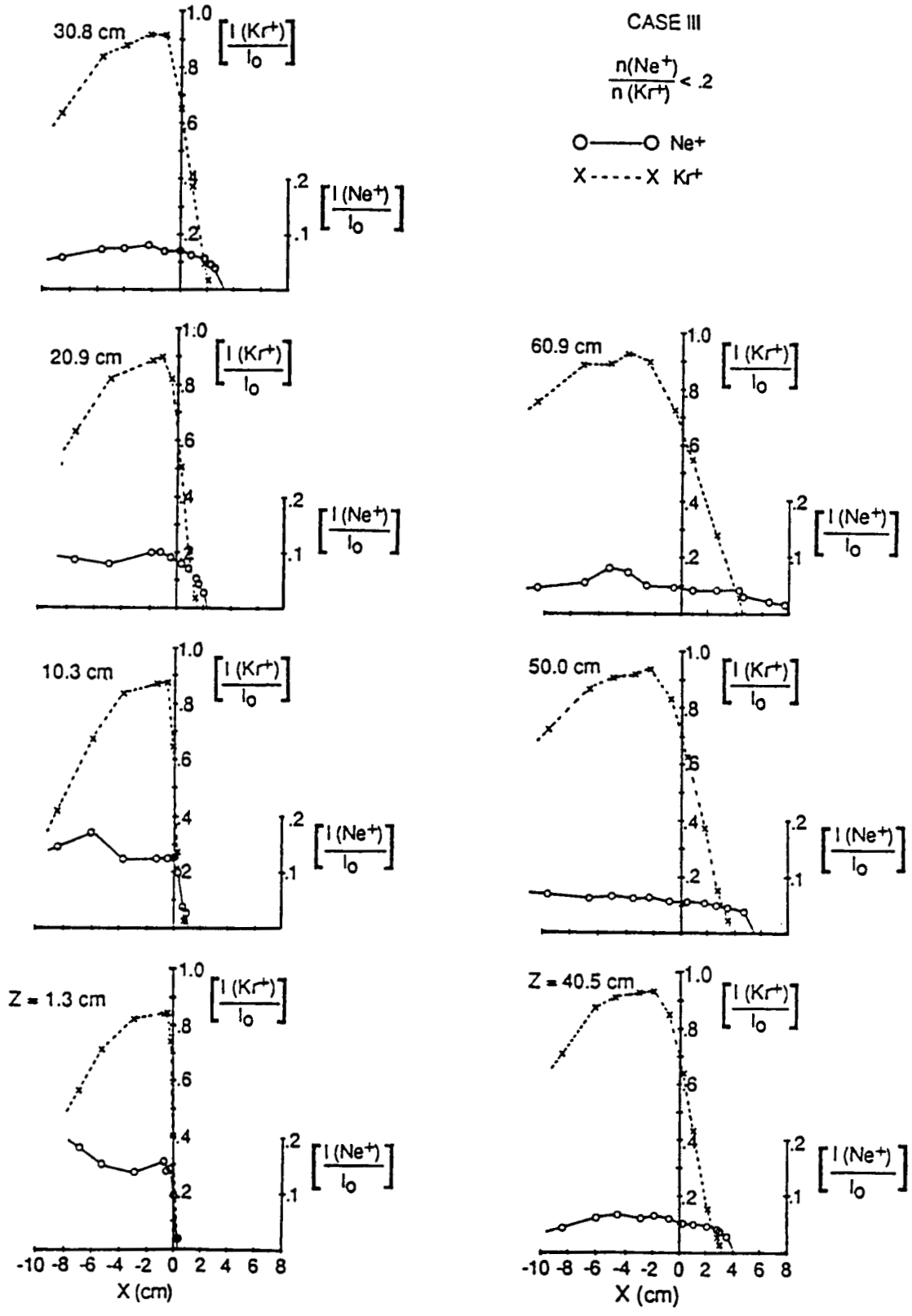

Figure 38. Same as Figure 32, except for experiment Case III: $n(Ne^+)/n(Kr^+) < 0.2$.

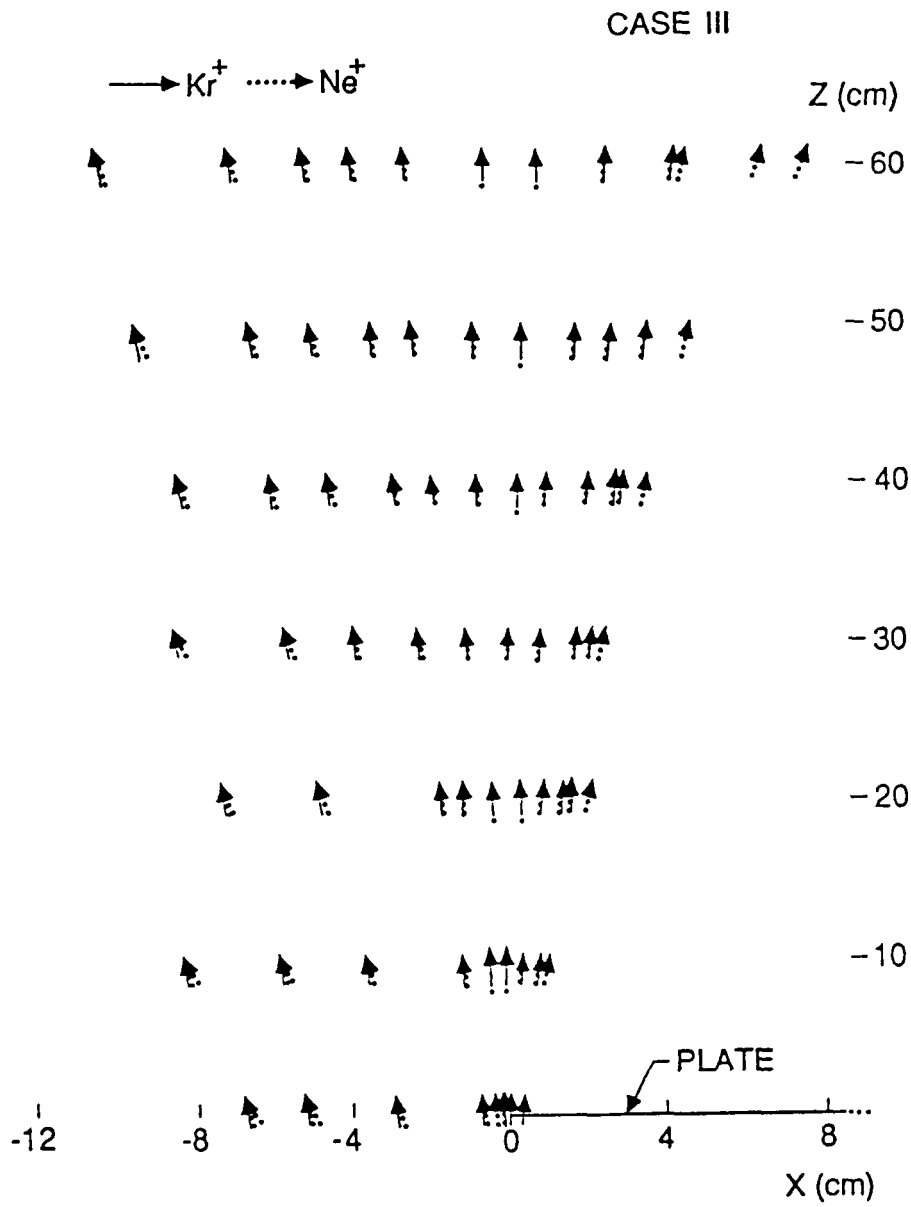

Figure 39. Same as Figure 33, except for experiment Case III: $n(Ne^+)/n(Kr^+) < 0.2$.

D. Discussion of the experimental results

The discussion is divided into two sections — one concerning the total ion current density obtained from the FC measurements and one concerning the ion component current density obtained from the DIFP measurements. The various regions of the wake are discussed in each section.

1. Total ion current density measurements. The measurements from the FC provide information about the spatial distribution of the total ion current density. The rarefaction wave and the ion behavior in the expansion region are examined.

a. *Rarefaction wave*. The disturbance boundary of the plasma-plate interaction, or the rarefaction wave, is observed to propagate into the ambient plasma at a speed C_S, where C_S is given by (4.2). Figure 40*a* presents the variation of the quantity $\Delta X \cdot \mathcal{M}$ with the downstream distance z for all three cases. Recall that $\Delta X = X_1 - X_0$, where X_1 = the location of the disturbance boundary in the transverse direction and X_0 = the disturbance location extrapolated to the plate location at $z = 0$, and $\mathcal{M} = V_{flow}/C_S$. The purpose of the plot is to show what factor multiplying ΔX will order the data along the solid line of slope = 1. By extension from the single ion plasma experiments, the dashed line indicates the ordering of the data if the factor S had been used ($S = \mathcal{M}/\sqrt{2}$). Figure 40*b* shows rarefaction wave data when the source was operated in the single ion plasma mode, with mono-ionic N_2^+ and Ne^+ plasmas. The rarefaction wave for these plasmas agrees with the previous single ion plasma experiment (see Figure 13); namely, that the rarefaction wave propagates into the ambient plasma at the speed $\sqrt{2}C_S$. However, more data for a single ion plasma using an inert gas is needed to verify this speed. For the mono-ionic N_2^+ rarefaction wave, the plasmas generated by the different sources used in the two experiments give consistent results.

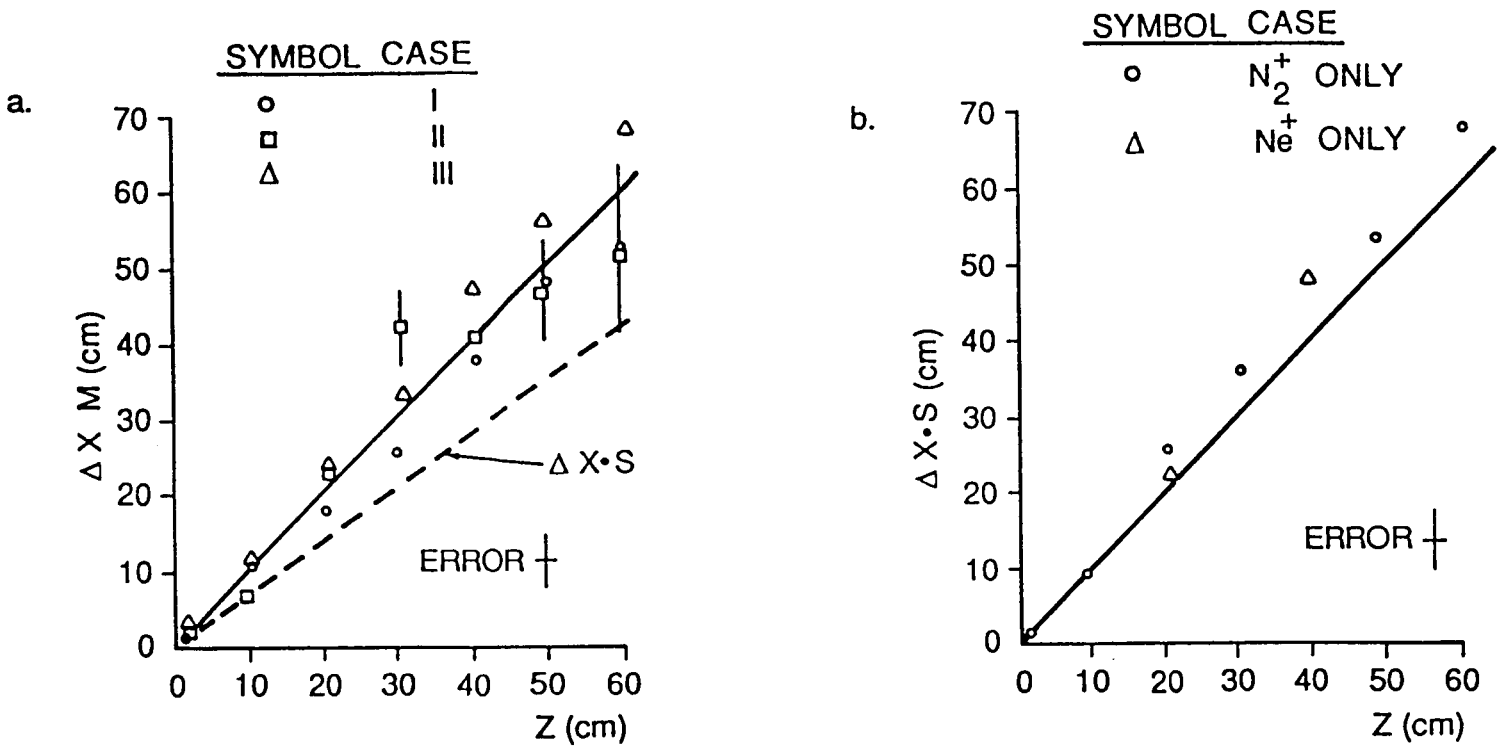

Figure 40. (a) Motion of the rarefaction wave point, ΔX, times $\mathcal{M}$ versus downstream position for all three cases of the binary ion plasma experiment. $\mathcal{M} = V_{flow}/C_S$, where C_S is given by (4.2). Dashed line represents the ordering of the data points if the factor S is used. $S = \mathcal{M}/\sqrt{2}$. (b) Motion of the rarefaction wave point, ΔX, times S versus downstream position. The binary ion plasma source is used in the single ion plasma mode with N_2^+ only and Ne^+ only.

A comparison of the rarefaction wave for the Ne^+, Kr^+ plasma and the monoionic N_2^+ plasma reveals a different propagation speed, C_S and $\sqrt{2}C_S$, respectively. The different heat capacities between an inert gas and a molecular gas may contribute to the speed difference. The general formula for an ion acoustic wave is given as

$$C_S = \left(\frac{\Gamma_e k T_e + \Gamma_i k T_i}{M_i} \right)^{\frac{1}{2}}, \tag{4.3}$$

where $\Gamma_{e,i}$ = specific heat capacities of electrons and ions, respectively. It is seen that corrections from both Γ_i and T_i can increase the acoustic speed. The value for Γ_i is larger for N_2^+ than Ne^+ or Kr^+ due to the extra degrees of freedom available for a diatomic molecule. As was pointed out in section IV.B, possible evidence of the different heat capacities between N_2^+ and Ne^+ or Kr^+ is observed in the different $T_{i_\parallel}$ measured for each type gas. A different $T_{i_\parallel}$ value, in large part, indicates differences in the creation of each ion in the source. However, a difference in the ion temperature between the experiment cases, either in the parallel or perpendicular direction, is not a contributing factor to the wave speed difference. The relative changes are going in opposite directions; i.e., T_i increasing in the binary ion plasma but rarefaction wave speed decreasing ($\sqrt{2}C_S \rightarrow C_S$).

There are predictions for the rarefaction wave motion from the plasma expansion into vacuum problem which treat the binary ion plasma case. No plasma expansion theory, however, treats a gas dependent effect. In examining the self-similar, quasi-neutral expansion for the case where the ambient charge density of one ion species is much greater than the ambient charge density of the other ion species, *Gurevich and Meshcherkin* [1981*a*] show for $\gamma > 1$ (with the heavy ion as the major ion) that the rarefaction wave motion for each ion constituent is the speed C_S. (In an earlier theory, however, *Gurevich et al.* [1973*a*] predict each ion species to propagate at different rarefaction wave speeds. See the discussion about Figure 5 in Chapter II.) *Anderson et al.* [1978] showed that this result also applied

for the same expansion where equal ambient charge densities were considered and $\gamma < 1$. In the present experiment for the range of density ratios which include both $\gamma < 1$ and $\gamma > 1$, the motion of the rarefaction wave, as determined by the total ion current density, is observed to be C_S, at least for the accessible measurement region.

b. *Expansion region*. The most obvious point to make about the wake region of the plate, concerning the total current density measurements for all cases, is the absence of the expansion front that was observed in the single ion plasma experiment (compare Figures 31, 34, and 37 with Figure 11). As mentioned in Chapter III, the expansion front was a persistent feature in several runs of that experiment, was also present for various applied plate voltages (see Figure 17), and was predicted theorectically. Several factors were studied in an attempt to understand the absence of the expansion front for the binary ion plasma expansion. First, the second ion component was removed. Plasma streams with Ne^+ only, Kr^+ only, and N_2^+ only were used. Two runs of N_2^+ were performed; first, using source #1 and second, using source #2 (see Figure 22). In no case did the expansion front appear with these single ion plasmas. Therefore, the addition of a second ion constituent to the plasma flow did not cause the disappearance of the expansion front.

The effective parallel beam temperature of the N_2^+ plasma flow was slightly larger than its value in the single ion plasma experiment case, but it was still factors of $2 - 10$ times smaller than the effective parallel beam temperatures of both Ne^+ and Kr^+. The effect of a larger velocity spread about the plasma drift velocity was not then playing a significant role in the disappearance of the expansion front.

Additional changes to the experimental set-up were tried. The plate was biased over a range of -5 to $+5$ volts, including zero, without observing the expansion front. The plate was re-located at $z \simeq 100$ cm from the source to test whether the density gradient in the ambient plasma was having any effect. The Ne^+, Kr^+, and

N_2^+ gases were used to generate single ion plasma flows and again the expansion front did not appear. The electrostatic mirror structure was removed to check whether it was having an influence on the plasma conditions; e.g., the perpendicular beam component of ion temperature. The three different gases were used, again, to generate single ion plasma flows and, again, the expansion front did not form.

It seems that a fundamental difference exists between the plasma flows created by the source used in the binary ion experiment and by the source used in the single ion experiment. The difference may be in the coupling of the electrons from the neutralizer wire located at the exit of each source. The extraction plates for the two sources possessed different hole sizes and numbers. As discussed in Chapter II, it is the electron pressure gradient which drives the ion expansion. The details of the electron distribution in the ambient plasma determine the ion behavior in the expansion region. Comparing the Langmuir probe (LP) data between the two experiments reveals that the degree of linearity on a semi-log plot, i.e. the 'Maxwellianity', is approximately one-and-a-half orders of magnitude for the single ion experiment, while for the binary ion case it is only an order of magnitude. The difference in the space potential and the small difference in density between the two experiments might lead to a question of whether a critical ambient electron density is involved for formation of the front. Further measurements of the plasmas from both sources are needed to determine exactly what differences between the plasmas are contributing to the disappearance of the expansion front.

The shapes of the transverse current density profiles for each case show a similarity to those in the single ion case; i.e., there is a concave portion of each profile. However, the range of the concave portion in the transverse direction is, in general, smaller. The details of the profile shape change with the $n(Ne^+)/n(Kr^+)$ ratio. Figure 41 presents a comparison of the variation of the normalized transverse current density for the farthest z position for each case. The region for approximately

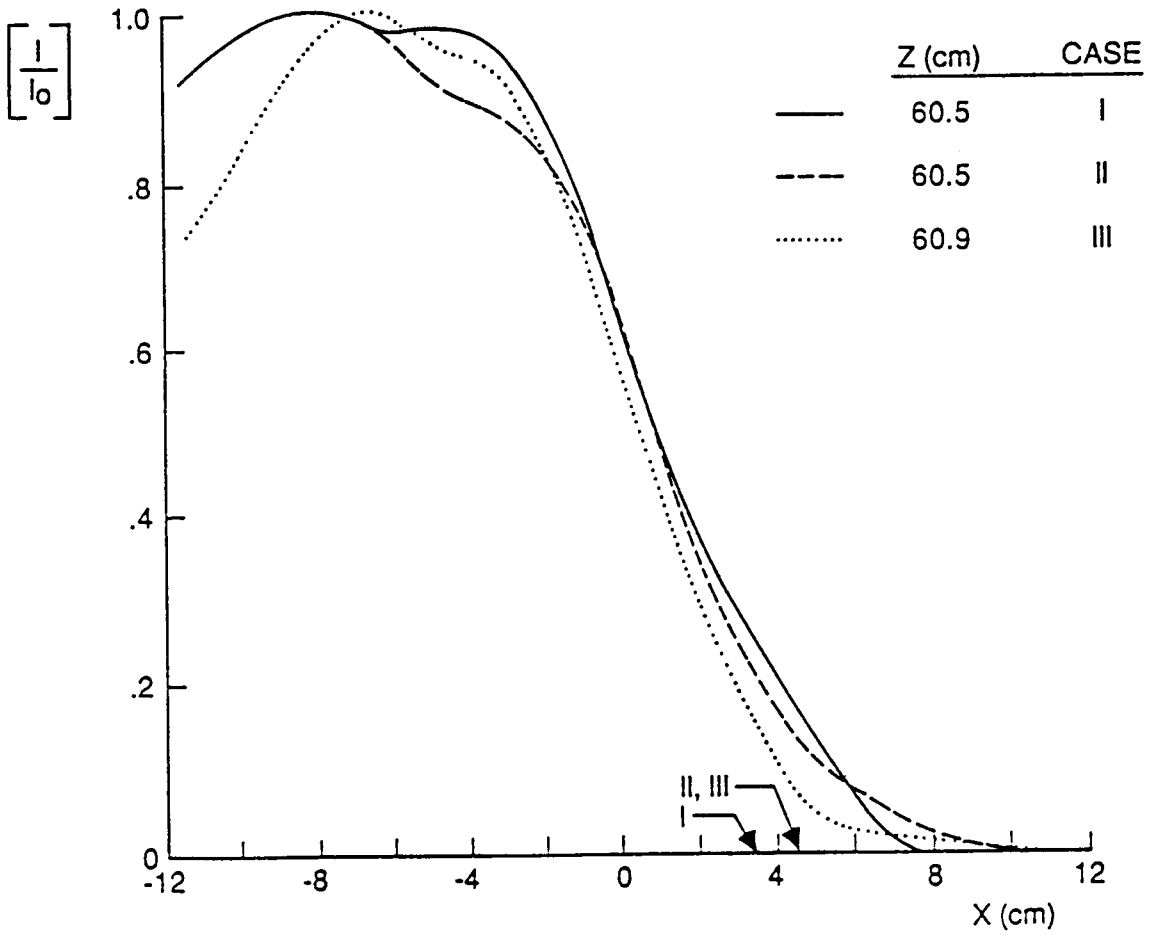

Figure 41. Variation of the normalized total ion current density with transverse position for all three experiment cases at the $z \simeq 60$ cm location. Data for Cases I, II, and III are taken from Figures 31, 34, 37, respectively. The location where the Kr^+ current, as determined by the DIFP, goes to zero is indicated for each case.

$x > -4\,\text{cm}$ is considered the expansion region for this z location. In general, as the percentage of Ne^+ is increased, relatively less current is observed at a particular x position. However, an extended 'foot' region is developed. The points where the Kr^+ current density reaches zero are marked on the $x-$axis, indicating that the 'foot' region consists entirely of Ne^+. The details of this behavior are discussed in the next section, which addresses the ion component measurements.

2. Ion component current density measurements. The ambient ion density ratio, $n(Ne^+)/n(Kr^+)$, decreases with downstream distance, as was pointed out in section C. In comparisons of the ambient $n(Ne^+)/n(Kr^+)$ ratio at $z \simeq 1.5\,\text{cm}$ with the ratio at $z \simeq 60\,\text{cm}$ for each case, it is observed that $n(Ne^+)/n(Kr^+)$ decreases by a factor of ≈ 1.5 for Case I, ≈ 2 for Case II, and ≈ 2.5 for Case III. The distinction between Case II and Case III then becomes blurred since the spatial change is of the order of the proposed parametric change; i.e., 0.5 to 0.2. Thus as the percentage of Ne^+ is decreased in the ambient, the percentage decrease in the $n(Ne^+)/n(Kr^+)$ ratio at the $z \simeq 60\,\text{cm}$ position becomes even greater.

a. *Rarefaction wave*. The spatial distribution of the DIFP measurement locations in the ambient plasma prevents a quantitative estimate of the rarefaction wave motion for each ion constituent. Recall that the DIFP internal voltage sweeps are not operated in the continuous manner needed to provide a continuous transverse profile; hence, measurements are performed at discrete locations. Measurements need to be performed closer than the 2 to 3 cm separation used here. However, a general qualitative tendancy is noted: the rarefaction wave for each ion species propagates at a different speed. An indication of the speed difference can be seen in Figure 42. The variation of the normalized current, for each ion species, with the transverse position at $z \simeq 60\,\text{cm}$ is shown for all three density ratio cases. The normalization current factor for each ion species is chosen to be its largest percentage current value in the ambient plasma at the $z \simeq 60\,\text{cm}$ position (see Figures 32, 35,

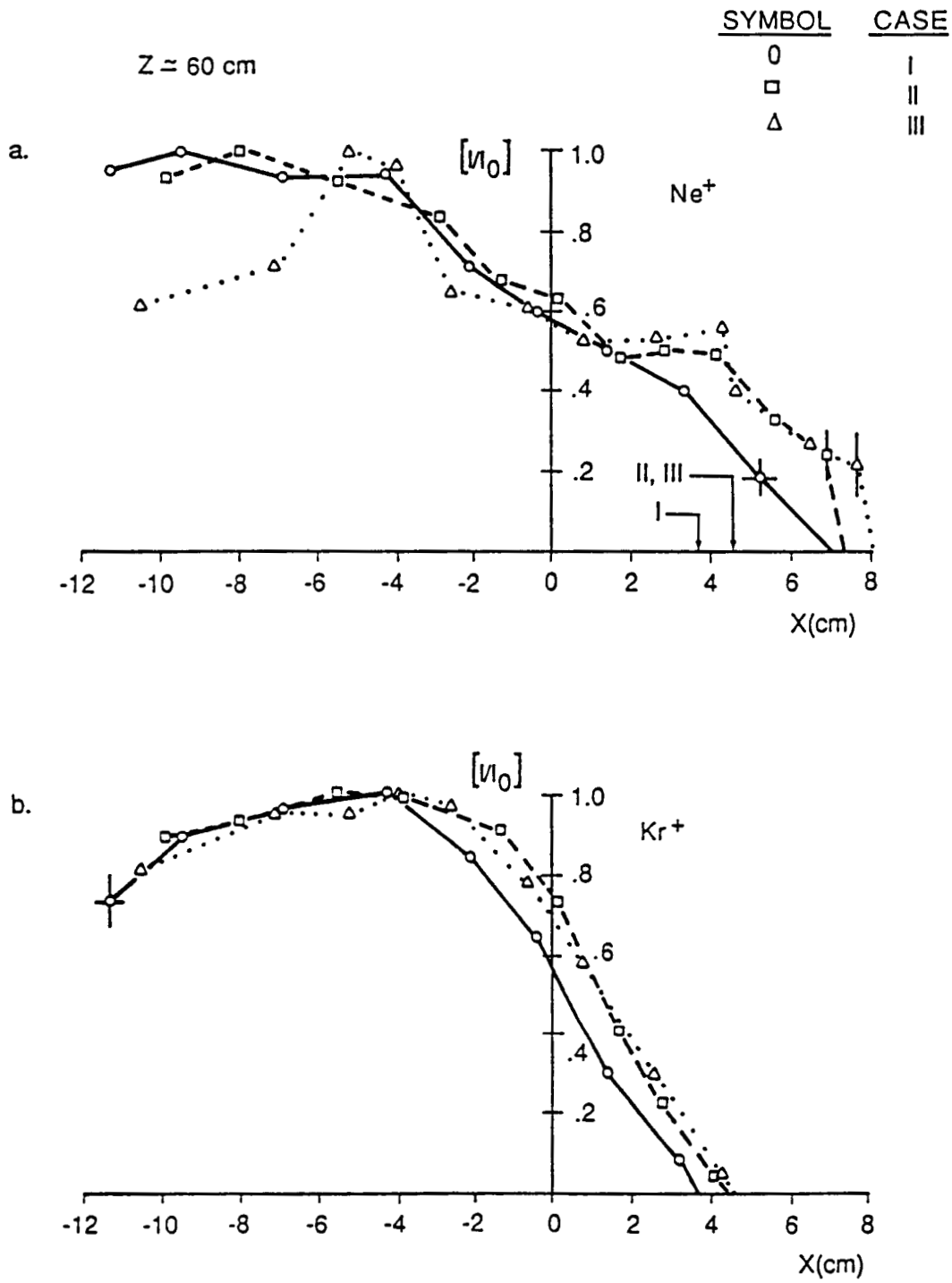

Figure 42. Variation of the normalized (a) Ne^+ and (b) Kr^+ component current densities with transverse position at the downstream location of $z \simeq 60$ cm from the plate for all three experiment cases. The data for each case is normalized by the largest ion component current for the particular case at this z position.

and 38). The rarefaction wave position, the location where $I/I_0 = 1$, for Ne^+ is roughly a factor of 2 greater than that for Kr^+. This factor for the speed difference is the ratio of the individual ion acoustic speeds; i.e., $C_S(Ne^+)/C_S(Kr^+) = 2$ since the mass ratio $M(Kr^+)/M(Ne^+) = 4$.

As mentioned above, in the theoretical plasma expansion results from *Gurevich and Meshcherkin* [1981*a*] and *Anderson et al.* [1978] for the quasi-neutral treatment, the rarefaction wave for each ion constituent is predicted to move at the same rate. However, the *Gurevich et al.* [1973*a*] quasi-neutral treatment, presented in Chapter II, predicts the ratio of the rarefaction wave speed for each ion component to be γ. This solution was derived under the assumption that the ambient density of one ion species was much greater than the other. Only case III can approach this criteria. If ion pressure effects are included [*Singh and Schunk*, 1983*a*; *Anderson et al.*, 1978], the rarefaction wave for each ion species is also found to move at different speeds, with the light ions again moving faster. In [*Singh and Schunk*, 1983*a*], charge separation effects are also included; i.e., Poisson's equation is used. These studies effectively apply to much longer times than the present experiment. A value for the longest time in the experiment is given by $\omega_{pi}(Ne^+)t = 3.8$, where the total ion density of the ambient at the plate location is used in the calculation of the Ne^+ plasma frequency and $t = z/V_{flow}$. However, as seen in the single ion plasma experiment, the rarefaction wave propagation should be constant throughout the expansion, so the result from the above studies should apply to even the small 'time scale' of the present experiment.

b. *Expansion region*. As was discussed in Chapter II for plasma expansion in the $\gamma > 1$ case (with the heavy ion as the major ion), the light ions will move relative to the heavy ions, eventually overtake the heavy ions and become the dominant species, and then, finally, the only ion species present (see Figure 5). When the heavy ion density goes to zero, *Gurevich et al.* [1973*a*] predict that a plateau region

will form. In the plateau region, the light ion density and velocity, and also the electrostatic potential remain essentially constant. The plateau region is predicted to become more pronounced as the value of γ increases. *Gurevich and Meshcherkin* [1981*a*] show numerical results for the quasi-neutral, self-similar solution for the case where $\gamma = 2$ and where $\gamma = 16$. For the $\gamma = 16$ case, an extended plateau is seen beginning at the location where the heavy ion density goes to zero. For the $\gamma = 2$ case, only a region of slow variation of the light ion density is seen. The range for this slow density variation is given by $\xi = 1$ to 4, where

$$\xi = \frac{x}{C_S t} \tag{4.4}$$

$$C_S = \left(\frac{kT_e}{M_2}\right)^{\frac{1}{2}}$$

and M_2 = the light ion mass.

In view of the theoretical predictions, recall that $\gamma = 4$ for Cases II and III of this experiment. The spatial distribution of the ion components in the experiment for Cases II and III show the light ions (Ne^+) moving through the heavy ions (Kr^+). For example, in Figure 42, which represents the ion expansion for the experiment in its most developed state (i.e., at the greatest distance from the plate), a region of slow variation in the Ne^+ current ('plateau-like' region) exists. In contrast, the Ne^+ current for case I ($\gamma < 1$) shows only a monotonic variation. The transverse velocity component is increasing over the plateau-like region, but only by values less than 10% of the Mach number. The plateau-like region then should also describe the Ne^+ density behavior over this spatial range. The plateau-like feature begins after the Kr^+ current has fallen below the $0.5I_0$ level. The total current measurements for the $z \simeq 60$ cm position, shown in Figure 41, do not show any evidence of the plateau-like feature. Since this feature begins at a position where there is still a

substantial Kr^+ current, the sum of the two components just shows a monotonic variation.

The range for the plateau-like feature of the Ne^+ current can be estimated from (4.4) to be $\xi_{exp} = 0.25 - 0.80$. The initial position and the width of the plateau-like feature are about a factor of four smaller than the values given by *Gurevich and Meshcherkin* [1981*a*] for the numerical result of the $\gamma = 2$ case. The equivalent expansion time for the experiment is small, but the positive space potential may effectively shift the ion expansion in the experiment to longer times, and, hence, allow development of the plateau-like feature. Although quantitative agreement with the plateau position is not achieved, Figure 42 definitely shows movement by the Ne^+ component through the Kr^+ component to form a region of slow variation of the current. At the position where the Kr^+ current density is observed to vanish, the Ne^+ expansion then proceeds. The variation of the current density for the last part of the Ne^+ only expansion, as determined by the DIFP, probably does not have a gradient that large. A better indication of the location where the Ne^+ current density goes to zero is obtained by the FC, since it has a higher sensitivity than the DIFP (see Figure 41). The result from Figure 42 shows that the 'foot' region of the total current density profiles for Cases II and III, shown in Figure 41, is populated only by Ne^+.

The Kr^+ data in Figure 42*b* also shows a difference between Case I and the other two cases. In the discussion on plasma expansion in Chapter II, it was noted that there is a higher electric field value for the earliest expansion stages in the $\gamma > 1$ case, with the heavy ion as the major constituent, as compared with the $\gamma < 1$ case, with the heavy ion as the minor constituent. For $\gamma < 1$, light ions rush ahead of the heavy ions and reduce the electric field. For $\gamma > 1$, there are relatively few light ions to rush out as the expansion begins, so that less screening occurs and the electric field is higher. The electric field acts on both the Kr^+ and Ne^+ ions,

so that a larger amount of Kr^+ moves into the expansion region. In Figure 42*b*, the Kr^+ data obtained at the $z \simeq 60$ cm position for Cases II and III illustrates the result of this effect; i.e., more current at a given x position.

c. *Leading edge of the expansion*. To quantify the acceleration of ions into the wake, the ion behavior in the leading edge, or foot region, of the expansion is examined. The quantities of Debye length, ion plasma frequency, and ion acoustic speed are used for normalization, as was done in the single ion plasma experiment. The change from the position variable to the analogous time variable is also made; i.e., $t = z/V_{flow}$. Use of the time variable, t, allows a better comparison between the three cases where different V_{flow} values, or Mach numbers, exist (see Tables 3, 4, and 5).

The boundary of the expansion region, or the foot point, is examined first. The change in location of the foot point for each ion constituent (the position at which the ion current is zero) is shown in Figure 43 as a function of the time variable. Since in Figure 42, it is shown that the expansion region foot of the total ion current density, illustrated in Figure 41, is entirely composed of Ne^+ ions, the FC measurement is used for the Ne^+ foot point. For the Kr^+ ions, the foot point position determined by the DIFP is used. Because there is no observation that Kr^+ has moved through Ne^+ at any downstream location (no extended 'foot' development for Kr^+), the Kr^+ foot point location determined by the DIFP should be fairly accurate and also allow a valid comparison with the Ne^+ foot point location determined by the FC. The foot point position for each ion species is normalized by Debye length, λ_D, and the time is normalized by the ion plasma frequency; i.e., $\omega_{pi}[M_i(Ne^+), n(Ne^+)]$ for Figure 43*a* and $\omega_{pi}[M_i(Kr^+), n(Kr^+)]$ for Figure 43*b*. The method that was followed concerning normalization is the same as in the single ion plasma experiment. That is, when discussing ions in the leading edge of the expansion (the expansion front in the single ion plasma case), the ambient ion

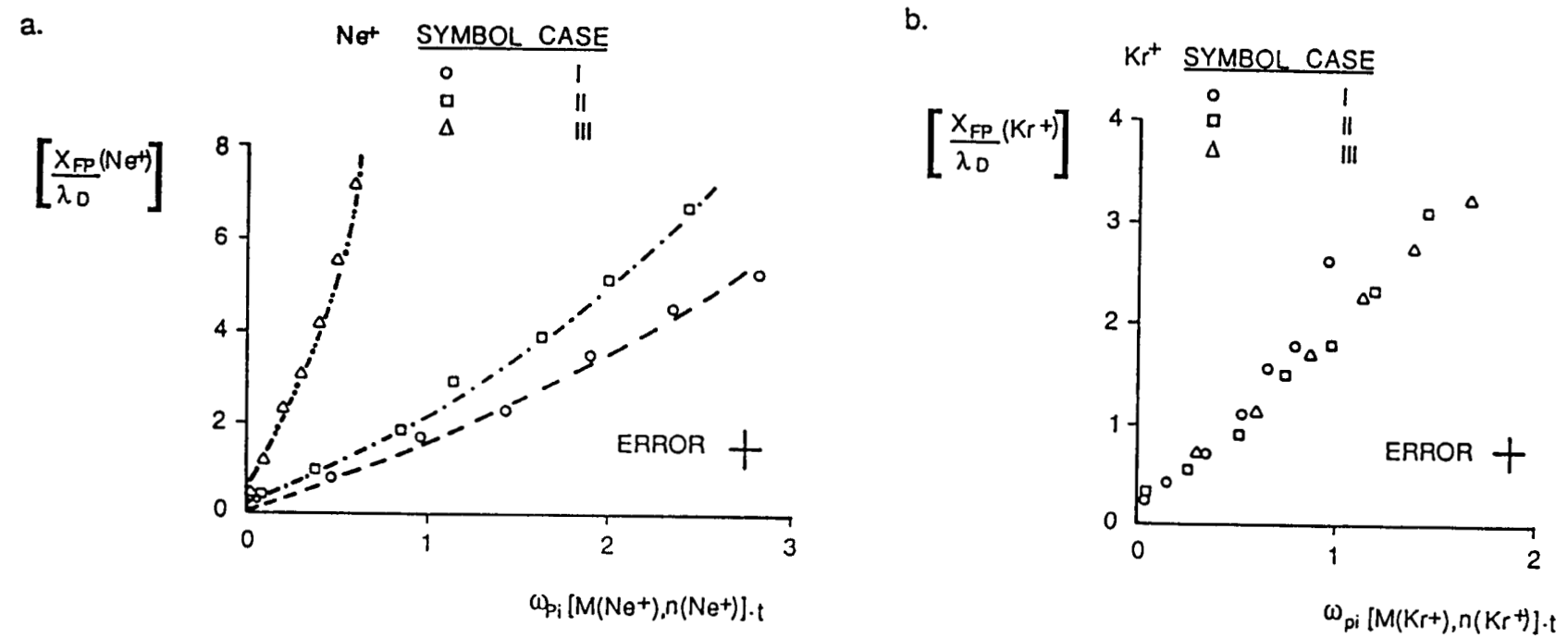

Figure 43. Variation of the foot point location, normalized by the Debye length, with time, normalized by the ion component plasma frequency, for all three experiment cases. (*a*) Ne^+. (*b*) Kr^+. The foot point is the location where the ion current goes to zero. FC measurements are used for Ne^+, while DIFP measurements are used for Kr^+. The Debye length calculation uses the total ambient ion density near plate edge. The time variable is defined as $t \equiv z/V_{flow}$. Each ion component plasma frequency is calculated using the respective ambient ion component density near the plate edge and the ion mass.

properties near the plate edge are used since it is this region from which the foot point particles originate. Therefore, the Debye length is calculated based on the total ion density at the plate location while both plasma frequencies are calculated using the relevant ion constituent density at the plate.

Plotting the data with the normalizations just described allows comparison for each ion species with itself as its relative density is changed in the three cases. As a result, the Ne^+ data clearly separates into three curves in $\omega_{pi}[M_i(Ne^+), n(Ne^+)] \cdot t$ space. In geometric space, however, the separation of Ne^+ is not this dramatic (see Figure 41 for the foot points at $z \simeq 60\,\mathrm{cm}$, which corresponds to the largest $\omega_{pi}[M(Ne^+), n(Ne^+)] \cdot t$ value for each case). The heavier ion, Kr^+, does not measureably separate for this short time scale. Note the difference in the y-axis scale between the Ne^+ and Kr^+ data. In general, the curves for each ion species possess a quadratic shape similar to the curve described by the expansion front profile observed in the single ion plasma experiment (see Figure 16), although the second derivative is not nearly as large. A comment is in order about this comparison between the single ion plasma and the binary ion plasma experiments. The foot point is, by definition, the location where the ion current is zero; i.e., no ions exist. Instrument sensitivity limits an accurate determination of this point. The expansion front observed in the single ion plasma experiment is a feature where ions do exist. Therefore, the same behavior, which results from the action of electric fields, for the foot point and the expansion front should not be expected.

A more accurate indication of acceleration for the leading edge of the expansion can be obtained by examining the vector measurements from the DIFP. The transverse ion velocity in the foot region of the Kr^+ and Ne^+ individual expansions for each case is shown in Figure 44 as a function of time. The velocity measurement is normalized by the ion acoustic speed given by (4.2). The time is normalized in the same manner as in Figure 43. All points satisfied the condition that the

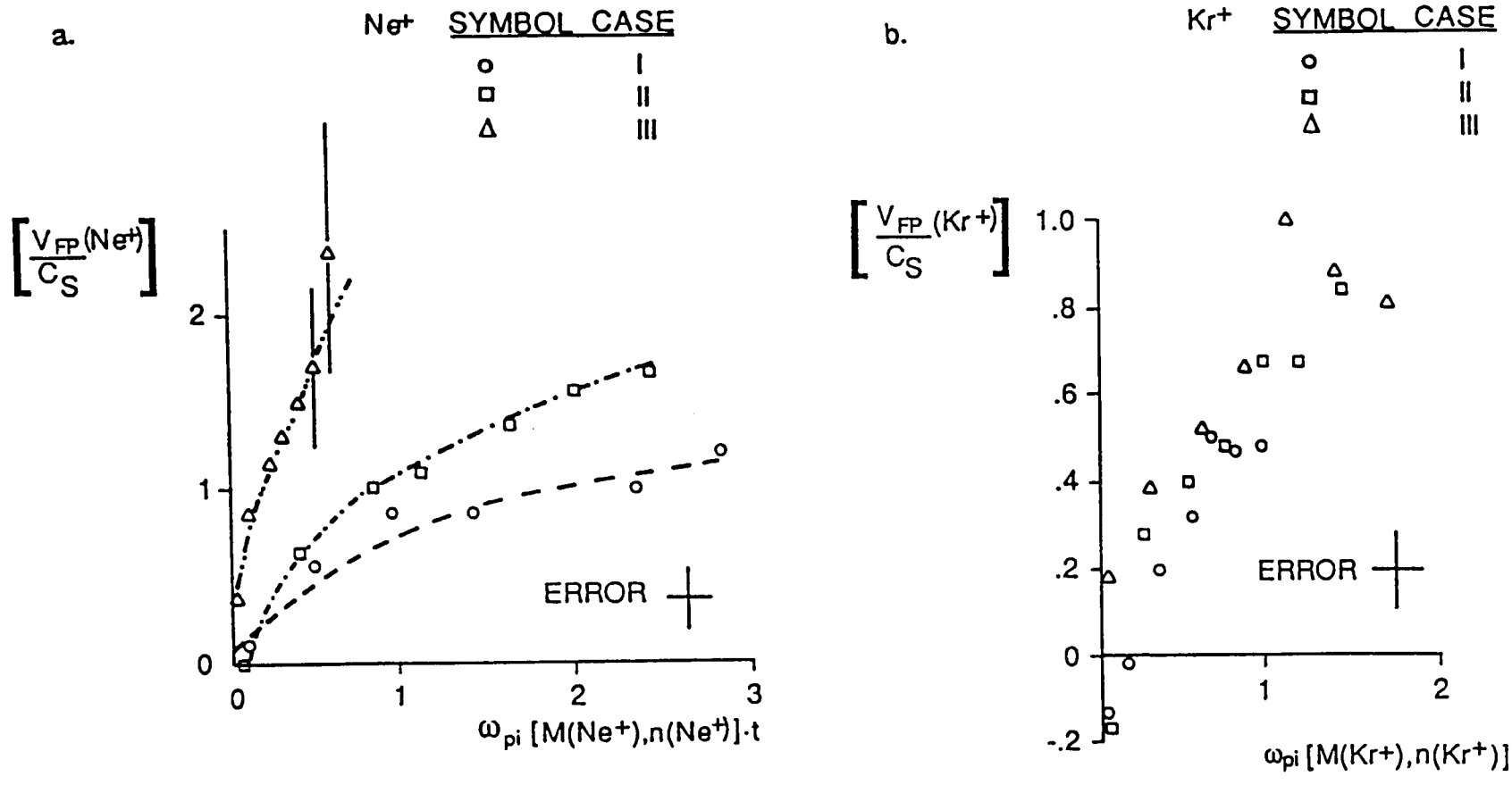

Figure 44. Variation of the transverse ion velocity component in the foot region, normalized by the ion acoustic speed, with time, normalized by the ion plasma frequency, for all experiment cases. (*a*) Ne^+. (*b*) Kr^+. The data points represent velocity measurements when the percentage ion component current density was below the 0.1 level. The ion plasma frequencies are calculated in the manner described in Figure 43. A correction is introduced to the Ne^+ data and is described in the text.

percentage ion current value for each constituent was below the $0.1I_0$ level, with an exception for the Ne^+ data at $z \simeq 40\,\mathrm{cm}$ in case I which is not plotted (see Figures 32, 35, and 38). Only data points at the largest positive x measurement position for each component expansion are considered. These points define the 'foot region' of the expansion, which is crudely analogous to the expansion front in the single ion plasma experiment.

It was observed that the Ne^+ ions, for all cases, have different flow angles as they pass near the plate. To assess any relative differences between the cases in a more accurate way, the transverse velocity values near the plate were all referenced to run 1 of Case II, which had the smallest value of transverse velocity just downstream from the plate edge. The correction obtained for each case was applied to the remaining downstream transverse velocities for that particular case. The result is displayed in Figure 44*a*. Again, the Ne^+ data can be separated into three curves. If the velocity correction is not applied, the separation is wider between the curves for Cases II and III and is about the same between the curves for Cases I and II. The correction has reduced the maximum transverse velocity achieved in each case and serves to account for the small differences existing in Φ_B between the cases (see Tables 3, 4, and 5).

Each curve in Figure 44*a* has a shape similar to expansion front velocity profile in the single ion plasma expansion experiment (see Figure 19). As the Ne^+ percentage is reduced in the plasma, a higher relative acceleration, i.e. a larger slope for the curve, is seen between the cases in $\omega_{pi}[M_i(Ne^+), n(Ne^+)] \cdot t$ space. An increase in the transverse velocity component to speeds above the ion acoustic speed occurs for Cases II and III ($\gamma > 1$), while for case I ($\gamma < 1$), the transverse velocity has just reached the ion acoustic speed. This effect is consistent with the plasma expansion theoretical predictions outlined in Chapter II. When the lighter mass ion is the minor ion constituent in the ambient plasma, the relatively immobile heavier

mass ions initially provide, as the expansion begins, a greater electric field than in the case where the lighter mass ion is the minor constituent. Thus, the response to the electric field should be revealed in higher velocities.

The Kr^+ transverse velocity measurements are displayed in Figure 44*b* with the same time scale as in Figure 43*b*. Note the difference in the Kr^+ velocity scale as compared with the Ne^+ velocity scale. The divergence of the Kr^+ ions at the plate was about the same for all cases so no correction was applied. The Kr^+ data, again, does not separate into different curves. The transverse velocity of the Kr^+ ions just begins reaching the ion acoustic speed at the end of the accessible measurement region.

The Ne^+ data of Figures 43*a* and 44*a* can be normalized in a different way and the case distinction becomes minimal. Reducing the density is easily seen to lower the calculated $\omega_{pi}[n(Ne^+)]$ value. It is interesting to note the difference between the Ne^+ data (separation by case) and the Kr^+ data (no separation by case) when the ion plasma frequency is calculated in the same manner, by using the ambient density of the ion component rather than the total ambient ion density. In some computer simulations, the total ambient ion density is used to calculate the light ion plasma frequency. If this method is followed, the result for the foot point motion is shown in Figure 45*a* while the result for the transverse velocity measurement is shown in Figure 45*b*. The data for the foot point location are now described by one curve. The velocity data show a slight separation between case I ($\gamma < 1$) and Cases II and III ($\gamma > 1$). The reason for the separation is discussed above in connection with Figure 44*a*. If a general separation between cases occurs for this particular normalization, then it must occur for a longer time scale.

To compare the Ne^+ behavior with the Kr^+ behavior in the foot region of their respective expansions, the data in Figures 43 and 44 are plotted with a common $\omega_{pi}[M_i(Kr^+), n(Kr^+)] \cdot t$ axis. That is, the Ne^+ data is placed in the Kr^+

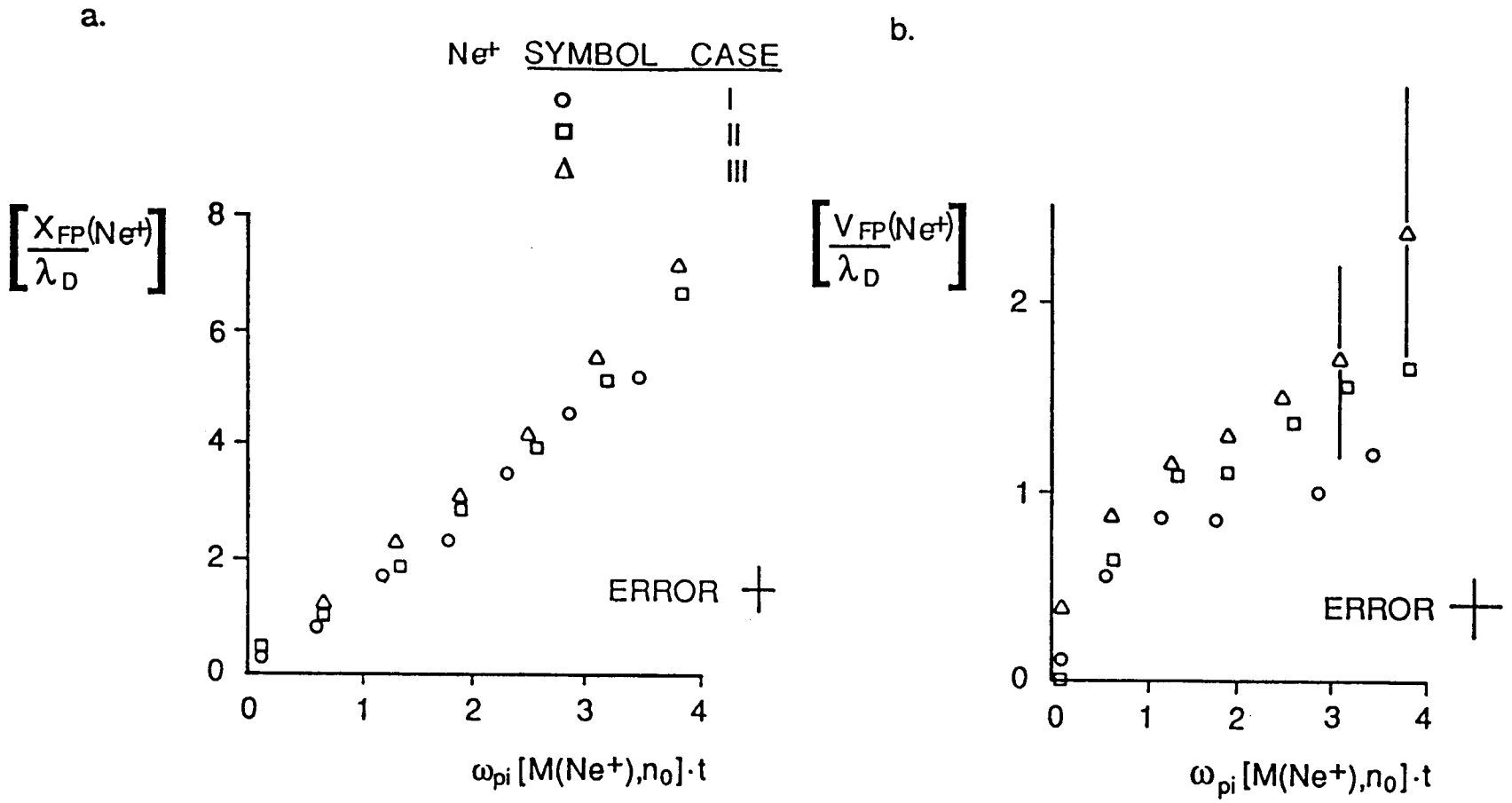

Figure 45. The ordinate values of the Ne^+ data from Figures 43*a* and 44*a* are replotted as a function of normalized time, where the Ne^+ plasma frequency is obtained by using the ambient total ion density near the plate edge. (*a*) Normalized foot point location. (*b*) Normalized transverse velocity component in the foot region.

time scale. The result for the foot point motion is shown in Figure 46*a* while the transverse velocity result is shown in Figure 46*b*. In each panel of the figure, the relative motion of Ne^+ with respect to Kr^+ is seen. Basically, the data for each ion species in all cases is described by one curve. This implies that for this small time scale of the Kr^+ ion, the Ne^+ data, representing the lighter mass ion, does not separate according to the density ratio as it is varied over an order of magnitude.

The best information on the relative acceleration of ion constituents is obtained from Figure 46*b*, where the change in velocity with respect to time can be seen. The dashed lines in Figure 46*b* indicate a linear regression fit to the data points, excluding the smallest $\omega_{pi}[M_i(Kr^+), n(Kr^+)] \cdot t$ values for each case. In addition, the two Ne^+ points with the largest error bars are also excluded. These dashed lines describe in some global sense the acceleration of each ion species at their respective foot regions. The ratio of the slopes is 1.6. This value is less than the mass ratio, 4, the value that would be expected if the particles experience the same electric field. But the electric field will change as a function of spatial position in response to the varying charge distributions of both species; i.e., the electric fields are different in the expansion foot regions of each ion species. Therefore, in the time frame of the Kr^+ ions, the expansion 'foot regions' of both ion species are accelerating, with Ne^+ at a higher rate, due to the potential developed between the ambient plasma and the wake region.

For a closing remark on this chapter, a general comment about the experiment is made. A summary of the results is deferred to the following chapter. No theory exists for detailed comparison with the equivalent small time scale of this experiment ($\omega_{pi}(Ne^+)t < 4$). However, all observations – a rarefaction wave for each ion component, the relative acceleration of Ne^+ to Kr^+, a difference in ion behavior according to γ – can be connected with the physics of the plasma expansion process discussed in Chapter II for the binary ion, single electron temperature plasma.

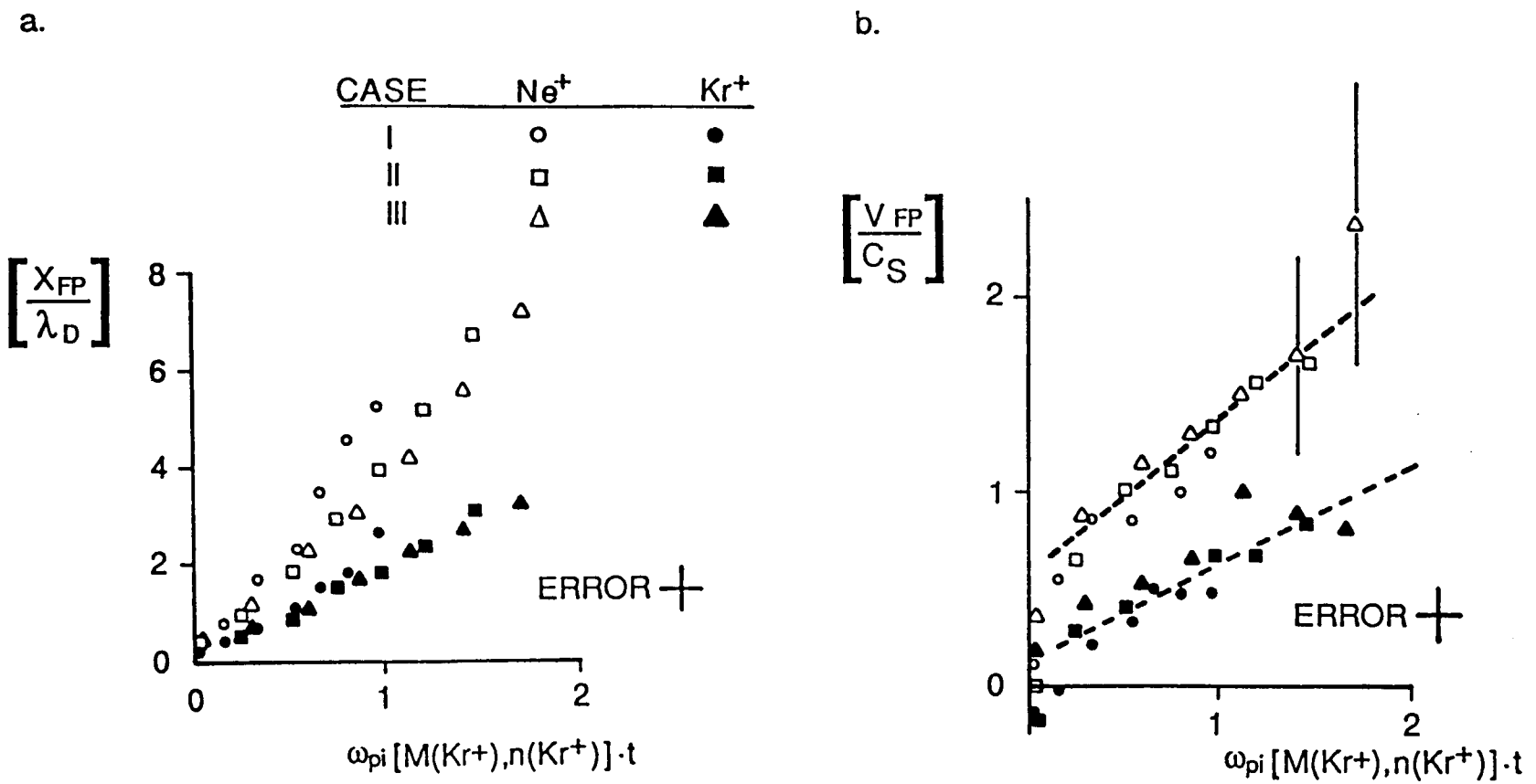

Figure 46. The Ne^+ and Kr^+ data from Figures 43 and 44 are combined on the same graph as a function of normalized time, where the Kr^+ component plasma frequency is calculated in the manner described in Figure 43. (a) Normalized foot point location. (b) Normalized transverse velocity component in the foot region. The dashed lines represent linear least squares fits to the respective data.

CHAPTER V. SUMMARY AND CONCLUSIONS

In the present study, the wake of a non-magnetized test body immersed in a mesosonic, collisionless plasma flow has been examined with single and binary ion plasmas. A large, thin, conducting plate is employed and mounted such that plasma is allowed to flow past only one edge. This object has the effect of simulating, in two dimensions, a body with planar geometry for $R_D \gg 1$. The small thickness of the plate helps maximize the density gradient at the plate edge. Maintaining the potential difference between the plate and the plasma as low as possible minimized sheath deflection of ions and also serves to maximize the density gradient. The subsequent expansion of plasma ions into the wake in response to this density gradient is measured and found to be in accord with some of the predictions from the 'plasma expansion into a vacuum' theories. The comparison of the experimental data with the plasma expansion results is facilitated through the use of the variable $t = z/V_{flow}$. Results from the experiments are summarized in the following sections.

A. Summary of the single ion plasma experimental results

The properties of the single ion (N_2^+) plasma are as follows: $E_d \simeq 18\,\mathrm{eV}$; $n_0 \simeq 1.2 \times 10^5\,\mathrm{cm}^{-3}$; $T_e \simeq 0.27\,\mathrm{eV}$; $\phi_{sp} \simeq -0.5\,\mathrm{volts}$; $\phi_{plate} = 0\,\mathrm{volts}$; and $T_i < 0.1T_e$. The dimensionless parameters for the experiment are then given by:

$$\mathcal{M} \simeq 11.5 \text{ (or } S \simeq 8.1), \quad R_D \gg 1, \quad \Phi_B \simeq +1.8, \quad T > 10\,.$$

Plasma rarefaction wave: A rarefaction wave is observed to initiate at the plate location and to propagate into the ambient background at a speed given by $\sqrt{2}C_S$,

where $C_S = (kT_e/M_i)^{1/2}$. This is consistent with the rarefaction wave predicted from the expansion of plasma from an initially large density gradient. The rarefaction wave is also identical to earlier experimental results where plasma flow over finite-sized bodies of different cross-sectional shapes was examined for various applied potentials [*Stone et al.*, 1978]. (It is noted that the ionic constituent in both the present experiment and in [*Stone et al.*, 1978] was N_2^+.) The rarefaction wave is basic to the plasma disturbances produced by the body, regardless of whether ions enter the near wake by sheath deflection at the body or from acceleration due to polarization electric fields. This is not unexpected, since the response, in general, of a supersonic plasma to a perturbation is the propagation of ion acoustic waves.

Plasma expansion region: The expansion region is observed to possess a general monotonic behavior of decreasing current density from the ambient plasma outside of the wake to the void region behind the plate. The variation of the current density and the vector measurements of the ion flow do not indicate a self-similar behavior, but the plasma is approaching that state with time. This implies that the plasma is accelerating in order to produce an overall quasi-neutral flow. The experiment is limited to equivalent expansion times of $\omega_{pi}t < 4$. The self-similar solution from the quasi-neutral plasma expansion theory applies for the asymptotic state of the expansion. Numerical simulations and other laboratory experimental data have shown that the self-similar state of quasineutral plasma flow is reached in a few ion plasma periods. The present experimental finding is consistent with this result.

It should be noted that the theories assume a constant ambient density. The ambient density in the experiment decreases approximately as $1/r^2$ from the source so that all particles in the expansion region do not originate at the same density level. The effect of the decreasing ambient density is to slow down the expansion because of a reduction in the electron pressure gradient which drives the expansion. This should be kept in mind when making comparisons with theoretical models.

Ion expansion front: This experiment provided extended measurements for the early time ($\omega_{pi}t < 4$) behavior of the ion expansion front. The leading 'front' of the expansion is observed to exist throughout the wake region and is characterized by a large gradient in the local current density. The expansion front accelerates with increasing downstream distance from the plate, which is analogous with increasing expansion time. This motion indicates the action of the polarization electric field. A maximum front velocity of $V_F \simeq 2.4C_S$ is attained, limited by the experimental conditions of ambient plasma density and chamber length. At the farthest downstream location, the width of the front is observed to increase as the front slows down.

Very good quantitative agreement is found for the observed expansion front velocity and position with the empirical formulas of *Katz et al.* [1985]. These formulas describe, within 10 to 15 percent, the numerical simulation results of *Crow et al.* [1975], which used the ion fluid equations and Poisson's equation. The formula for front position is related to the front velocity by $X_F = \int V_F\, dt$. (A small, systematic offset of the data, as compared with the formulas, is noted and attributed to whatever thermal and sheath effects are present. This offset is added as a correction to the formulas.) The agreement of the experimental data with the model implies that the expansion front in this collisionless plasma could be described by the fluid approach. The long range nature of the electrostatic forces and the experimentally imposed fact of no crossing ion streams in the wake would allow it to retain the character of a fluid-like element. The model equations can be used to predict expansion front behavior at longer times, or at distances behind a body for the large $R_D \gg 1$, small Φ_B case, subject to the limitations noted in Appendix D.

The expansion front position is examined at one downstream distance ($z = 22.4\,\text{cm}$ or $\omega_{pi}t = 1.7$) as a function of plate bias. A linear variation is exhibited by

the expansion front position, normalized by Debye length, as a function of normalized body potential over the range $-10 < \Phi_B \leq 20$. This indicates a superposition of effects from the sheath and polarization electric field. Whether the superposition is maintained throughout the wake awaits further study.

B. Summary of the binary ion plasma experimental results

A new plasma source has been developed which has the ability to accelerate dissimilar mass ions to equal flow velocities and the capability to control the ion component density ratio. The source allows access to new dimensions in the parameter space that were previously unavailable for laboratory studies. Specifically, the mass ratio, M_1/M_2 (or Z_2M_1/Z_1M_2), and the ion density component ratio, n_1/n_2, are added to the other parameters of S, R_D, Φ_B, and T that characterize the interaction of a non-magnetized body immersed in a collisionless, plasma flow. Hence, the following results that were obtained from the experiments are new findings.

The general properties of the binary ion (Ne^+, Kr^+) plasma are as follows: $E_d(Ne^+) = 20 - 25\,\text{eV}$ and $E_d(Kr^+) = 85 - 95\,\text{eV}$; $n_0(\text{tot}) = 0.8 - 1.1 \times 10^5\ \text{cm}^{-3}$; $T_e = 0.27 - 0.38\,\text{eV}$; $\phi_{sp} = +(2-3)\,\text{volts}$; $\phi_{plate} = 0\,\text{volts}$; and an estimated $T_i < (0.15 - 0.3)T_e$. The largest difference between the flow velocities for each ion component in any one experiment is less than 8 percent. The ion acoustic speed in a binary ion plasma is given as $C_S = (\beta k T_e/M_H)^{1/2}$, where $\beta = (1-\alpha)Z_H + \alpha\mu Z_L$, $\mu = M_H/M_L$, and $\alpha = Z_L n_L/n_0$. The subscript 'H' designates the heavy ion mass while subscript 'L' designates the light ion mass; i.e., $M_H = M(Kr^+)$, $M_L = M(Ne^+)$. The quantity α represents the light ion percentage in the plasma. In comparing this expression for C_S with the acoustic speed in a single ion plasma, an 'effective' mass of the plasma is noted, $M_{eff} = M_H/\beta$ or $1/M_{eff} = (1-\alpha)/M_H + \alpha/M_L$.

Three cases of ion component density ratio are considered in the experiment: Case I $- n(Ne^+)/n(Kr^+) \simeq 2$; Case II $- n(Ne^+)/n(Kr^+) \simeq 0.5$; and Case III $- n(Ne^+)/n(Kr^+) < 0.2$. (See Chapter IV.C for the specific plasma properties for each case.) The dimensionless parameters are then given by

$$M_H/M_L = 4.15; \quad \mathcal{M} \simeq 14 - 20, \quad R_D \gg 1, \quad \Phi_B \simeq -(6-8), \quad T \simeq 3.5 - 6.5\,.$$

General results from all three cases are now presented.

Plasma rarefaction wave: A rarefaction wave, as determined by the total ion current density, is observed to initiate at the plate location and to propagate into the ambient background at a speed given by C_S, whose formula is noted above for the binary ion case. When the plasma source is operated in the single ion species mode and N_2^+ is the working gas, a rarefaction wave is observed and is identical to the rarefaction wave in the single ion plasma experiment; i.e., the wave speed is $\sqrt{2}C_S$. This difference in rarefaction wave speed may be due to different heat capacities between the inert gases and the molecular gases.

A rarefaction wave for each ion component is also observed. Spatial resolution of the DIFP measurements is not sufficient to determine a wave speed for each component. However, the general behavior indicates that the ratio for the component wave speeds is approximately 2. This value is the ratio of the acoustic speeds for each individual component; i.e., $C_S(Ne^+)/C_S(Kr^+) = 2$. The observation of different speeds for each component is consistent with plasma expansion theory which includes charge separation or ion pressure (temperature) effects.

Plasma expansion region: The ion behavior in the expansion region is observed to change as a function of the ion density component ratio. In Case I, the lighter mass Ne^+ is the dominant ionic species in the ambient plasma and remains the dominant species in the expansion region. The Ne^+ is also observed to move relative to the Kr^+. The current density for each ion component monotonically decreases in the expansion region. In Cases II and III, Ne^+ is the minor ion species in the

ambient plasma but accelerates relative to the Kr^+, overtakes the Kr^+, and then becomes the only ion species expanding. The Ne^+ begins crossing through the Kr^+ as close as 10 cm to the plate.

At the farthest downstream position from the plate, or alternatively, at the longest time [$\omega_{pi}(Ne^+)t|_{max} < 3$], a plateau-like region develops for Ne^+ in Cases II and III. That is, there is a range of positions over which the Ne^+ current density varies slowly. In this high Mach number plasma, the normalized density is roughly indicated by the normalized current density. The normalized current density for Ne^+ shows the plateau-like region to be approximately the same for both cases. The lower position of the plateau-like region begins after the normalized Kr^+ current has fallen below the $0.5I_0$ level. At the position where the Kr^+ current goes to zero, the Ne^+ plateau-like region ends and the Ne^+-only expansion proceeds. The observation of the plateau-like feature existing in Cases II and III is consistent with the plasma expansion theory prediction of the development of a region where the light ion properties are constant or change slowly. The theory applies for the longer times. The positive space potential in the ambient plasma may increase the polarization electric field, giving the appearance of a longer expansion time.

Leading edge of the expansion: The experiment provides measurements for the early time behavior of the leading ions in the expansion, $\omega_{pi}(\%Ne^+)t \leq 2.8$ and $\omega_{pi}(\%Kr^+)t \leq 1.7$. An expansion front is not observed in the binary ion plasma case. The presence of the second ion species does not result in the disappearance of the front because it is not observed even in the single ion mode operation of the plasma source. Differences in the electron environment and the transverse ion temperature between the plasma sources of the single ion and the binary ion plasma experiments are possible reasons.

Acceleration of ions in the leading edge of each component expansion is observed by the vector measurements of the ion flow. A correction is applied to the

Ne^+ based on the different divergences occurring at the plate location between the three cases. This correction is thought to yield a more accurate description of the Ne^+ expansion. The highest transverse component of velocity for Ne^+ is approximately $2C_S$, while Kr^+ barely reaches the C_S level. Over the Kr^+ time scale for the expansion, the three cases for Kr^+, as well as for $Ne+$, can basically be described by one curve. Ne^+ is seen to accelerate at a rate approximately 1.6 times the rate for Kr^+.

The present laboratory experiments indicate that the plasma expansion process is the dominant filling mechanism of the near wakes of bodies in the supersonic, sub-Alfvenic flow regime with $R_D \gg 1$ and a relatively small potential difference between the body and the plasma. This is a case of general interest to space plasma physics, which includes the specific examples of the motion of Io and Ganymede through the Jovian magnetosphere, the motion of Titan through the Saturnian magnetosphere, and the motion of spacecraft through the terrestrial ionosphere. The magnitude of the effects from the expansion process depends, among other things, on the strength of the initial density gradient. As the density gradient is decreased, comparatively less acceleration of the ions occurs for a given time and spatial extent of the expansion. In this case, longer times are required to reach a quasi-neutral, self-similar flow. A body with a 'non-zero' dimension in the flow direction (i.e., not a thin plate) together with an atmosphere (neutral or ionized) would serve to reduce the density gradient near the 'edge' of the body. However, three-dimensional aspects of electron expansion into the near wake and the formation of a potential barrier for electrons (an attractive well for ions) may offset the lower acceleration resulting from a reduced density gradient.

C. Suggestions for future studies

1. Single ion plasma flow-body interaction. Several additional points should be examined in future laboratory studies: (1) The rarefaction waves of the inert gases need to be investigated along with additional available molecular gases. The binary ion plasma experiment, which used Ne^+ and Kr^+ as the working gases, raised the issue of a difference in the rarefaction wave speed between the monoatomic and molecular gases due to different heat capacities. This information will be useful in interpreting data from future space plasma physics investigations on the space shuttle and space station; e.g., the Tethered Satellite System and Space Plasma Lab experiments. (2) The wake of the plate should be examined for a range of Mach numbers to further investigate $z/\mathcal{M}$ scaling. This is essentially implied by the use of the $t(\equiv z/V_{flow})$ variable. (3) The expansion region needs to be mapped for different Φ_B to determine interplay between the sheath and polarization electric fields. (4) The possibility of oscillations or noise occurring in the wake, perhaps in association with density gradients, needs to be investigated. (5) The wake filling in the presence of various magnetic field strengths and orientations should also be examined.

2. Binary ion plasma flow-body interaction.

Before additional experiments are carried out, however, certain aspects of the beam need to be improved. The large gradient in the freestream transverse ion current profiles needs to be reduced. Elimination of the B_{MIRROR} and B_{EXIT} magnetic fields, or drastically reducing their values, may accomplish this. However, the plasma density will be reduced. The addition of some emissive filaments and conducting rings near the mirror, along with improvements in the ion optics in order to extract more ions from the individual sources are examples of things that can be done to increase the overall plasma stream density in the chamber. Reducing

the value or eliminating B_{MIRROR} will also remove the extra, undesirable Ne^+ stream currently present. Additional probes, such as an instrument with a highly collimated entrance aperature and a Langmuir probe of the emissive wire type, are needed to gain a better idea of the ion temperatue value and of the plasma space potential, respectively.

Once improvement of the plasma beam has been completed, the parametric studies of the wake previously accomplished in the single ion plasmas can be repeated for the binary ion plasma. The complexity of the wake structure, existing for certain parameter values, can be expected to increase. Vector measurements of the ion flow will be imperative in order to diagnose the interaction, as already established by the present experimental study. Two stream instabilities can be studied by establishing a speed difference between the ions in the flow. The differential motion could be created by a sufficiently negative potential on the body or created in the freestream by appropriate adjustments of the plasma source. This new source allows investigation of phenomena and processes that naturally occur in space plasma physics, particularly in planetary ionospheres and magnetospheres where multiple ion constituents are known to exist.

APPENDIX A. THE KINETIC AND FLUID EQUATIONS FOR PLASMA EXPANSION INTO A VACUUM

The phenomena and processes of plasma expansion into vacuum or into a more tenuous plasma have been investigated through both kinetic and fluid treatments. The basic equations considered in those approaches for describing the ion behavior during the expansion are presented.

1. Kinetic equations

The basic one dimensional kinetic equation treated in the *Gurevich et al.* approach (e.g., *Gurevich et al.* [1966]) is derived. A singly-ionized plasma described by a Vlasov - Poisson system for the ion distribution function f (in Gaussian units) is given by:

$$\frac{\partial f}{\partial t} + v\frac{\partial f}{\partial x} - \frac{e}{M_i}\frac{\partial \phi}{\partial x}\frac{\partial f}{\partial v} = 0 \qquad (A.1)$$

and

$$\frac{\partial^2 \phi}{\partial x^2} = -4\pi e(n_i - n_e)\,, \qquad (A.2)$$

where M_i is the ionic mass, ϕ is electrostatic potential ($E = -\partial\phi/\partial x$), and

$$n_i = \int_{-\infty}^{\infty} f\, dv. \qquad (A.3)$$

Assuming quasi-neutrality, or that the scale length for potential variation is much greater than a Debye length, (A.2) can be reduced to:

$$n_i = n_e \qquad (A.4)$$

The electrons are treated as a massless, isothermal fluid resulting in a density governed by the Boltzmann relation:

$$n_e = n_0 \exp(e\phi/kT_e), \tag{A.5}$$

where n_0 is the ambient electron density. Hence

$$e\phi = kT_e \ln(n_i/n_0). \tag{A.6}$$

Substituting (A.6) into (A.1) results in

$$\frac{\partial f}{\partial t} + v\frac{\partial f}{\partial x} - \frac{\partial f}{\partial v}\frac{kT_e}{M_i}\frac{\partial}{\partial x}\left(\ln \int_{-\infty}^{\infty} n_0^{-1} f\, dv\right) = 0. \tag{A.7}$$

The ion motion can be treated in the self-similar approach by rewriting the equations in terms of a variable x/t, i.e. $f = f(x/t, v)$. Note that the element of 'characteristic length' is eliminated.

Defining new variables

$$\tau = \frac{x}{t}\left(\frac{M_i}{2kT_e}\right)^{1/2} \qquad u = v\left(\frac{M_i}{2kT_e}\right)^{1/2} \qquad g = \left(\frac{2\pi kT_i}{M_i}\right)^{1/2} f n_0^{-1} \tag{A.8}$$

the equation

$$(u-\tau)\frac{\partial g}{\partial \tau} - \frac{1}{2}\frac{\partial g}{\partial u}\frac{d}{d\tau}\left(\ln \int_{-\infty}^{\infty} g\,\frac{du}{\sqrt{\pi/T}}\right) = 0 \tag{A.9}$$

is obtained for the non-dimensional ion distribution function g. Note that (A.9) does not impose any requirement on f. (Note that ξ, given in Chapter II, and τ satisfy: $\tau = \xi/\sqrt{2}$.)

Equation (A.9) can also be written in the form:

$$(u-\tau)\frac{\partial g}{\partial \tau} - \frac{1}{2}\frac{\partial g}{\partial u}\frac{d\Phi_N}{d\tau} = 0 \tag{A.10}$$

$$\Phi_N = \frac{e\phi}{kT_e} = \ln\left(\frac{n_i}{n_0}\right) \qquad \frac{n_i}{n_0} = \int_{-\infty}^{\infty} g\frac{du}{\sqrt{\pi/T}} \qquad T = \frac{T_e}{T_i}$$

Equation (A.9) or (A.10) is the basic equation treated in *Gurevich et al.* [1966, 1968, 1973*a*] and *Gurevich and Pitaevsky* [1975].

For $t \leq 0$, $x \to -\infty$ the plasma is undisturbed (ambient), while for $x \to +\infty$ the plasma vanishes. If it is assumed that in the undisturbed plasma the ions obey a Maxwellian distribution, then the boundary conditions of the 'basic equation' (A.9 or A.10) are: $\tau \to -\infty$, $g \to \exp(-Tu^2)$ and $\tau \to +\infty$, $g \to 0$.

2. Fluid equations

For large $\tau > 0$ (which corresponds to large x) the ions are strongly accelerated; hence, their thermal motion can be neglected. In this case, one can treat the plasma using the fluid continuity and momentum equations

$$\frac{\partial n_i}{\partial t} + \frac{\partial}{\partial x}(n_i V_i) = 0 \tag{A.11}$$

$$M_i\left(\frac{\partial V_i}{\partial t} + V_i\frac{\partial V_i}{\partial x}\right) = -Z_i\, e\left(\frac{\partial \phi}{\partial x}\right) \tag{A.12}$$

together with the Boltzmann relation (A.5). If quasi-neutrality is not assumed, then Poisson's equation (A.2) must be used.

APPENDIX B. PLASMA EXPANSION FOR TWO ELECTRON TEMPERATURE PLASMAS

The expansion of plasma with multiple electron temperatures is of interest in some solar system situations. For example, in the polar regions of the earth, various energetic electron populations can exist which enhance the outflow of plasma from the ionosphere (the polar wind) [e.g., *Winningham and Heikkila*, 1974; *Barakat and Schunk*, 1984]. Also, in the solar wind, several types of energetic electron populations can exist with a variety of effects on the expanding plasma [e.g., *Feldman et al.*, 1978; *Pilipp et al.*, 1987*a*, *b*, *c*]. The following sections give brief descriptions of plasma expansion for two electron temperatures in single ion and binary ion plasmas.

1. Single ion and two electron temperature plasma

For the expansion of a plasma consisting of one ionic constituent and two electron temperatures, consider the case where the ambient density of the colder electron population (n_{e0}^C, T_e^C) be much greater than the ambient density of the hot electron population (n_{e0}^H, T_e^H). During the early stages of the expansion, the ion acceleration is determined by the cold electron component, because $n_e^C > n_e^H$. The ion velocity V_i is given by

$$V_i \simeq C_S^C(\xi_C + 1), \tag{B.1}$$

where $\xi_C = x/C_S^C t$ and $C_S^C = (Z_i k T_e^C/M_i)^{1/2}$. When $n_e^H > n_e^C$, the hot electron component controls the ion motion according to

$$V_i \simeq C_S^H(\xi_H + 1), \tag{B.2}$$

where $\xi_H = x/C_S^H t$ and $C_S^H = (Z_i k T_e^H / M_i)^{1/2}$. The energy spectra of the ions has then two peaks, one proportional to T_e^C and the other proportional to T_e^H. The rarefaction wave will propagate at the acoustic speed determined by the cold electron component; i.e., C_S^C.

Bezzerides et al. [1978], solving the quasi-neutral fluid equations for two superimposed isothermal electron fluids, determined that there should be a 'rarefaction shock' in an intermediate region in the flow, i.e. between the regions dominated by the respective electron temperature components. The necessary condition for the shock to occur is that

$$T_e^H / T_e^C \geq 5 + \sqrt{24}. \qquad (B.3)$$

In an experiment for a supersonic plasma flow of this type past a body, *Diebold et al.* [1987*b*] found evidence of a rarefaction shock in the wake when the condition (B.3) was satisfied in the ambient plasma.

2. Binary ion and two electron temperature plasma

Finally, consider the expansion of a plasma composed of two ionic constituents $(Z_1, M_1; Z_2, M_2)$ and two electron temperature populations (T_e^C, T_e^H) where the ambient cold electron population (n_{e0}^C) is much greater than the hot electron population (n_{e0}^H). Further, let the ions obey the conditions $Z_1 n_{10}^i > Z_2 n_{20}^i$ and $\gamma > 1$ [*Wickens and Allen*, 1981]. (Recall that $\gamma = Z_2 M_1 / Z_1 M_2$.) As the expansion begins, the initial electric field is predominantly determined by the cold electrons and the ionic constituent with the greater charge density; in this case, $Z_1 n_1^i$. Therefore, the larger Z/M constituent, i.e. Z_2/M_2, is preferentially accelerated. As the expansion continues, there is a spatial region where many of the cold electrons are reflected from the self consistent electric field set up by the hot electrons. In this spatial region, the charge density of the Z_2/M_2 constituent begins to exceed the

charge density of the Z_1/M_1 constituent. The remainder of the expansion is then determined by the hot electron component and the Z_2/M_2 constituent. The energy spectra of each ion constituent has then two peaks, one proportional to T_e^C and the other proportional to T_e^H. The rarefaction wave moves toward the ambient plasma at a speed determined by the cold electron temperature and the smaller Z/M constituent; i.e., $(Z_1 k T_e^C/M_1)^{1/2}$.

APPENDIX C. DIAGNOSTIC INSTRUMENTS AND ANALYSIS TECHNIQUES

1. Faraday cup

The ion current density of the plasma beam is measured by a Faraday cup, shown in Figure 47. The probe consists of a collector and two grids. The outer grid, along with the probe casing, is maintained at ground potential while the inner grid is maintained at a negative potential (-20 volts) to repel electrons. The collector is of a deep well cup-shaped construction in order to minimize loss of secondary electrons emitted from the collecter surface. The collected ion current is related to the ion density by

$$I = \kappa Z_i e n_i V_{flow} A, \qquad (C.1)$$

where κ = total grid transmission factor, $Z_i e$ = charge per ion, n_i = ion number density, V_{flow} = ion-stream velocity, and A = aperature area of probe.

2. Langmuir probe

The Langmuir probe, shown in Figure 48a, is a small, segmented cylindrical rod. The addition of the guard is to eliminate fringing fields. The current collected, in response to an applied ramp voltage, was passed through a 1 mega-ohm resistor. The voltage drop across the resistor is measured by a differential amplifier and the amplifier output recorded versus the applied ramp voltage. In the single ion plasma experiment, the probe trace was recorded on a X-Y plotter. In the binary

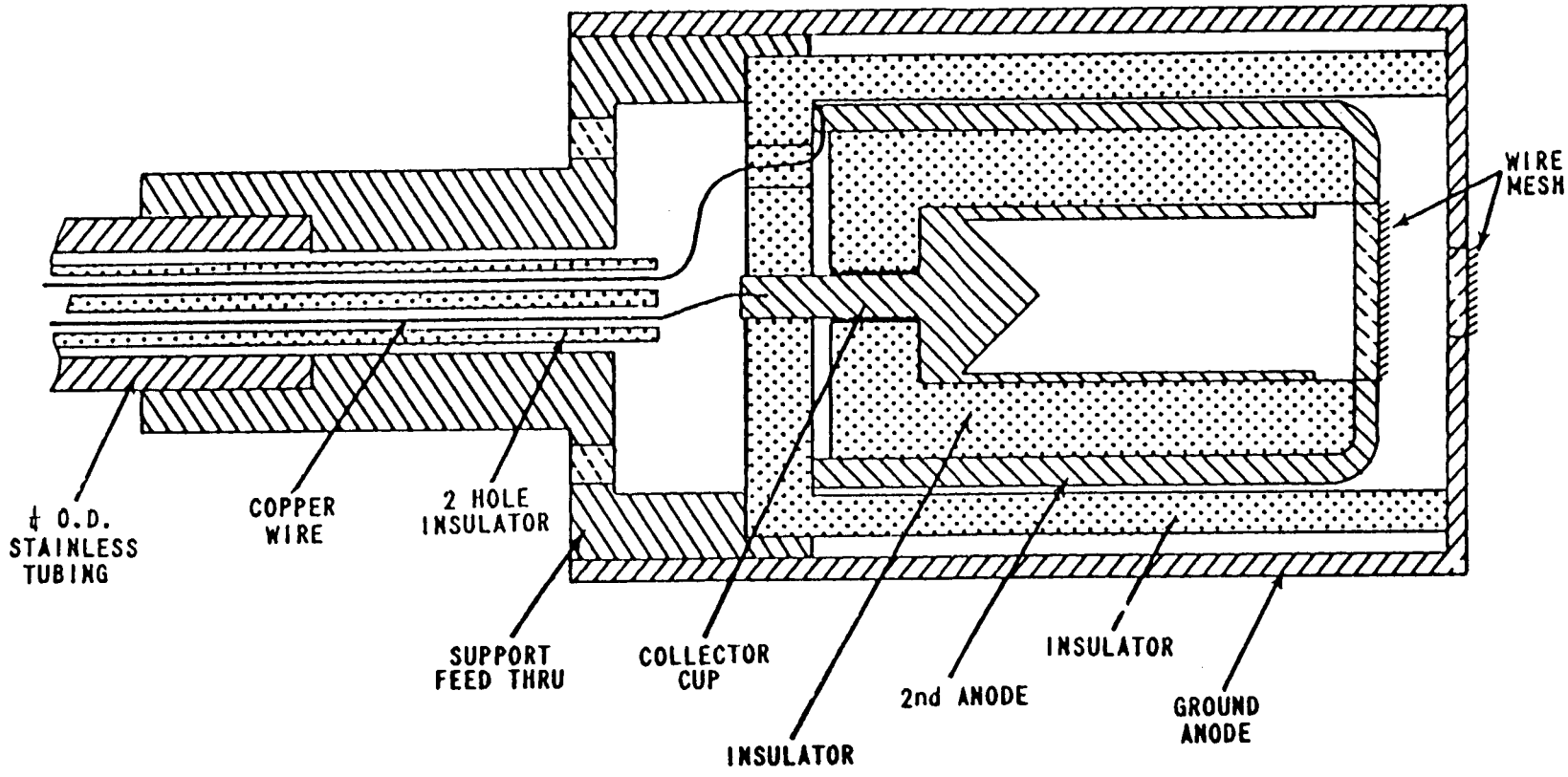

Figure 47. Schematic of Faraday cup assembly.

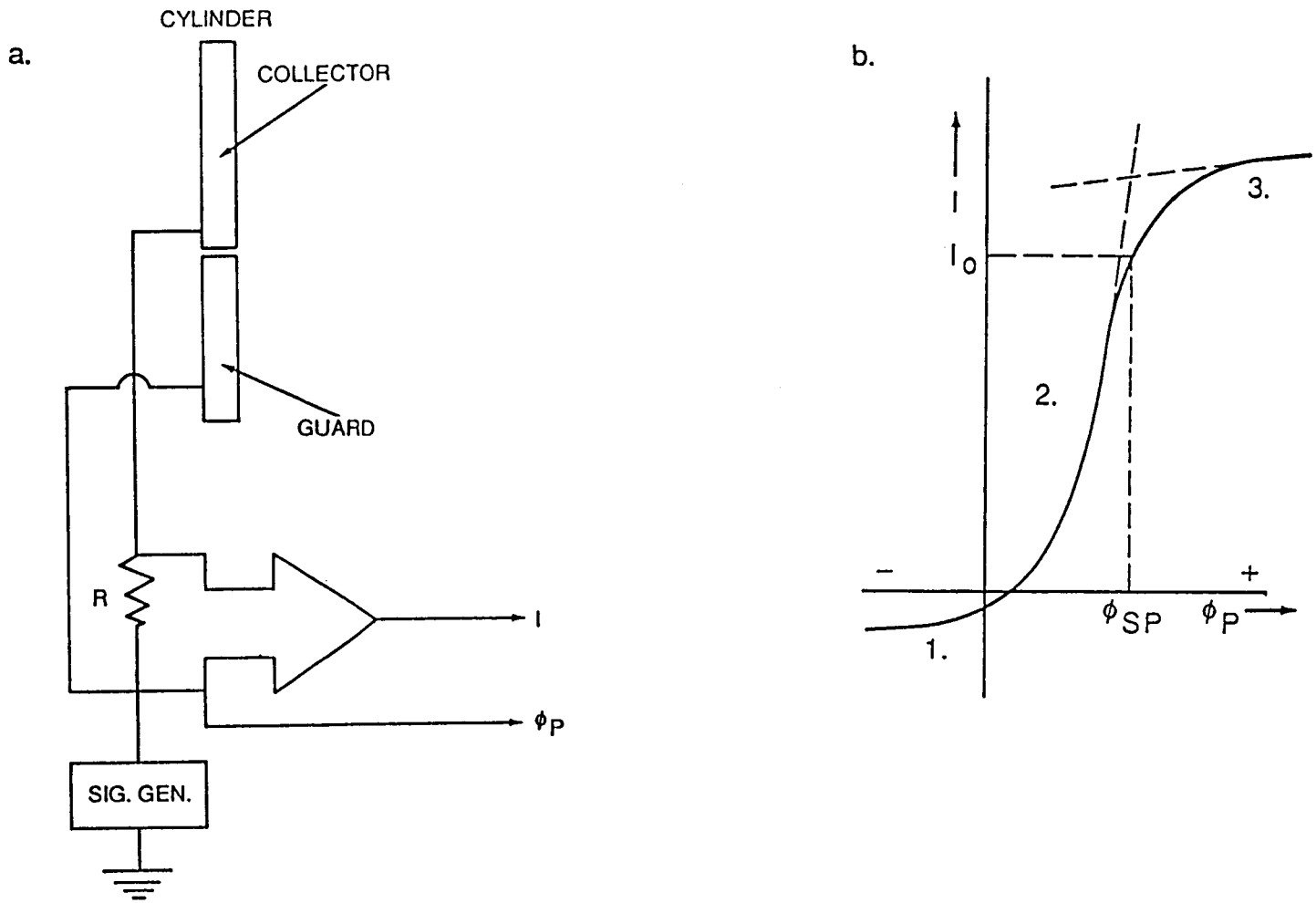

Figure 48. (*a*) Cylindrical Langmuir probe and circuit. (*b*) Instrument response curve.

ion plasma experiment, the probe trace was recorded by computer (MASSCOMP 560) acquisition through an analog-to-digital converter.

The probe characteristic is illustrated in Figure 48*b*. (Note that the electron current is plotted as positive.) In region 1 of the curve, electrons are repelled and only ions are collected (ion saturation). As the probe potential is swept more positive, electrons are collected. If the electron distribution is Maxwellian, the probe response in region 2 is given by

$$I_e = I_{e_0} \exp[e(\phi_p - \phi_{sp})/kT_e], \qquad (C.2)$$

where ϕ_p = applied probe potential, ϕ_{sp} = plasma space potential, and I_{e_0} = electron current at $\phi_p = \phi_{sp}$. When the probe potential is greater than ϕ_{sp}, in region 3, electrons of all energies are collected. This is the electron saturation region. Subtracting the ion saturation current from the probe characteristic and plotting the logarithm of this difference versus ϕ_p will yield a linear curve (for a Maxwellian distribution) whose slope is proportional to T_e [see (C.2)]. The linearity of this plot for the experiment data extended over one to one-and-a-half orders of magnitude in current. Deviation from linearity defines the space potential point. In practice, for laboratory plasmas, the electron saturation current is not very constant and the 'break point' on the semilog plot is not well defined. Emissive probes can provide a much more accurate determination of ϕ_{sp}. However, a probe of this type was not availiable for use in these experiments. The theory, applications, and limitations of a variety of Langmuir probes types have been recently discussed in *Hershkowitz* [1987].

Two different cylindrical probes of approximately the same dimensions were used in the experiments. For the single ion plasma case, the probe electronics were external to the vacuum chamber. This allowed biasing the probe at a large negative voltage (-750 volts) for extended periods of time to obtain ion bombardment cleaning of the surface. In the binary ion plasma case, the probe electronics were inside

the vacuum chamber and were configured such that large probe biases were not possible. Possible surface contamination in this case would lead to an overestimate for both the electron temperature and the space potential.

3. Differential ion flux probe (DIFP)

The DIFP was developed to diagnose the complex ion behavior occurring in the wake of a body immersed in a flowing plasma; e.g., multiple streams converging on the wake axis. The technique to discriminate in direction among several ion streams; i.e., the differential flux vector, is discussed in detail in *Stone* [1977, 1981*a*]. In this section, only the basic principle of the DIFP and its operation in the two experiments described in Chapters III and IV will be discussed.

The DIFP consists of two sections: an electrostatic deflection section and a planar retarding potential analyzer (RPA) section. A cross-sectional schematic is presented in Figure 49. Two deflection plates are located behind an entrance slit. These plates are swept with a voltage (ϕ_d), of the same magnitude but opposite in polarity, to provide a fringing electric field which can deflect incident particles through an exit slit. The ramping of the deflection voltage effectively sweeps a small angular window, $\Delta\theta$, through a range $-\Omega$ to $+\Omega$. For the DIFP used in the experiment, $\Delta\theta = 5°$ and $\Omega = \pm 50°$. For incoming particles with an energy (E_i) and an angle (θ) in the analysis plane depicted in Figure 49, a particular plate voltage (ϕ_d^*) will maximize the output through the exit slit. This is very similar to the operation of a cathode ray tube. Particles entering the RPA section, at some small angle (ψ) relative to the grid normal, are then analyzed in the standard way by applying a ramp voltage (ϕ_r) to a grid. The screen grid is held at -20 volts to repel electrons. The value of ψ is just a few degrees even at large incident angles ($\theta \simeq 50°$), therefore allowing an accurate determination of E_i even when θ is

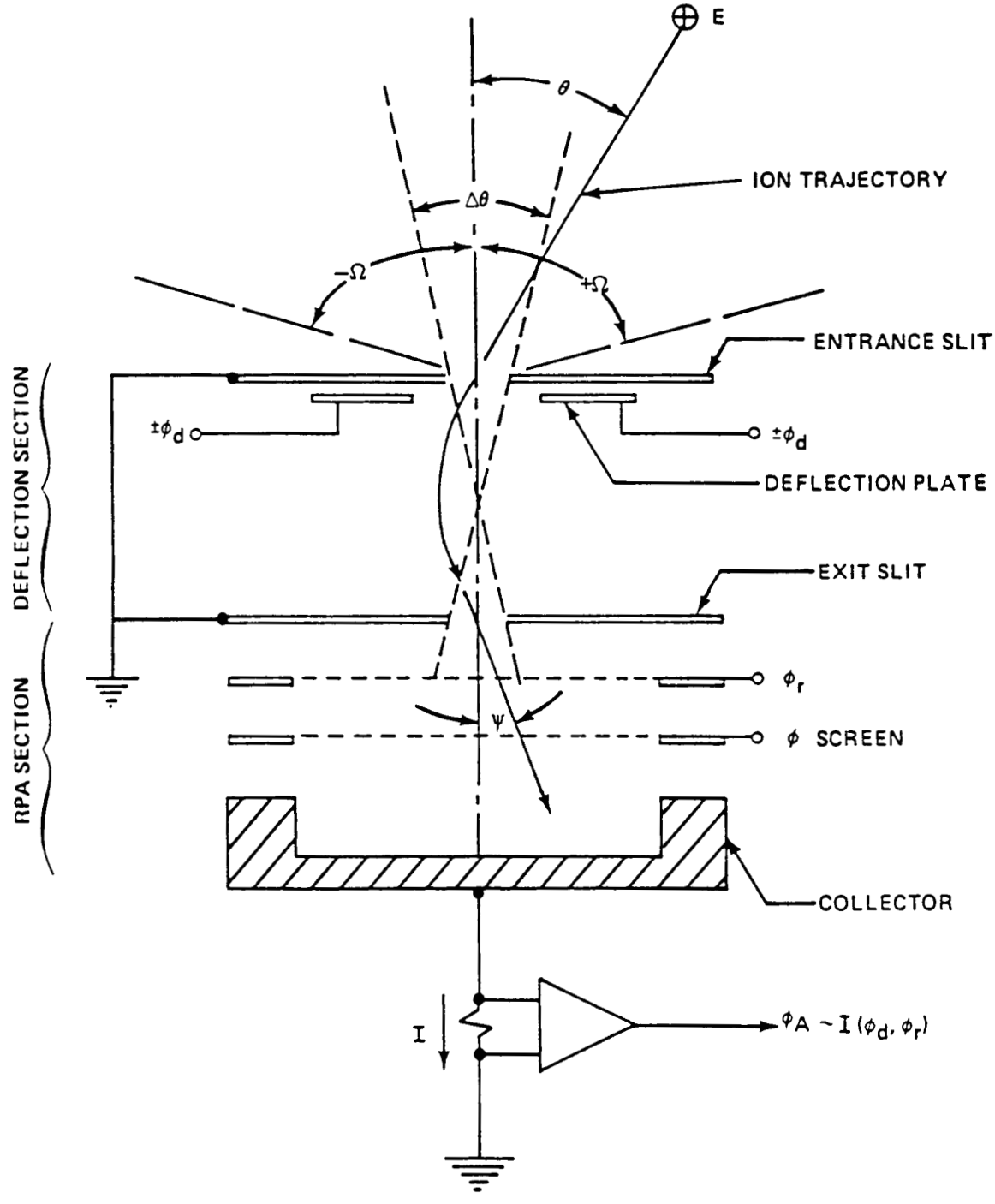

Figure 49. Cross-sectional view of the Differential Ion Flux Probe (DIFP) in the instrument's measurement plane. This view is perpendicular to the deflection plate system. The figure is after *Stone* [1977].

large. The deflection voltage, ϕ_d, and the retarding voltage, ϕ_r, provide two known variables that can be used to calculate the two unknown characteristics of the ions, θ and E_i. Typical probe responses as functions of the two ramp voltages for the two types of plasmas used in the experiments are shown in the following sections C.3.a and C.3.b.

The DIFP response in the deflection mode (ϕ_d swept while $\phi_r = 0$) is linear in energy. That is to say, for a given angle, θ, increasing the ion energy, E_i, results in a linear increase in ϕ_d^*, the deflection voltage where the collected current is maximized. Thus, the ratio, ϕ_d^*/E_i, will only be a function of the angle θ. Calibration information yields the following instrument response function:

$$\frac{\phi_d^*}{E_i} = 1.66 \sin(1.7\theta). \qquad (C.3)$$

The drift energy E_i is determined from analysis of the RPA trace obtained by holding $\phi_d = \phi_d^*$ and sweeping ϕ_r. The instrument is not interactive so that the value ϕ_d^* must be determined by visual inspection of the X-Y plotter deflection trace or output from the electrometer or computer graph display. If the incident ion stream is assumed to be a drifting Maxwellian, then integrating this distribution to estimate the current response yields [*Whipple*, 1959]:

$$I(\phi_d^*, \phi_r) = \frac{1}{2} I_0 \left[1 + \mathrm{erf}(\eta) + \sqrt{(T_{i_\parallel}/\pi E_i)} \exp(-\eta^2)\right], \qquad (C.4)$$

where I_0 is given by (C.1), $T_{i_\parallel}$ = ion temperature parallel to the flow in eV, $\eta = (1/\sqrt{T_{i_\parallel}})[\sqrt{E_i} - \sqrt{\phi_r}]$, and $V_{flow} \equiv (2eE_i/M_i)^{1/2}$. $T_{i_\parallel}$ represents the spread in energy along the flow direction due to potential fluctuations and gradients from the source acceleration region to the measurement point.

The DIFP sensitivity varies with angle due to geometric effects of the collimator system. The ion current at ϕ_d^*, therefore, decreases with increasing angle θ. Calibration information yields the following angular sensitivity equation:

$$I(\phi_d^*, \theta) = I(\theta = 0) \exp\left[-9.86 \times 10^{-5}|\theta| - 1.92 \times 10^{-3}|\theta|^2 - 1.19 \times 10^{-5}|\theta|^3\right], \quad (C.5)$$

where $I(\theta = 0)$ = the value of the current if the ion stream is incident along the probe normal.

a. Single ion plasma experiment. A typical DIFP response in the freestream (ambient) of the single ion (N_2^+) plasma experiment is shown in Figure 50*a* (deflection mode) and Figure 50*b* (RPA mode). The data shown has been digitized from an X-Y plotter trace. The normalized current is plotted in both curves. The deflection curve data is fit to the following Gaussian function:

$$I(\phi_d, \phi_r = 0) = I_0 \exp[-(\phi_d - \phi_d^*)^2/2\sigma^2], \qquad (C.6)$$

where I_0 = the curve amplitude and σ = the standard deviation. The half width at half maximum ($\equiv \delta$) is given by 1.18σ. The value of δ depends on several factors: the size of the angular window, any spread in energy along and transverse to the flow direction, and the particular value of the energy and incident angle. A quantitative analysis of the dependence of δ on each of these factors is not possible with the present calibration information. The parameters from the fit of (C.6) to the deflection data yields $\phi_d^* = 3.3$ volts and $\delta = 1.0$ volt. The curve fit of (C.4) to the RPA data in Figure 50*b* yields $E_i = 18.5\,\text{eV}$ and $T_{i_\parallel} = 0.033\,\text{eV} = 380\,\text{K}$. The angle of this example stream relative to the instrument normal, calculated from (C.3), is $\theta = 3.6°$. Since the probe normal of the DIFP was aligned with the chamber axis, the velocity components parallel and perpendicular to the chamber axis in the measurement plane are readily found from the value of the angle θ.

b. Binary ion plasma experiment. The DIFP is operated in the same manner as in the single ion plasma experiment, but with additional ϕ_d and ϕ_r sweeps at every spatial location since there are now two ion populations to measure. As described in Chapter IV, each ion is accelerated to the same flow velocity, V_{flow}. The two masses used in the experiment are neon (Ne^+) and krypton (Kr^+). The mass ratio $M_i(Kr^+)/M_i(Ne^+) = 4.15$; therefore, the drift energy ratio is the same factor. (The drift energies of the ions during freestream measurements and during the

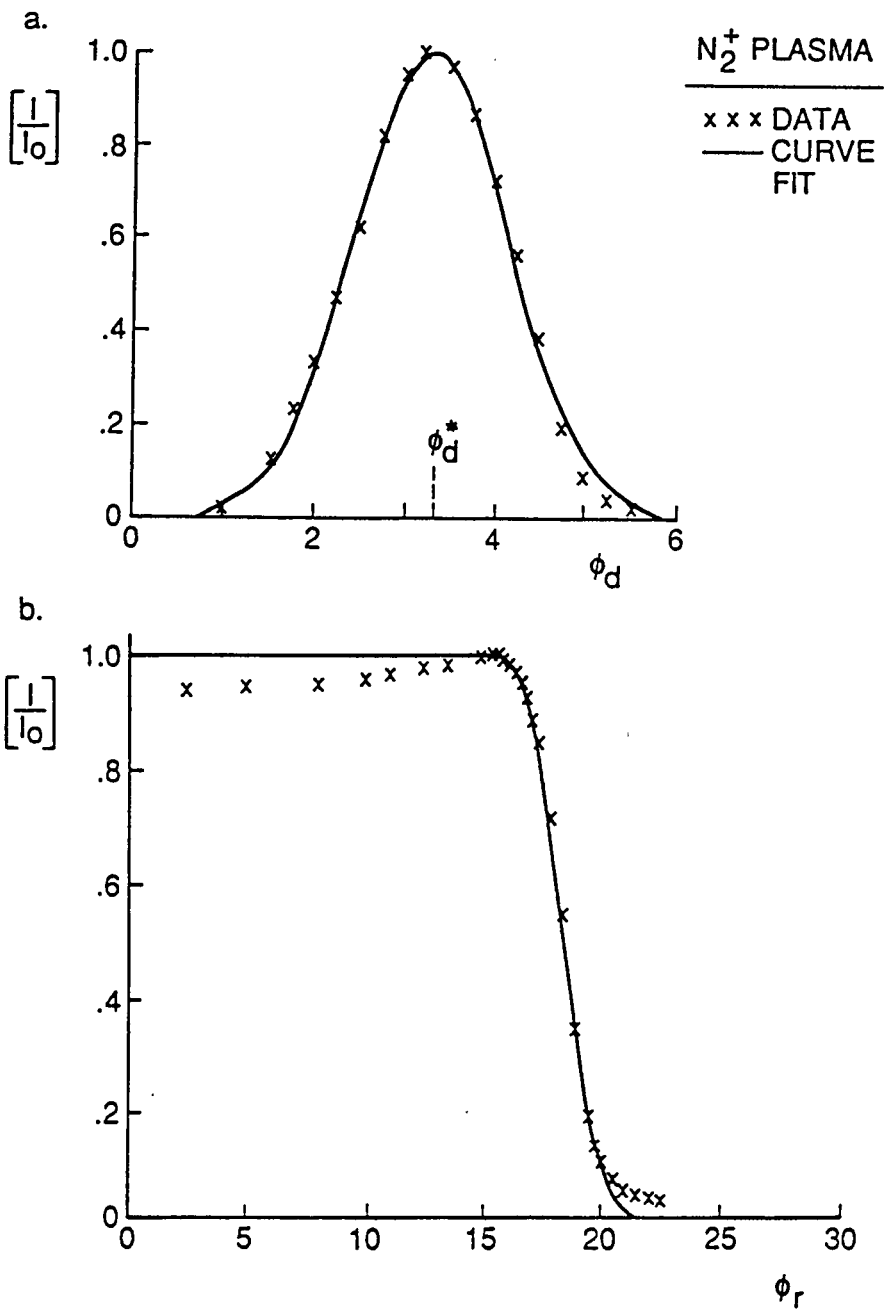

Figure 50. The variation of normalized current (I/I_0) with applied voltage for the two DIFP operational modes. The data are indicated by 'x' . (*a*) Deflection mode: ϕ_d swept, $\phi_r = 0$. ϕ_d^* = the voltage at the current maximum. Solid line is a curve fit to (C.6). (*b*) Retarding mode: ϕ_r swept, $\phi_d = \phi_d^*$. Solid line is a curve fit to (C.4). The ion energy (E_i) is approximately the ϕ_r value at $[I/I_0] = 0.5$. The incident angle, θ, is determined from (C.3) with the ϕ_d^* and E_i values.

experiment were $20\,\text{eV} < E_i(Ne^+) < 25\,\text{eV}$ and $85\,\text{eV} < E_i(Kr^+) < 95\,\text{eV}$.) This difference in drift energy between the two ion species and the vector measurement capability of the DIFP is exploited to determine the behavior of each ion species, independently, during the experiment.

Figure 51 shows the deflection mode response of the DIFP for the Ne^+, Kr^+ plasma. The current for the deflection sweep when $\phi_r = 0$ is shown in Figure 51*a* for the case when the flow is nearly parallel to the instrument normal. Both ion species reach the collector at this ϕ_r value. If the value of ϕ_r is increased to a value whereby all Ne^+ ions are prevented from reaching the collector, then the deflection sweep produces the signature for Kr^+ only. This is indicated by the dashed line in Figure 51*a*, acquired for $\phi_r = 35\,\text{volts}$. The difference between the solid and dashed curves yields the deflection mode signature for Ne^+ only. The deflection curve for each ion can then be analyzed as in the previous section. Data acquisition and storage for all operations of the DIFP in the binary ion plasma experiment was accomplished by a MASSCOMP 560 computer. Real time analysis was not performed; however, graphic display of data on the terminal screen was utilized to aid in instrument operation.

If the incident plasma stream is along the instrument normal, or very close to it, the deflection mode response at $\phi_r = 0$ is like the solid curve in Figure 51*a*. If the ion stream arrives at some angle away from the normal then, since the ions possess different drift energies, the deflection mode peaks due to each ion will separate along the ϕ_d axis according to (C.3). This peak separation is illustrated in Figure 51*b*. An independent energy analysis of each stream can be obtained by sweeping ϕ_r at each of the deflection voltages corresponding to the two peaks. Separating the peaks, therefore, aids in determining the properties of the two constituents. To help accomplish this, the DIFP was rotated 5° about the entrance aperature slit in the measurement plane.

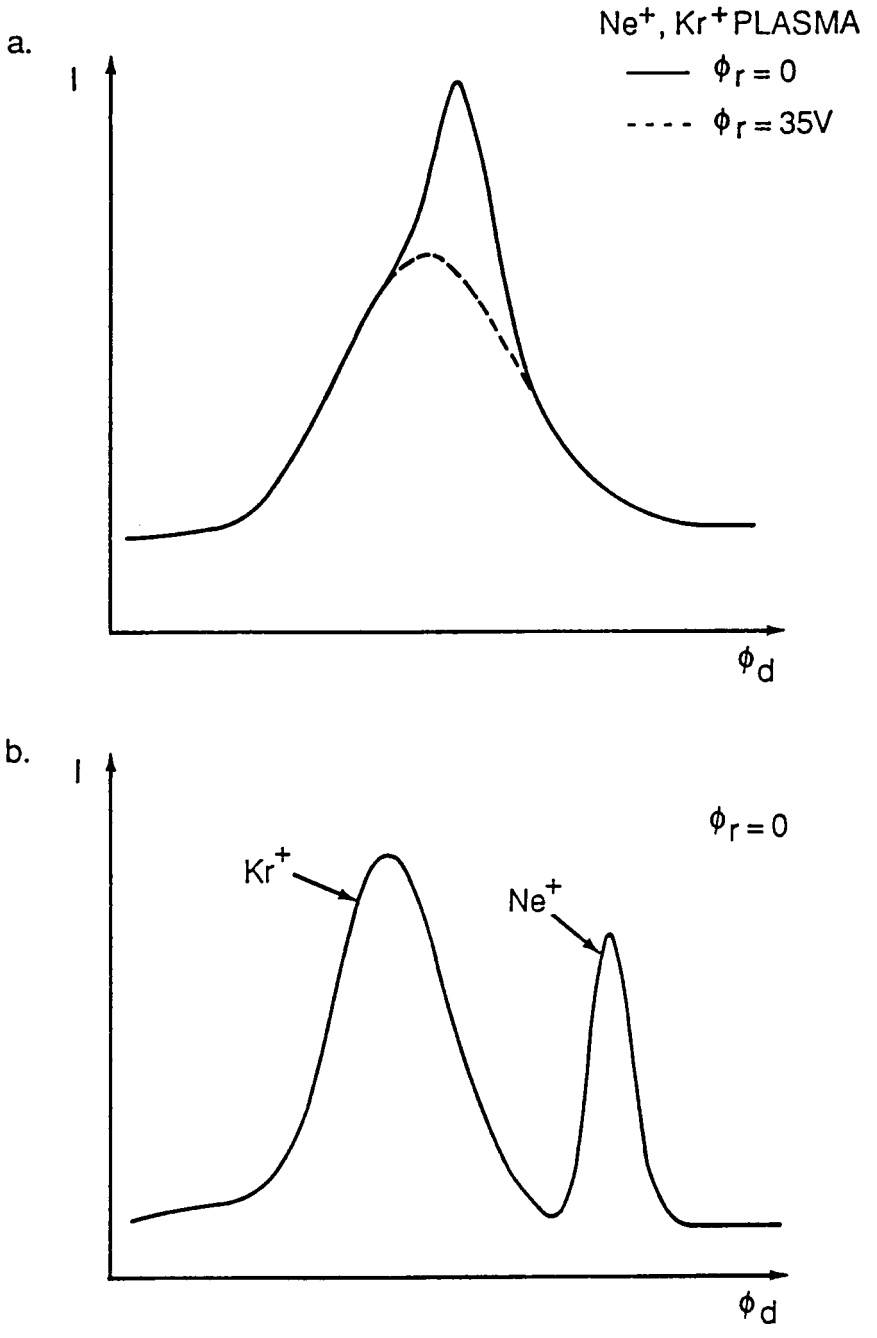

Figure 51. DIFP deflection mode response in a Ne^+, Kr^+ plasma. (a) Ion flow is nearly along the instrument normal. Both ion species contribute to the collected current at $\phi_r = 0$, indicated by the solid line. The dashed line indicates $I(Kr^+)$ only, acquired for $\phi_r = 35$ volts. The difference between the solid and dashed lines will give the $I(Ne^+)$ only response. (b) Ion flow at some non-zero incident angle. The two ion species form two distinct peaks as indicated.

Figure 52 presents an example DIFP measurment in the deflection and retarding mode for each ion species. The separation of the ion deflection mode signatures was performed as described above. Note that the normalized currents are plotted and that the scales for each x-axis are different. The curve fits were performed as discussed above in the single ion plasma case. The curve fit parameters for Ne^+ are $\phi_d^* = 2.6\,\text{v.}$, $\delta = 2.6\,\text{v.}$, $E_i = 24\,\text{eV}$, $T_{i_\parallel} = 0.27\,\text{eV}$; and for Kr^+, $\phi_d^* = 5.2\,\text{v.}$, $\delta = 7.4\,\text{v.}$, $E_i = 89.5\,\text{eV}$, $T_{i_\parallel} = 0.10\,\text{eV}$. The flow angles relative to the chamber axis, accounting for the 5° probe rotation, are then $\theta(Ne^+) = -2.8°$ and $\theta(Kr^+) = -3.8°$. Negative angles are defined as flow moving to the left looking downstream from the plasma source. The non-parallel flow for the Ne^+ and Kr^+ ions is discussed in Chapter IV. To calculate the ratio of the two ion currents at the measurement location, a correction for angular sensitivity must first be made. Equation (C.5) is used with the unnormalized data to determine the eqivalent $I(\theta = 0)$ value for each ion. The ratio $I_{Ne^+}(\theta = 0)/I_{Kr^+}(\theta = 0)$ then provides the proper experimental parameter.

The deflection curve half-width for Kr^+ is much wider than for Ne^+; i.e., $\delta(Kr^+) > \delta(Ne^+)$. This is due to Kr^+ having a much larger drift energy as compared with Ne^+. Similarly, the curve half-width $\delta(Ne^+)$ is greater than $\delta(N_2^+)$ for the single ion plasma case. Differences in E_i, $T_{i_\parallel}$, and possibly $T_{i_\perp}$ can contribute to this effect. When the Ne^+ data was compared with DIFP calibration data for approximately the same θ, E_i, and $T_{i_\parallel}$ values, $\delta(Ne^+)$ was still found to be larger. Attempts to translate this difference into an estimate for a $[T_{i_\perp}]_{eff}$ value were inconclusive. However, a qualitative statement can be made that $[T_{i_\perp}(Ne^+)]_{eff}$ was larger than $[T_{i_\perp}(N_2^+)]_{eff}$ in the single ion plasma experiment. Extrapolating to a qualitative estimate for Kr^+ yields $[T_{i_\perp}(Kr^+)]_{eff} \leq [T_{i_\perp}(Ne^+)]_{eff}$. The $T_{i_\parallel}$ for both Ne^+ and Kr^+ was much larger than the $T_{i_\parallel}$ in the single ion experiment.

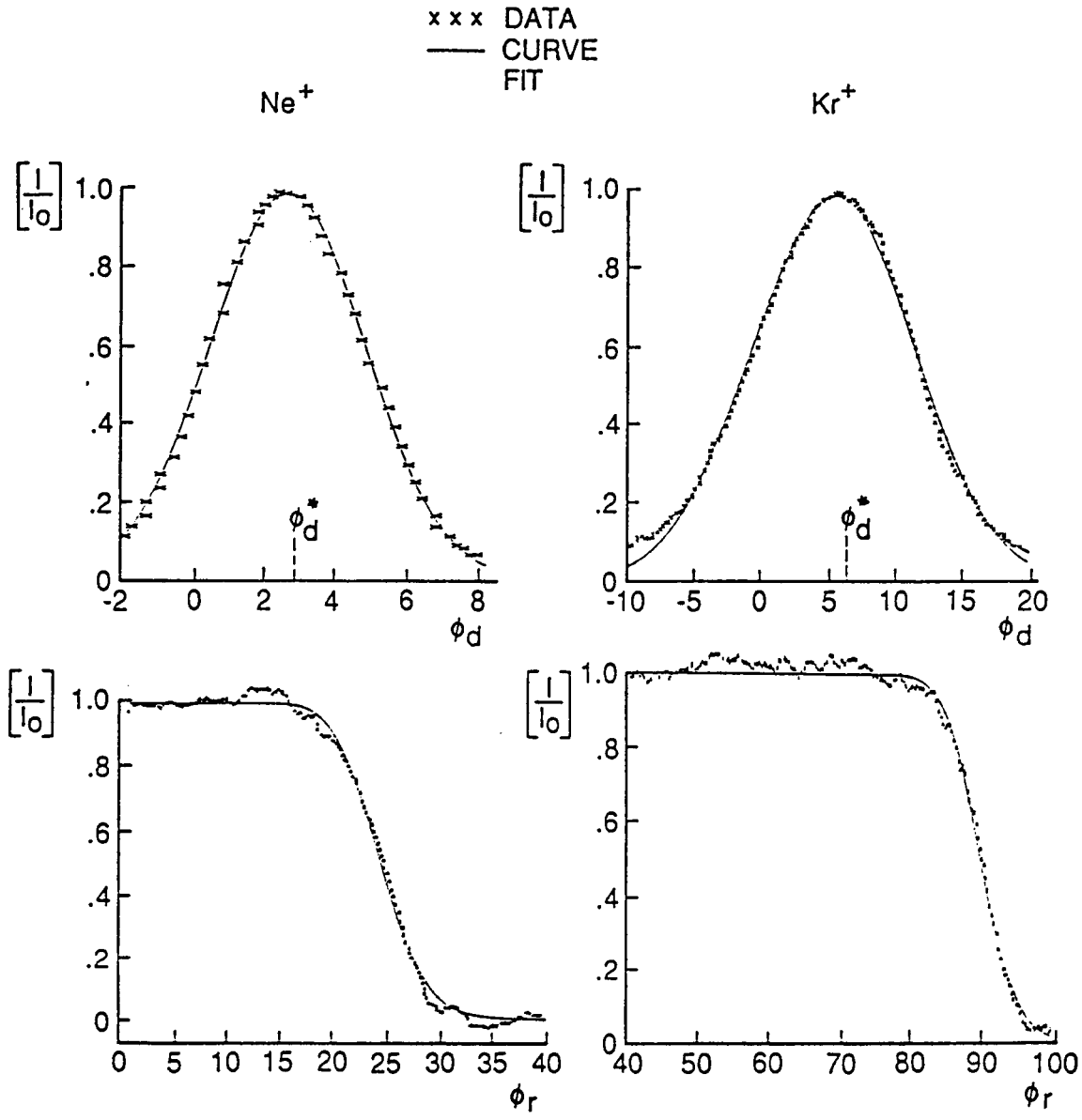

Figure 52. Analysis of the DIFP response for both Ne^+ and Kr^+ ions. The deflection signature for each ion species is separated in the manner described in Figure 51*a*. The retarding mode curves were obtained at the respective ϕ_d^* values. The data are indicated by 'x' . The solid lines are curve fits: (C.6) for the deflection mode; (C.4) for the retarding mode.

APPENDIX D. CONNECTION OF THE PLASMA FLOW-BODY INTERACTION WITH THE PLASMA EXPANSION PROBLEM

The development of the plasma expansion analogy as applied to the near wakes of bodies in flowing plasmas is given. First, an outline of the *Gurevich et al.* [1969] kinetic formulation is presented. Then, a brief description of the *Diebold* [1987] and *Diebold et al.* [1987*a*] fluid treatment is discussed. In both cases, limitations of the plasma expansion analogy are noted. The equations are written in Gaussian units.

1. *Gurevich et al.* [1969] kinetic approach

Consider a body moving supersonically through a collisionless, single ion plasma where the flow velocity is much greater than the ion thermal speed and much less than the electron thermal speed, i.e. the mesosonic flow regime. In a coordinate system moving with the body, the problem is considered to be time stationary. The Vlasov - Poisson equation system for the ion distribution function f is

$$\mathbf{v} \cdot \frac{\partial f}{\partial \mathbf{r}} - \frac{e}{M_i} \frac{\partial \phi}{\partial \mathbf{r}} \cdot \frac{\partial f}{\partial \mathbf{v}} = 0 \qquad (D.1)$$

and

$$\nabla^2 \phi = -4\pi e(n_i - n_e). \qquad (D.2)$$

The ion density is then given by

$$n_i = \int_{-\infty}^{\infty} f \, d\mathbf{v}. \qquad (D.3)$$

The electron gas is assumed to be isothermal and obey the Boltzmann relation given by

$$n_e = n_0 \exp(e\phi/kT_e). \qquad (D.4)$$

For bodies moving in planetary ionospheres, the body size is much larger than the Debye length; i.e.,

$$R_0 \gg \lambda_D. \tag{D.5}$$

The characteristic dimension of the disturbance caused by the moving body is R_0 and characteristic potentials are of the order kT_e/e. Equation (D.2) can be rewritten as

$$\left(\frac{\lambda_D}{R_0}\right)^2 = \left(\frac{n_e}{n_0} - \frac{n_i}{n_0}\right). \tag{D.6}$$

Using (D.5), the condition of quasi-neutrality results:

$$n_e = n_i. \tag{D.7}$$

The condition of quasi-neutrality is violated in the near vicinity of the body, but *Gurevich et al.* [1969] estimates that the region where large deviations from quasi-neutrality occur is small compared to the overall wake disturbance. General characteristics of the wake can then be determined under this assumption. However, the assumption is not necessary for achieving connection with plasma expansion. Therefore, combining (D.7) and (D.4) yields

$$e\phi = kT_e \ln(n_i/n_0). \tag{D.8}$$

Let the z-axis be oriented along the direction of motion, then (D.1) can be written as

$$v_z \frac{\partial f}{\partial z} + \mathbf{v}_1 \cdot \frac{\partial f}{\partial \mathbf{r}_1} - \frac{e}{M_i}\frac{\partial \phi}{\partial z}\frac{\partial f}{\partial v_z} - \frac{e}{M_i}\frac{\partial \phi}{\partial \mathbf{r}_1} \cdot \frac{\partial f}{\partial \mathbf{v}_1} = 0, \tag{D.9}$$

where $\mathbf{r}_1$, $\mathbf{v}_1$ are the projections of vectors $\mathbf{r}$, $\mathbf{v}$ on to plane orthogonal to the z-axis. For supersonic motion under condition (D.5), the disturbed region is elongated along the z-axis, i.e. a length of the order SR_0, where $S \equiv (M_i V_0^2/2kT_e)^{1/2}$. Thus, $|\partial\phi/\partial\mathbf{r}_1| \gg |\partial\phi/\partial z|$. In addition, in mesosonic flow, the thermal dispersion of

particles along z can be neglected such that $v_z \approx V_0$. With these two assumptions the third term in (D.9) may be neglected. The result is

$$V_0 \frac{\partial f}{\partial z} + \mathbf{v}_1 \cdot \frac{\partial f}{\partial \mathbf{r}_1} - \frac{e}{M_i} \frac{\partial \phi}{\partial \mathbf{r}_1} \cdot \frac{\partial f}{\partial \mathbf{v}_1} = 0. \tag{D.10}$$

Introduce the following dimensionless variables

$$\mathbf{p} = \mathbf{r}_1/R_0 \qquad t = z/(SR_0) \qquad \mathbf{u} = \mathbf{v}_1 \left(\frac{M_i}{2kT_e} \right)^{1/2}$$

$$g(t, \mathbf{p}, \mathbf{u}) = \frac{2\pi k T_i}{M_i n_0} \int f \, dv_z \qquad \Phi_N = e\phi/kT_e \tag{D.11}$$

Substituting (D.11) into (D.10) and (D.8) yields

$$\frac{\partial g}{\partial t} + \mathbf{u} \cdot \frac{\partial g}{\partial \mathbf{p}} - \frac{1}{2} \frac{\partial \Phi_N}{\partial \mathbf{p}} \cdot \frac{\partial g}{\partial \mathbf{u}} = 0 \qquad \Phi_N = \ln \int_{-\infty}^{+\infty} g \frac{d^2\mathbf{u}}{(\pi/T)}, \tag{D.12}$$

where $T = T_e/T_i$.

The boundary conditions will now be discussed. If the body is not too elongated in the z direction, and since the flow is supersonic ($S \gg 1$), the body can be replaced by a thin plate or disk with an area equal to the transverse area $\mathcal{A}_T$ at the maximum cross-section of the body. Let the ambient plasma be Maxwellian and consider that the ions are neutralized upon striking the body surface. Then the boundary conditions for the plasma at the body and at infinity are of the form

$$\begin{aligned} g &= 0 \qquad \text{for } R_0\mathbf{p} \text{ inside } \mathcal{A}_T; \\ g &= \exp(-T\mathbf{u}^2) \qquad \text{for} R_0\mathbf{p} \text{ outside } \mathcal{A}_T. \end{aligned} \tag{D.13}$$

This boundary condition leads to a singularity in the last term of the first equation (D.12). This can be eliminated by considering $\zeta \equiv \mathbf{n}_1 \cdot (\mathbf{p}_0 - \mathbf{p})$ (where $\mathbf{n}_1$ is the normal to the cross-section $\mathcal{A}_T$ at a point $\mathbf{p}_0$ of the contour) and small values for ζ and t, i.e. $|\zeta| \ll 1$ and $t \ll 1$. The curvature of the contour can now be neglected.

If the solution space is also confined to where particles from the opposite side of the body do not reach the point of observation, then no characteristic spatial dimension now exists in the problem. The solutions to (D.12) will now depend only on the ratio ζ/t, i.e. the problem is self-similar in ζ/t. Let

$$g_a(\tau, u_\zeta) = \frac{1}{\sqrt{\pi/T}} \int_{-\infty}^{+\infty} g(\tau, u_\zeta, u_\nu)\, du_\nu \quad \tau \equiv \zeta/t \quad u_\zeta = \mathbf{u} \cdot \mathbf{n}_1. \tag{D.14}$$

Substituting (D.14) into (D.12) the following equation for g_a is obtained

$$(u_\zeta - \tau)\frac{\partial g_a}{\partial \tau} - \frac{1}{2}\frac{\partial g_a}{\partial u_\zeta}\frac{d}{d\tau}\left(\ln \int_{-\infty}^{\infty} g_a \frac{du_\zeta}{\sqrt{\pi/T}}\right) = 0 \tag{D.15}$$

The boudary conditions for g_a can be rewritten in the form: $\tau \to -\infty$, $g_a \to \exp(-Tu^2)$ and $\tau \to +\infty$, $g_a \to 0$. The solution of (D.15) with the boundary conditions then describes the ion behavior near the edge of the body. Equation (D.15) is formally identical to (A.10), which was derived in the plasma expansion context.

In applying these equations to the near wake of a large flat plate, *Gurevich et al.* [1969] note a limit of the validity of the above model. In this case, the transverse dimension is x, i.e. $\zeta \to x$, and the quantities are independent of y. The approximation of $\partial/\partial z \simeq 0$ will not hold for $x \simeq z$. In dimensionless variables, this is

$$\tau \simeq S \tag{D.16}$$

(or $\xi \simeq \mathcal{M}$ in the notation of Chapters II and III). At this point the potential energy of the ions is of the order $M_i V_0^2/2$, so that v_z has been influenced by the electric field. The condition implied then is that for $M_i V_0^2/2 > e\phi$ or

$$S^2 (\text{or } \mathcal{M}^2) > \Phi_N, \tag{D.17}$$

the identity with plasma expansion holds. *Alikhanov et al.* [1971] investigated flow about a conducting plate both numerically and experimentally. The computer simulation solved essentially (D.15) with Poisson's equation (D.2). Good quantitative

agreement was found between the experiment and the simulation as long as relation (D.17) held.

2. *Diebold* [1987] and *Diebold et al.* [1987*a*] fluid approach

In these studies, the time independent, two dimensional fluid equations

$$\nabla \cdot (n\mathbf{v}) = 0 \qquad (D.18)$$

$$(\mathbf{v} \cdot \nabla)\mathbf{v} = -qn\nabla\phi - T\nabla n\,, \qquad (D.19)$$

where n, $\mathbf{v}$, q, and T refer either to the ion or electron density, velocity, charge, and temperature, respectively, together with Poisson's equation (D.2) were investigated for self-similar behavior for application to the near wake. Only the self-similar form of the equations was sought, which can provide insight into the wake structure without finding specific solutions. The plasma flow was considered aligned with the z axis. The x axis was transverse to the flow axis and the dependent variables were considered independent of y. The following variable definitions were used:

$$\hat{\xi} \equiv v_z^{\alpha}\left(\frac{x - x_0}{z - z_0}\right) \qquad \text{and} \qquad N \equiv \frac{n(z - z_0)^{\beta}}{v_z^{\alpha\beta}}. \qquad (D.20)$$

Note that for $\alpha = 1$, $\hat{\xi} \rightarrow \xi$, where $\xi \simeq x/t$, the self-similar variable in the plasma expansion theory and the *Gurevich et al.* [1969] wake theory from the preceeding section with $t = z/v_z$. Also, with $\beta = 2$, $N = nt^2$. This quantity, N, was found to be self-similar in the plasma expansion theory of *Lonngren and Hershkowitz* [1979], where the time dependent, one dimensional ion fluid equations were solved with Poisson's equation [see (A.11), (A.12), (A.2), (A.5)]. When the relations in (D.20) are used in (D.18) and (D.19), the resulting equations do not depend only on ξ. Further restrictions must be applied; namely, the velocity v_z is independent of x and z (v_z constant), $(x - x_0)^2/(z - z_0)^2 \ll 1$, and $\partial\phi/\partial z = \partial n/\partial z = 0$. With these

limitations, the equations are now identical to the self-similar plasma expansion equations of *Lonngren and Hershkowitz* [1979]. These limitations are essentially the same ones used by *Gurevich et al.* [1969] and noted above.

If $\alpha = 0$ and $\beta = 2$ in the relations of (D.20), the equations derived from (D.18) and (D.19) will result in only a $\hat{\xi}$ dependence. This implies that the potential, velocity, and N are self-similar in $\hat{\xi} = (x - x_0)/(z - z_0)$. Thus, the equi-contours of potential, velocity, and N will be straight lines in the x, z plane. Potential measurements were performed in the wake of a half-plane, at floating potential, immersed in supersonic flow and were found to obey the x/z similarity. The contours mapped to a point (x_0, z_0) in the sheath at the plate edge, actually to a line along the plate edge, since y independence is assumed. When the Mach number was increased by factors of 1.4 and 1.7, and the other experimental properties held approximately constant, the potential for a particular contour value was still found to be self-similar in x/z and not self-similar in $V_0 x/z$. That is to say, the particular contour measured for the Mach number variation did not map to a single straight line in the $x, z/V_0$ plane. The scaling of the wake region for z/V_0 (or $z/\mathcal{M}$), if the other parameters remain approximately constant, is known experimentally [e.g., *Samir et al.*, 1974; *Stone et al.*, 1974; *Fournier and Pigache*, 1975; *Stone*, 1981*c*]. That the near wake does not follow $z/\mathcal{M}$ scaling will need further investigation over a large range of Mach number. The single ion plasma experiment discussed in Chapter III is for only one Mach number and cannot address this point. However, the use of the variable $\omega_{pi}t$ in Chapter III (and also Chapter IV) does assume the $z/\mathcal{M}$ wake scaling.

REFERENCES

Alikhanov, S. G., V. G. Belan, G. N. Kichigin, and P. Z. Chebotaev, Expansion of a plasma in vacuum and flow of collisionless plasma around a plate, *Sov. Phys. JETP*, Engl. Transl., *32*, 1061, 1971.

Allen, J. E., and J. G. Andrews, A note on ion rarefaction waves, *J. Plasma Physics*, *4*, 187, 1970.

Anderson, D., J. Faulkner, H. Wilhelmsson, K. Nishikawa, and T. Tange, Study of similarity flows of two component laser produced plasmas, *Phys. Scripta*, *18*, 141, 1978.

Anderson, D., M. Bonnedal, and M. Lisak, Effects of magnetic field of self-similar plasma expansion into vacuum, *Phys. Scripta*, *22*, 507, 1980.

Barakat, A. R., and R. W. Schunk, Effects of hot electrons on the polar wind, *J. Geophys. Res.*, *89*, 9771, 1984.

Begay, F., and D. W. Forslund, Acceleration of multi-species ions in CO_2 laser-produced plasmas: experiments and theory, *Phys. Fluids*, *25*, 1675, 1982.

Bezzerides, B., D. W. Forslund, and E. L. Lindman, Existence of rarefaction shocks in a laser-plasma corona, *Phys. Fluids*, *21*, 2179, 1978.

Block, L. P., Interpretation of laboratory experiments of interest to space physics, in *Physics of Planetary Environments*, ed. D. J. Williams, *vol. I*, 255, 1976.

Borovsky, J. E., M. B. Pongratz, R. A. Roussel-Dupre, and T.-H. Tan, The laboratory simulation of unmagnetized supernova remnants: Absence of a blast wave, *Astrophys. J.*, *280*, 802, 1984.

Chan, C., Laboratory experiments on plasma expansion, in *Ion Acceleration in the Magnetosphere and Ionosphere*, *Geophys. Mono. 38*, 249, 1986.

Chan, C., N. Hershkowitz, A. Ferreira, T. Intrator, B. Nelson, and K. Lonngren, Experimental observations of self-similar plasma expansion, *Phys. Fluids*, *27*, 266, 1984.

Chang, C. T., and M. Hashmi, Oscillations modes of a laser-produced plasma expanding into a uniform magnetic field, *Phys. Fluids*,*20*, 533, 1977.

Chutov, Yu. I., and A. Yu. Kravchenko, Plasma expansion into vacuum, *Sov. J. Plasma Phys.*, Engl. Transl., *6*, 151, 1980.

Crow, J. E., P. L. Auer, and J. E. Allen, The expansion of a plasma into a vacuum, *J. Plasma Phys.*, *14*, 65, 1975.

Decoste, R., and B. H. Ripin, High energy ions from a Nd-laser produced plasma, *Appl. Phys. Lett.*, *31*, 68, 1977.

Decoste, R., and B. H. Ripin, High energy ion expansion in laser-plasma interactions, *Phys. Rev. Lett.*, *40*, 34, 1978.

Denavit, J., Collisionless plasma expansion into a vacuum, *Phys. Fluids*, *22*, 1384, 1979.

Diebold, D. A., Near wake self-similar phenomena, *Ph.D. thesis*, University of Wisconsin-Madison, 1987.

Diebold, D., N. Hershkowitz, T. Intrator, and A. Bailey, Self-similar potential in the near wake, *Phys. Fluids*, *30*, 579, 1987*a*.

Diebold, D., N. Hershkowitz, and S. Eliezer, Rarefaction shock in the near wake, *Phys. Fluids*, *30*, 3308, 1987*b*.

Eselevich, V. G., and V. G. Fainshtein, Expansion of a collisionless plasma into a vacuum, *Sov. Phys. Dokl.*, Engl. Transl., *24*, 114, 1979.

Eselevich, V. G., and V. G. Fainshtein, Expansion of collisionless plasma in a vacuum, *Sov. Phys. JETP*, Engl. Transl., *52*, 441, 1980.

Eselevich, V. G., and V. G. Fainshtein, Expansion of a collisionless plasma into vacuum, *Sov. J. Plasma Phys.*, Engl. Transl., *7*, 271, 1981.

Eselevich, V. G., and M. A. Filippov, Study of the mechanism for solar wind formation, *Planet. Space Sci.*, *34*, 1119, 1986.

Falthammar, C. G., Laboratory experiments of magnetosphere interest, *Space Sci. Rev.*, *15*, 803, 1974.

Felber, F. S., and R. Decoste, Fast expansions of laser-heated plasmas, *Phys. Fluids*, *21*, 520, 1978.

Feldman, W. C., J. R. Asbridge, S. J. Bame, J. T. Gosling, and D. S. Lemons, Characteristic electron variations across simple high speed solar wind streams, *J. Geophys. Res.*, *83*, 5285, 1978.

Fournier, G., and D. Pigache, Wakes in collisionless plasma, *Phys. Fluids*, *18*, 1443, 1975.

Goldenbaum, G. C., and K. A. Gerber, Experimental observations of the thermal expansion of a plasma, *Phys. Fluids*, *16*, 1289, 1973.

Graur, A. D., J. W. L. Prak, and A. W. Jenkins, Jr., A cylindrical shell model of the NASA-MPE barium ion cloud experiment, *Planet. Space Sci.*, *21*, 643, 1973.

Grebowsky, J. M., H. A. Taylor, Jr., M. W. Pharo, III, and N. Reese, Thermal ion perturbations observed in the vicinity of the space shuttle, *Planet. Space Sci.*, *35*, 501, 1987.

Gurevich, A. V., and L. P. Pitaevsky, Non-linear dynamics of a rarefied ionized gas, *Prog. Aerospace Sci.*, *16*, 227, 1975.

Gurevich, A. V., and A. P. Meshcherkin, Ion acceleration in an expanding plasma, *Sov. Phys. JETP*, Engl. Trans., *53*, 937, 1981*a*.

Gurevich, A. V., and A. P. Meshcherkin, Jump discontinuity on the front of a rarefaction wave front in a plasma, *Sov. Phys. JETP*, Engl. Transl., *54*, 688, 1981*b*.

Gurevich, A. V., L. V. Paryiskaya, and L. P. Pitaevsky, Self-similar motion of rarefied plasma, *Sov. Phys. JETP*, Engl. Transl., *22*, 449, 1966.

Gurevich, A. V., L. V. Paryiskaya, and L. P. Pitaevsky, Self-similar motion of a low density plasma II, *Sov. Phys. JETP*, Engl. Transl., *27*, 476, 1968.

Gurevich, A. V., L. P. Pitaevsky, and V. V. Smirnova, Ionospheric aerodynamics, *Space Sci. Rev.*, *9*, 805, 1969.

Gurevich, A. V., L. V. Paryiskaya, and L. P. Pitaevsky, Ion acceleration upon expansion of a rarefied plasma, *Sov. Phys. JETP*, Engl. Transl., *36*, 274, 1973*a*.

Gurevich, A. V., L. V. Paryiskaya, and L. P. Pitaevsky, One dimensional motion of a low density plasma in a magnetic field, *Sov. Phys. JETP*, Engl. Transl., *37*, 1071, 1973*b*.

Gurevich, A. V., D. Anderson, and H. Wilhelmsson, Ion acceleration in an expanding rarefied plasma With non-Maxwellian electrons, *Phys. Rev. Lett.*, *42*, 769, 1979.

Hairapetian, G., and R. L. Stenzel, Expansion of a non-Maxwellian, magnetized plasma into vacuum, *Phys. Rev. Lett.*, in press, 1987.

Hendel, H. W., and T. T. Reboul, Adiabatic acceleration of ions by electrons, *Phys. Fluids*, *5*, 360, 1962.

Hershkowitz, N., How Langmuir probes work, in *Plasma Diagnostics*, eds. O. Aucielello and D. Flam, Academic Press, New York, in press, 1987.

Hester, S. D., and A. A. Sonin, A laboratory study of the wakes of ionospheric satellites, *AIAA J.*, *8*, 1090, 1970.

Intriligator, D. S., and G. R. Steele, Observations of structuring in the downstream region of a large spherical model in a laboratory simulated solar wind plasma, *J. Geophys. Res.*, *87*, 6053, 1982.

Intriligator, D. S., and G. R. Steele, Analyses of experimental observations of electron temperatures in the near wake of a model in a laboratory simulated solar wind plasma, *J. Geophys. Res.*, *90*, 4027, 1985.

Johnson, S. F., and K. E. Lonngren, On the expansion of a magnetized plasma *Phys. Scripta*, *25*, 583, 1982.

Katz, I., D. E. Parks, and K. H. Wright, Jr., A model of the plasma wake generated by a large object, *IEEE Trans. Nucl. Sci.*, *NS-32*, 4092, 1985.

Kobel, E., Pressure and high velocity vapour jets at cathodes of a mercury vacuum arc, *Phys. Rev.*, *36*, 1636, 1930.

Korn, E., T. C. Marshall, and S. P. Schlesinger, Effects of plasma flow on electrostatic disturbances in a Q machine, *Phys. Fluids*, *13*, 517, 1970.

Kornowski, E. T., The region behind a body moving through a rarefied atmosphere, Proceedings of the Symposium on the Plasma Sheath, *Rep. AFCRC-TR-60-108(1)*, 1960.

Landau, L. D., and E. M. Lifshitz, *Fluid Mechanics*, Pergamon Press, Oxford, 1963.

Le Vaguerese, P., and D. Pigache, Etude d'une source d'ions de basse energie et a forte densite de courant, *Revue De Physique Applique*, *6*, 325, 1971.

Linlor, W. I., Ion energies produced by laser giant pulse, *Appl. Phys. Lett.*, *3*, 210, 1963.

Lonngren, K. E., Self-similar solution of plasma equations, *Proc. Indian Acad. Sci.*, *86 A*, 125, 1977.

Lonngren, K. E., and N. Hershkowitz, A note on plasma expansion into a vacuum, *IEEE Trans. Plasma Sci.*, *PS-7*, 107, 1979.

Martin, A. R., Numerical solutions to the problem of charged particle flow around an ionospheric spacecraft, *Planet. Space Sci.*, *22*, 121, 1974.

Mathews, W. G., The hydromagnetic free expansion of a relativistic gas, *Astrophys. J.*, *165*, 147, 1971.

Merlino, R. L., and N. D'Angelo, The interaction of a conducting object with a supersonic plasma flow: ion deflection near a negatively charged obstacle, *J. Plasma Phys.*, *37*, 185, 1987.

Mitrovich, D., Fast ion predictions from a simple hot-electron model, *Phys. Fluids*, *28*, 2591, 1985.

Mora, P., and R. Pellat, Self-similar expansion of a plasma into a vacuum, *Phys. Fluids*, *22*, 2300, 1979.

Morgan, M. A., C. Chan, and R. C. Allen, A laboratory study of the electron temperature in the near wake of a conducting body, *Geophys. Res. Lett.*, *14*, 1170, 1987.

Oran, W. A., U. Samir, N. H. Stone, and E. G. Fontheim, Laboratory observations of electron temperature in the wake of a sphere in a streaming plasma, *Planet. Space Sci., 23*, 1081, 1975.

Oran, W. A., U. Samir, and N. H. Stone, Slow ion in plasma wind tunnels, *AIAA J.*, *14*, 1141, 1976.

Parker, L. W., Computation of collisionless steady state plasma flow about a charged disk, *NASA Contract. Rep.,CR-144159*, 1976.

Parker, L. W., Calculation of sheath and wake structure about a pillbox-shaped spacecraft in a flowing plasma, Proceedings of the Spacecraft Charging Technology Conference, *Rep. AFGL-TR-77-0051/NASA TMX-73537*, 1977.

Pillip, W. G., H. Miggenrieder, M. D. Montgomery, K.-H. Mühlhäuser, H. Rosenbauer, and R. Schwenn, Characteristics of electron velocity distribution functions in the solar wind derived from the Helios plasma experiment, *J. Geophys. Res.*, *92*, 1075, 1987*a*.

Pillip, W. G., H. Miggenrieder, M. D. Montgomery, K.-H. Mühlhäuser, H. Rosenbauer, and R. Schwenn, Unusual electron distribution functions in the solar wind derived from the Helios plasma experiment: Double-strahl distributions and distributions with an extremely anisotropic core, *J. Geophys. Res.*, *92*, 1093, 1987*b*.

Pillip, W. G., H. Miggenrieder, K.-H. Mühlhäuser, H. Rosenbauer, R. Schwenn, and F. Neubauer, Variations of electron distribution functions in the solar wind, *J. Geophys. Res.*, *92*, 1103, 1987*c*.

Plyutto, A. A., Acceleration of positive ions in expansion of the plasma in a vacuum spark, *Sov. Phys. JETP*, Engl. Transl., *12*, 1106, 1961.

Podgorny, I. M., Simulation studies of space, *Fund. Cosmic Phys.*, *4*, 1, 1978.

Podgorny, I. M., E. M. Dubinin, and P. L. Israelevich, Laboratory simulation of the induced magnetospheres of comets and Venus, *Moon and Planets*, *23*, 323, 1980.

Raadu, M. A., Expansion of a plasma injected from an electrodeless gun along a magnetic field, *Plasma Phys. Contr. Nucl. Fus.*, *21*, 331, 1979.

Raychaudhuri, S., J. Hill, H. Y. Chang, E. K. Tsikis, and K. E. Lonngren, An experiment on the plasma expansion into a wake, *Phys. Fluids*, *29*, 289, 1986.

Reader, P. D., The operation of an electron-bombardment ion source with various gases, *NASA TMX-52006*, 1964.

Sack, Ch., and H. Schamel, Evolution of a plasma expanding into vacuum, *Plasma Phys. Contr. Fus.*, *27*, 717, 1985.

Sack, Ch., H. Schamel, and R. Schmalz, The asymptotic velocity of fast ions in expanding plasmas, *Phys. Fluids*, *29*, 1337, 1986.

Samir, U., Bodies In flowing plasmas: Spacecraft measurements, *Adv. Space Res.*, *1*, 373, 1981.

Samir, U., and Y. J. Kaufmann, An assessment of the relative importance of body and plasma properties in determining the ram ion current distribution in the wake of an ionospheric satellite, *J. Atmos. Terr. Phys.*, *42*, 533, 1980.

Samir, U., and E. G. Fontheim, Comparison of theory and in situ observations for electron and ion distributions in the near wake of the Explorer 31 and AE-C satellites, *Planet. Space Sci.*, *29*, 975, 1981.

Samir, U., N. H. Stone, and W. A. Oran, Does a 'two stream' flow model apply to wakes of large bodies in space?, *Astrophys. Space Sci.*, *31*, L1, 1974.

Samir, U., K. H. Wright, Jr., and N. H. Stone, The expansion of a plasma into a vacuum: Basic phenomena and processes and applications to space physics, *Rev. Geophys.*, *21*, 1631, 1983.

Samir, U., N. H. Stone, and K. H. Wright, Jr., On plasma disturbances caused by the motion of the space shuttle and small satellites: A comparison of in situ observations, *J. Geophys. Res.*, *91*, 277, 1986.

Sharma, S. R., S. Yashvir, and T. N. Bhatnagar, New analytical solution for an ion-acoustic soliton in a two-ion plasma, *Phys. Fluids*, *29*, 442, 1986.

Shuvalov, V. A., Structure of the near wake behind a sphere in the flow of a nonequilibrium rarefied plasma, *Geomagn. Aeron.*, Engl. Transl., *19*, 440, 1979*a*.

Shuvalov, V. A., Flow of a nonequilibrium rarefied plasma around a sphere, *Geomagn. Aeron.*, Engl. Transl., *19*, 670, 1979*b*.

Shuvalov, V. A., Structure of the near wake behind a cylinder in a nonequilibrium rarefied plasma flow, *Geomagn. Aeron.*, Engl. Transl., *20*, 293, 1980.

Singh, N., and R. W. Schunk, Numerical calculations relevant to the initial expansion of the polar wind, *J. Geophys. Res.*, *87*, 9154, 1982.

Singh, N., and R. W. Schunk, Expansion of a multi-ion plasma into a vacuum, *Phys. Fluids*, *26*, 1123, 1983*a*.

Singh, N., and R. W. Schunk, Numerical simulations of counterstreaming plasmas and their relevance to interhemispheric flows, *J. Geophys. Res.*, *88*, 7867, 1983*b*.

Singh, N., and R. W. Schunk, Temporal behavior of density perturbations in the polar wind, *J. Geophys. Res.*, *90*, 6487, 1985.

Singh, N., U. Samir, K. H. Wright, Jr., and N. H. Stone, A possible explanation of the electron temperature enhancement in the wake of a satellite, *J. Geophys. Res.*, *92*, 6100, 1987.

Siskind, D. E., W. J. Raitt, P. M. Banks, and P. R. Williamson, Interactions between the orbiting space shuttle and the ionosphere, *Planet. Space Sci.*, *32*, 881, 1984.

Stenzel, R. L., R. Williams, R. Agüero, K. Kitazaki, A. Ling, T. McDonald, and J. Spitzer, Novel directional ion energy analyzer, *Rev. Sci. Instrum.*, *53*, 1027, 1982.

Stone, N. H., Technique for measuring the differential ion flux vector, *Rev. Sci. Instrum.*, *48*, 1458, 1977.

Stone, N. H., The aerodynamics of bodies in a rarefied ionized gas with applications to spacecraft environmental dynamics, *NASA Technical Paper 1933*, November 1981*a*.

Stone, N. H., The plasma wake of mesosonic conducting bodies. Part 1. An experimental parametric study of ion focusing by the plasma sheath, *J. Plasma Phys.*, *25*, 351, 1981*b*.

Stone, N. H., The plasma wake of mesosonic conducting bodies. Part 2. An experimental parametric study of the mid-wake ion density peak, *J. Plasma Phys.*, *26*, 385, 1981*c*.

Stone, N. H., and W. K. Rehmann, The simulation of ionospheric conditions for space vehicles, *NASA TN D-5894*, 1970.

Stone, N. H., and K. H. Wright, Jr., Initial results from the differential ion flux probe, in *Spacelab 2: 90 Day Post-Mission Report*, ed. E. W. Urban, NASA Marshall Space Flight Center, November 14-15, 1985.

Stone, N. H., W. A. Oran, and U. Samir, Collisionless plasma flow over a conducting sphere, *Planet. Space Sci.*, *20*, 1787, 1972.

Stone, N. H., U. Samir, and W. A. Oran, Laboratory simulation of the structure of disturbed zones around bodies in space, *J. Atmos. Terr. Phys.*, *36*, 253, 1974.

Stone, N. H., U. Samir, and K. H. Wright, Jr., Plasma disturbances created by probes in the ionosphere and their potential impact on low-energy measurements

considered for spacelab, *J. Geophys. Res.*, *83*, 1668, 1978.

Stone, N. H., U. Samir, K. H. Wright, Jr., D. L. Reasoner, and S. D. Shawhan, Multiple ion streams in the near vicinity of the Space Shuttle, *Geophys. Res. Lett.*, *10*, 1215, 1983.

Stone, N. H., K. H. Wright, Jr., K. S. Hwang, U. Samir, G. B. Murphy, and S. D. Shawhan, Further observations of Space Shuttle plasma-electrodynamic effects from OSS-1/STS-3, *Geophys. Res. Lett.*, *13*, 217, 1986.

Tan, T.-H., and J. E. Borovsky, Spherically symmetric high velocity plasma expansions into background gases, *J. Plasma Phys.*, *35*, 239, 1986.

Tanberg, R., On the cathode of an arc drawn in vacuum, *Phys. Rev.*, *35*, 1080, 1930.

Tariq, G. F., T. P. Armstrong, and J. M. Lowery, Electrodynamic interaction of Ganymede with the Jovian magnetosphere and the radial spread of wake associated disturbances, *J. Geophys. Res.*, *90*, 3995, 1985.

Tonks, L., The rate of vaporization from an anchored cathode spot, *Phys. Rev.*, *54*, 634, 1938.

True, M. A., J. R. Albritton, and E. A. Williams, Fast ion production by suprathermal electrons in laser fusion plasmas, *Phys. Fluids*, *24*, 1885, 1981.

Whipple, E. C., Exploration of the upper atmossphere with the help of the third Soviet Sputnik (ion trap results), *Proc. IRE*, *47*, 2023, 1959.

Wickens, L. M., and J. E. Allen, Free expansion of a plasma with two electron temperatures, *J. Plasma Phys.*, *22*, 167, 1979.

Wickens, L. M., and J. E. Allen, Ion emission from laser-produced, multi-ion species, two electron temperature plasmas, *Phys. Fluids*, *24*, 1894, 1981.

Widner, M., I. Alexeff, and W. D. Jones, Plasma expansion into a vacuum, *Phys. Fluids*, *14*, 795, 1971.

Winningham, J. D., and W. J. Heikkila, Polar cap auroral electron fluxes observed with ISIS 1, *J. Geophys. Res.*, *79*, 949, 1974.

Wright, K. H., Jr., N. H. Stone, and U. Samir, A study of plasma expansion phenomena in laboratory generated plasma wakes: Preliminary results, *J. Plasma Phys.*, *33*, 71, 1985.

Wright, K. H., Jr., D. E. Parks, I. Katz, N. H. Stone, and U. Samir, More on the expansion of a collisionless plasma into the wake of a body, *J. Plasma Phys.*, *35*, 119, 1986.

1. REPORT NO.	2. GOVERNMENT ACCESSION NO.	3. RECIPIENT'S CATALOG NO.
NASA CR-4125		

4. TITLE AND SUBTITLE	5. REPORT DATE
A Study of Single and Binary Ion Plasma Expansion Into Laboratory-Generated Plasma Wakes	February 1988
	6. PERFORMING ORGANIZATION CODE
7. AUTHOR(S)	8. PERFORMING ORGANIZATION REPORT #
Kenneth Herbert Wright, Jr.	
9. PERFORMING ORGANIZATION NAME AND ADDRESS	10. WORK UNIT NO.
Department of Physics The University of Alabama in Huntsville Huntsville, AL 35899	M-582
	11. CONTRACT OR GRANT NO.
	NAG8-058 & NAS8-31088
12. SPONSORING AGENCY NAME AND ADDRESS	13. TYPE OF REPORT & PERIOD COVERED
National Aeronautics and Space Administration Washington, D.C. 20546	Contractor Report
	14. SPONSORING AGENCY CODE

15. SUPPLEMENTARY NOTES

Marshall Contracting Officer's Representative: Charles R. Chappell
Marshall Space Flight Center, Space Science Laboratory

16. ABSTRACT

Plasma expansion into the wake of a large rectangular plate immersed in a collisionless, supersonic plasma has been investigated in laboratory experiments. The experimental conditions address both single ion and binary ion plasma flows for the case of a body whose size is large in comparison with the Debye length and the potential difference between the body and the plasma is relatively small. A new plasma source has been developed to generate equi-velocity, binary ion plasma flows, which allows access to new dimensions in parameter space that have previously been unavailable for laboratory studies. Specifically, the new parameters are the ionic mass ratio and the ionic component density ratio. In a series of experiments, a krypton-neon plasma (mass ratio of 4.15) is employed where the ambient density ratio of neon to krypton is varied more than an order of magnitude. The expansion in both the single ion and binary ion plasma cases is limited to early times, i.e., a few ion plasma periods, by the combination of plasma density, plasma drift speed, and vacuum chamber size, which prevented detailed comparison with self-similar theory.

Several characteristics of the process involved in "plasma expansion into vacuum" that have been predicted theoretically are observed for the single and binary ion plasmas. For the single ion plasma case these include: (1) the propagation of a rarefaction wave into the ambient plasma, (2) the creation and motion of an expansion front, and (3) the acceleration of ions into the wake at speeds above the ion acoustic speed. These results for the single ion plasma case are in good agreement with numerical simulations and other laboratory experiments for the early time expansion.

For the binary ion plasma case, neither numerical simulations nor experimental results exist for comparison with the analogous early expansion times of this experiment. New experimental results include: (1) the propagation of a rarefaction wave for each ionic component into the ambient plasma, (2) the formation of a plateau-like region in the neon (the lighter mass) ion current density when the neon ions are the minor ionic species in the ambient plasma, and (3) the acceleration of both ionic species, with neon accelerating at a higher rate than krypton. Results of this study for the single ion and binary ion plasmas indicate that the plasma expansion process is the dominant filling mechanism of the near wake of a body under these experimental conditions.

17. KEY WORDS	18. DISTRIBUTION STATEMENT
Laboratory Plasma Wake, Plasma Expansion, Single and Binary Ion Plasma Flows	Unclassified—Unlimited Subject Category: 75

19. SECURITY CLASSIF. (of this report)	20. SECURITY CLASSIF. (of this page)	21. NO. OF PAGES	22. PRICE
Unclassified	Unclassified	186	A09

For sale by National Technical Information Service, Springfield, Virginia 22161

NASA-Langley, 1988